

UNIVERSITY OF READING  
DEPARTMENT OF MATHEMATICS AND  
STATISTICS

**Numerical Modelling of Glaciers:  
Moving Meshes and Data  
Assimilation**

Dale Partridge

Thesis submitted for the degree of  
Doctor of Philosophy  
June 2013

# Abstract

In this thesis we consider the solution to dynamical ice flow equations using a combination of a moving mesh method and data assimilation. We show that by moving the mesh the approximation to the ice thickness profile is improved, and the location of the domain boundary is significantly better estimated. The method used is derived by utilising a relative mass conservation principle to define a net deformation velocity comprising of the internal diffusion of ice and the effect of accumulation or ablation.

We use a finite difference numerical approximation in one-dimension and a finite element approximation in two-dimensions to demonstrate the ability of the methods to simulate different aspects of ice flow. In particular we focus on the accurate representation of the moving front of the glacier without the need for an interpolation procedure. Results are shown to compare favourably to exact, steady state solutions, while demonstrating improvements over traditional fixed grid methods.

The impact of the internal diffusion of the ice on the movement of the glacier front is analysed, and a condition on the local profile near the boundary is constructed to determine when the front is moving as a result of diffusion rather than the accumulation or ablation.

We utilise the technique of data assimilation to combine the moving mesh method with observational information to get a statistically best estimate of the ice thickness profile. In a moving mesh environment there are differences to the scheme that we detail, in both one and two dimensions.

We introduce an extension to our data assimilation scheme to directly include the numerical mesh within the update. This allows for the potential inclusion of observations of key features such as the location of the boundary. We demonstrate the improvement that this extension has on our prediction of the domain in one dimension and discuss the challenges encountered when applying this extension to two dimensions.

# Declaration

I confirm that this is my own work and the use of all material from other sources has been properly and fully acknowledged.

Dale Partridge

# Acknowledgements

Well, I got there...somehow! A lot of credit goes to my supervisors, Prof. Mike Baines and Prof. Nancy Nichols for dragging me through kicking and screaming when things weren't working and being a constant source of ideas. To have two walking encyclopedias of knowledge as supervisors has been fantastic! Additionally I would like to thank the lecturers at the University Centre in Svalbard (UNIS) for teaching me so much and giving me the opportunity to visit such an amazing place.

Special thanks goes to my better half, Sarah Williamson, who has kept me going and proof read the entire thesis for me to help avoid too many spelling mistakes.

A big shout out to my fellow PhD students who have kept me entertained over the years. Particular thanks to those I shared an office with, it is very sad that 'shared' is written in the past tense, I will miss seeing you guys on a regular basis. I would also like to ironically thank online flash games for single handedly attempting to destroy my focus during the entire project!

Finally I would like to thank the NERC National Centre for Earth Observation (NCEO) for the funding I received, without which I would not be writing this today.

# Contents

<b>Contents</b>	<b>iii</b>
<b>List of Figures</b>	<b>ix</b>
<b>List of Tables</b>	<b>xiv</b>
<b>List of Variables</b>	<b>xv</b>
<b>1 Introduction</b>	<b>1</b>
1.1 Aims . . . . .	4
1.2 Key Results Achieved . . . . .	5
1.3 Thesis Outline . . . . .	6
<b>2 Glaciology</b>	<b>9</b>
2.1 Introduction . . . . .	9
2.2 Ice Rheology . . . . .	10
2.3 Mass Continuity . . . . .	13
2.4 Models . . . . .	14
2.4.1 Full Stokes model . . . . .	15
2.4.2 Shallow Ice Approximation (SIA) . . . . .	15

2.4.3	Other Models . . . . .	17
2.5	Summary . . . . .	17
<b>3</b>	<b>Numerical Modelling</b>	<b>18</b>
3.1	Introduction . . . . .	18
3.2	Adaptive Meshes . . . . .	19
3.3	A Relative Mass Conservation Method . . . . .	22
3.4	Adaptive Ice Sheet Models . . . . .	26
3.5	Terminology . . . . .	29
3.6	Summary . . . . .	30
<b>4</b>	<b>Data Assimilation</b>	<b>31</b>
4.1	What is Data Assimilation? . . . . .	31
4.2	Data Assimilation Algorithms . . . . .	33
4.2.1	3D-VAR . . . . .	33
4.2.2	Kalman Filter . . . . .	37
4.2.3	4D-VAR . . . . .	38
4.3	Data Assimilation in Glaciology . . . . .	40
4.3.1	Available Observations . . . . .	40
4.4	Data Assimilation on Adaptive Meshes . . . . .	41
4.5	Summary . . . . .	41
<b>5</b>	<b>A 1D Moving Glacier Model</b>	<b>43</b>
5.1	The Shallow-Ice Glacier PDE . . . . .	43
5.2	Characteristics of the Shallow Ice PDE Model . . . . .	46
5.2.1	Diffusive Velocity at the Glacier Front . . . . .	46

5.2.2	Steady-state solution . . . . .	52
5.3	Glacier Movement . . . . .	54
5.3.1	Conserving Mass Fractions (CMF) . . . . .	54
5.3.2	Net Velocity at the Glacier Front . . . . .	55
5.3.3	Radial Adjustment . . . . .	56
5.4	Numerical Approximation . . . . .	57
5.4.1	A Finite Difference Scheme . . . . .	58
5.4.2	Numerical Diffusive Velocity at the Glacier Front . . . . .	59
5.4.3	Radial Adjustment - Numerics . . . . .	60
5.5	Experiments . . . . .	62
5.5.1	Testing the Model . . . . .	62
5.5.2	European Ice Sheet Modelling INiTiative . . . . .	67
5.6	Summary . . . . .	73
<b>6</b>	<b>Data Assimilation on Moving Meshes in 1D</b>	<b>74</b>
6.1	3D-VAR on a Moving Domain . . . . .	74
6.1.1	Observation Operator . . . . .	76
6.1.2	Observation Error Covariance Matrix . . . . .	76
6.1.3	Background Error Covariance Matrix . . . . .	77
6.1.4	Analysis Solution and Mass Conservation . . . . .	79
6.1.5	3D-Var Algorithm for CMF Moving Mesh . . . . .	80
6.2	A Test Experiment . . . . .	81
6.2.1	Initial Conditions . . . . .	81
6.2.2	Results . . . . .	82
6.3	An Extended Scheme: Assimilating the Mesh . . . . .	83

6.3.1	Observation Operator Extension . . . . .	85
6.3.2	Observation Error Covariance Matrix Extension . . . . .	86
6.3.3	Background Error Covariance Matrix Extension . . . . .	86
6.3.4	Extended 3D-Var Algorithm for CMF Moving Mesh . . . . .	88
6.4	Extended Scheme Experiments . . . . .	89
6.4.1	Observing the Boundary . . . . .	89
6.4.2	Including Cross-Covariances . . . . .	91
6.4.3	Discussion . . . . .	92
6.5	Summary . . . . .	95
<b>7</b>	<b>A 2D Moving Glacier Model</b>	<b>96</b>
7.1	The 2D Shallow Ice PDE . . . . .	96
7.1.1	Integral Property of Total Mass . . . . .	98
7.1.2	Non-Dimensionalisation of the Shallow Ice PDE . . . . .	99
7.2	Glacier Movement . . . . .	100
7.2.1	Conserving Mass Fractions (CMF) - Weak Formulation . . . . .	100
7.3	A Finite Element Scheme . . . . .	103
7.4	Experiments . . . . .	107
7.4.1	Testing the Model . . . . .	107
7.4.2	European Ice Sheet Modelling INiTiative . . . . .	113
7.5	Summary . . . . .	118
<b>8</b>	<b>Data Assimilation on Moving Meshes in 2D</b>	<b>119</b>
8.1	3D-VAR on a 2D Moving Domain . . . . .	119
8.1.1	Observation Operator . . . . .	120

8.1.2	Observation Error Covariance Matrix . . . . .	122
8.1.3	Background Error Covariance Matrix . . . . .	122
8.1.4	Analysis Solution and Mass Conservation . . . . .	123
8.1.5	3D-Var Algorithm for the CMF Moving Mesh Method . . . . .	124
8.2	A Test Experiment . . . . .	124
8.2.1	Initial Conditions . . . . .	125
8.2.2	Results . . . . .	125
8.3	2D Extended Scheme: Assimilating the Mesh - Theory . . . . .	129
8.3.1	Option 1: Conjoined Co-ordinates . . . . .	129
8.3.2	Option 2: Separate Co-ordinates . . . . .	130
8.3.3	Discussion . . . . .	132
8.4	Summary . . . . .	132
<b>9</b>	<b>Conclusions</b>	<b>133</b>
9.1	Summary . . . . .	133
9.2	Conclusions . . . . .	136
9.3	Future Work . . . . .	139
	<b>Appendices</b>	<b>142</b>
<b>A</b>	<b>Circular Mesh Generation</b>	<b>143</b>
A.1	Spoke . . . . .	143
A.2	Strang . . . . .	144
A.3	Hexagonal . . . . .	145
A.4	Automatic Generation . . . . .	146
<b>B</b>	<b>Useful Theorems</b>	<b>148</b>

*CONTENTS*

B.1 Leibniz's Integral Rule . . . . . 148

B.2 L'Hôpital's Rule . . . . . 148

B.3 Trapezium Rule . . . . . 149

B.4 Reynold's Transport Theorem . . . . . 149

B.5 Divergence Theorem . . . . . 149

**Bibliography** . . . . . **149**

# List of Figures

1.1	The Mer de Glace in the French Alps depicted as an ice dragon [13] . . .	2
2.1	The rate factor $A$ , determined by [27; 44]. The value of $A$ , and as a result the speed at which ice diffuses varies dramatically as the temperature of the ice changes. (Image from [102]) . . . . .	12
2.2	Mass changes in a column of ice (Modified from [10]) . . . . .	13
3.1	Example mesh mapping from a uniform computational domain (left) to an irregular physical domain (right). [17] . . . . .	21
3.2	Relative mass conservation concept for a velocity based moving mesh method. The mass of $\omega_1$ and $\omega_2$ as a fraction of the total mass $\Omega_1$ and $\Omega_2$ respectively are identical but the absolute mass is allowed to vary. . . . .	23
4.1	Concept cartoon of the optimal 3D-VAR data assimilation scheme, using each set of observations sequentially. . . . .	35
4.2	Concept cartoon of the Kalman Filter data assimilation scheme, a sequential scheme where the background error covariance matrix (dotted lines) is evolved through time in addition to the solution. . . . .	38
4.3	Concept cartoon of the 4D-VAR data assimilation scheme, which utilises all observations simultaneously to provide the best estimate of the system state. . . . .	39

5.1 Glacier domain along flowline from the fixed ice divide at  $x = 0$  to the moving front at  $x = b$  . . . . . 45

5.2 *Varying the parameter  $\alpha$  in Eq. (5.13) with  $g(x) = (1 + x)^\alpha$  leads to a critical value when considering the diffusive velocity at the glacier front. a) As  $\alpha \rightarrow 3/7$  from above the boundary diffusive velocity  $u_b$  jumps to a finite value. b) Velocity in the vicinity of the boundary for varying values of  $\alpha$ . As  $\alpha \rightarrow 3/7$  the velocity profile steepens, maintaining a zero velocity on the boundary until  $\alpha$  reaches  $3/7$ , at which point it jumps to a finite value . . . . . 49*

5.3 (a) Diffusive velocity. As  $\alpha \rightarrow 3/7$ , the peak velocity approaches the boundary, and when  $\alpha = 3/7$  (red line) the boundary velocity is finite whereas all other values have a zero boundary velocity. (b) Ice thickness profiles for  $\alpha = 1$  (solid) and  $\alpha = 3/7$  (dashed). Notice the infinite gradient at the boundary when  $\alpha = 3/7$  . . . . . 50

5.4 1D test equations: Ice thickness over the domain evolving from the initial profile (green) to a final steady state profile (blue). . . . . 64

5.5 Evolution of the mesh nodes over time, including the boundary point (red) representing the glacier front. . . . . 66

5.6 *Steady-state solutions to the EISMINT scenario: a) A 2D fixed grid method. b) 1D Moving mesh flowline radial model converted to 2D. c) Ice thickness profile along the flowline: exact (red), moving mesh (dash), fixed grid (solid). d) Diffusive velocity: moving mesh (dash), fixed grid (solid). . . . . 72*

6.1 A modified SOAR equation for rows of  $\mathbf{B}$  relating to different places in the domain. a) evenly spaced grid with even structure, b) unevenly spaced mesh after evolution. . . . . 78

6.2 Background error covariance matrix  $B$  using the Gaussian function Eq. (6.9);  
a) at the initial time when the mesh is evenly spaced, b) at  $t = 12000$   
when the mesh has moved. . . . . 79

6.3 1D moving mesh with data assimilation:- a-b) show the forecast, analysis  
and true ice thickness profile at  $t = 500$  and  $1500$  respectively, indicating  
the observations after noise is added. c) shows the time evolution of the  
boundary point  $x = b(t)$ . . . . . 84

6.4 Background error covariance matrix for the extended scheme; a) with-  
out cross covariance terms between the mesh and the ice thickness, b)  
with cross covariances between the boundary points and the ice thickness  
providing additional rows/columns. . . . . 88

6.5 1D moving mesh with data assimilation including observations of the  
boundary:- a-b) show the forecast, analysis and true ice thickness profile  
at  $t = 500$  and  $1500$  respectively, along with the observations after noise  
is added. c) shows the time evolution of the boundary point  $x = b(t)$ . . . 90

6.6 1D moving mesh with data assimilation:- evolution of mesh nodes through  
time. a) benchmark solution, b) including observations of the boundary. 91

6.7 1D moving mesh with data assimilation including cross-covariance terms  
in the extended background error covariance matrix,  $\mathbf{B}_e$ :- a-b) show the  
forecast, analysis and true ice thickness profile at  $t = 500$  and  $1500$   
respectively, along with the observations after noise is added. c) shows  
the time evolution of the boundary point  $x = b(t)$ . . . . . 92

6.8 1D moving mesh with data assimilation including cross-covariance terms  
in  $\mathbf{B}$  and boundary observations:- a-b) show the forecast, analysis and  
true ice thickness profile at  $t = 500$  and  $1500$  respectively, along with  
the observations after noise is added. c) shows the time evolution of the  
boundary point  $x = b(t)$ . . . . . 93

7.1	Arbitrary two-dimensional domain $\Omega(t)$ , with a moving boundary exhibiting a Dirichlet condition at the glacier front ( $\Gamma_D$ ) and Neumann boundary conditions ( $\Gamma_N$ ) along the rock walls . . . . .	97
7.2	Two-dimensional linear finite element ‘pyramid’ basis function [109] . .	104
7.3	Initial nodal location and mesh, using the Strang method (see Section A.2) for the two-dimensional test scenario . . . . .	109
7.4	Advancing Glacier: Ice Thickness Profile (left) and Net Velocity (right) at $t = 0, 2000, 15000, 30000$ (in descending order) with $\alpha = 3/7$ and $\beta = 0.72$ . . . . .	110
7.5	Retreating Glacier: Ice Thickness Profile (left) and Net Velocity (right) at $t = 0, 1000, 5000, 10000$ (in descending order) with $\alpha = 3/7$ and $\beta = 0.32$ . . . . .	111
7.6	Initially Stationary Glacier: Ice Thickness Profile (left) and Net Velocity (right) at $t = 0, 1000, 2000$ (in descending order) with $\alpha = 1$ and $\beta = 1$ . . . . .	112
7.7	Steady state solution to the EISMINT scenario: a) A 2D fixed grid method, b) 2D Moving mesh model. . . . .	115
7.8	Steady state ice thickness for the EISMINT problem using four different initial meshes. . . . .	116
7.9	Convergence analysis for varying mesh nodes using the spoked initial mesh: a) absolute error in the boundary position, b) computational time. . . . .	117
8.1	Point $P$ lying within triangle $ABC$ can be expressed in terms of its areal coordinates. . . . .	121
8.2	2D moving mesh with data assimilation at $t = 500$ :- a) Forecast before assimilation, b) Analysis solution, c) Reference solution and d) Difference between analysis and reference. . . . .	127
8.3	2D moving mesh with data assimilation at $t = 1500$ :- a) Forecast before assimilation, b) Analysis solution, c) Reference solution and d) Difference between analysis and reference. . . . .	128

8.4	2D moving mesh with data assimilation:- Evolution of a boundary point over time- Forecast (blue), Reference (Green), Analysis (Red). . . . .	128
A.1	An example of a mesh generated using spokes protruding from the centre, with 5 nodes per spoke and the angle between them $\pi/8$ . . . . .	144
A.2	A mesh generated using the Strang approach with 10 circles and 8 nodes per circle. At low resolution this mesh loses information close to the boundary and has a lot of long thin triangles which can cause numerical problems due to the shallow angle. . . . .	145
A.3	A hexagonal mesh with only 4 circles. Note that each interior node has 6 connections each and the regular hexagon in the centre. . . . .	146
A.4	Mesh generated using the software GMSH [37]. The software uses a refinement criteria that leaves the individual triangular elements approximately equilateral in shape. . . . .	147

# List of Tables

2.1	Table of typical values for Hookes modified Arrhenius equation. [13] . . .	12
5.1	Values of the physical parameters in the test model and the computational data used in the test equations. . . . .	63
5.2	Values of the physical parameters in the model and the computational data used in the EISMINT scenario. . . . .	68
5.3	Comparison between the average EISMINT experiment results, the moving mesh approach and the exact steady state solution. . . . .	70
5.4	Table of 1D values for boundary position and divide thickness with varying number of mesh nodes. . . . .	70
5.5	Error analysis for varying mesh nodes. . . . .	71
7.1	Values used within the test scenario including physical parameters of the PDE and the data used in the computational domain. . . . .	108
7.2	Two-dimensional EISMINT model parameters and functions. . . . .	114
7.3	Error comparison of steady state results from Fixed Grid and Moving Mesh solutions to the 2D EISMINT problem. . . . .	115
7.4	Table of steady state values for the boundary and divide thickness in the EISMINT problem under four different initial meshes. . . . .	117

# List of Symbols

## Glacier symbols

$\mathbf{x}$	Cartesian directional coordinates
$h(\mathbf{x}, t)$	Ice thickness
$m(\mathbf{x}, t)$	Ice equivalent accumulation rate
$\mathbf{u}(\mathbf{x}, t)$	Flow velocity (also called diffusive velocity)
$s$	Surface elevation
$\epsilon$	Strain rate
$\sigma'$	Deviatoric stress
$\epsilon_e$	Effective strain rate
$\sigma_e$	Effective stress
$A$	Rate factor
$n$	Flow law exponent
$T$	Temperature of the ice
$\rho$	Density of ice
$t$	Time
$p$	Pressure
$g$	Acceleration of gravity
$c$	Combination of constants in SIA

## Modelling symbols

$\Omega(t)$	Domain
$\omega(t)$	Sub-domain
$\Gamma(t)$	Domain boundary
$b(t)$	Glacial front in 1D
$\theta(t)$	Total mass
$\mu$	Relative mass constants
$\alpha$	Power of ice thickness profile factor
$\mathbf{v}$	Mesh velocity
$\psi$	Velocity potential
$k$	Time index
$i$	Spatial index
$\hat{x}$	Arbitrary interior point on the domain
$r$	Radial co-ordinate in 1D
$\mathbf{X}_i$	Numerical approximation to spatial co-ordinates $\mathbf{x}_i$
$H_i$	Numerical approximation to ice thickness at $\mathbf{x}_i$
$U_i$	Numerical approximation to diffusive velocity at $\mathbf{x}_i$
$\mu_i$	Numerical approximation to relative mass constants at $\mathbf{x}_i$
$\phi$	Total mass in radial co-ordinates
$\nu$	Relative mass constants in radial co-ordinates
$\mathbf{R}_i$	Numerical approximation to radial spatial co-ordinates $\mathbf{r}_i$
$\nu_i$	Numerical approximation to relative mass constants at $\mathbf{r}_i$
$\gamma$	Scale parameter in $m$
$\beta$	Equilibrium line
$b_{ss}$	Steady state boundary
$N$	Number of mesh nodes
$\mathcal{A}$	Area of finite element triangle

## Data Assimilation symbols

$\mathbf{z}$	State vector containing all model variables
$\mathcal{M}$	Model Operator
$\epsilon_m$	Error introduced by model operator
$\mathbf{y}^o$	Observation vector
$\mathcal{C}$	Observation operator mapping observations to model space
$\mathbf{C}$	Linearised observation operator
$\epsilon_o$	Error in observations
$q$	Size of state vector
$p$	Size of observation vector
$a$	Refers to 'analysis', or best guess solution
$f$	Prior solution, taken from the model
$J(\mathbf{z})$	Cost function
$\mathbf{B}_e$	Background error covariance matrix
$\mathbf{R}_e$	Observation error covariance matrix
$\mathbf{K}_e$	Correction, or Gain Matrix
$x^*$	Observation location
$\sigma_o$	Error variance for observations
$\sigma_b$	Error variance for state variables
$\mathbf{z}_e$	Extended state
$\mathbf{C}$	Extended linearised observation operator
$\mathbf{B}$	Extended background error covariance matrix
$\mathbf{R}$	Extended observation error covariance matrix
$\sigma_{ox}$	Error variance for observations of positional features
$\sigma_{bx}$	Error variance for mesh state variables
$\sigma_{bxh}$	Error variance for cross mesh-thickness variables

# Chapter 1

## Introduction

Advances in technology and the ability to reach the far ends of the Earth has allowed the study of the polar regions to accelerate in recent times. Within the polar regions, as well as alpine areas, there exist large bodies of ice that for the most part appear stationary. In fact the ice diffuses slowly under its own weight, and its movement impacts upon both the natural environment and human civilisation.

The state of ice on planet Earth has been the focus of much attention in recent times, particularly the rate at which the ice mass is decreasing. As with many natural features the impact of ice on the global climate is greater than in just the polar or alpine regions in which it exists. Ice stores around 80% of the fresh water found on the planet, which were it all to melt, would greatly impact the salinity of the ocean water as well as cause the much publicised sea level rise ( $\sim 65m$  if all ice melted). This would impact ocean circulations such as the Gulf stream which could ultimately bring long term changes to climate systems [75]. In addition the albedo of ice is high, between 0.5 and 0.9, which acts to reflect large amounts of incoming solar radiation [42]. On a more local scale a loss in ice mass can cause natural disasters such as floods and avalanches.

Moreover, during the various ice ages, glaciers and ice sheets expanded to claim large areas of the planet resulting in loss of life and, for some species, extinction. In the past the advance of ice has been likened to life threatening monsters such as the ice dragon drawn by HG Willinck (Figure 1.1). The glacier pictured (taken from [13]),

the Mer de Glace is no longer visible from the same location due to an extended period of retreat.



**Figure 1.1:** *The Mer de Glace in the French Alps depicted as an ice dragon [13]*

The recent news headlines claiming that all ice will melt within the next couple of generations are generally considered unlikely; however, the most recent assessment report of the IPCC (Intergovernmental Panel on Climate Change) in 2007 suggested that mathematical models are not yet sufficient to make credible predictions [96]. With this in mind much work has been devoted to increasing the accuracy of these mathematical models to reduce their uncertainty and provide better predictions for the future. These uncertainties in the models arise from two primary sources;

Firstly the dynamical response of ice to varying stress levels is extremely complex. While ice is generally considered to be viscous, it is highly non-linear, occasionally anisotropic and on some short time scales viscoelastic [51]. In addition there is the presence of debris, water and air mixed in between the ice.

Secondly the amount of data available is severely limited. Surface and satellite ob-

servations can give details about the upper layers of ice, but the state of deeper ice is harder to determine and is crucial to the flow of the entire body. For example the presence of meltwater near the base can cause basal sliding and thus speed up flow, which is currently an unresolved issue even if the location of any meltwater is known.

It is only recently that dynamical ice flow models have started to be included within global climate models. Part of the reason is the large uncertainties contained within the models, whilst also being computationally expensive, requiring a higher resolution than is present in current climate models. One potential solution is to use a simpler dynamical model which requires less computational time, though this invariably increases the uncertainty. Alternatively, ice sheet and climate models could be operated separately and coupled together. Generally this option would involve a coarse coupling, using ocean and atmospheric conditions from a climate model as forcing terms in the ice sheet model, and the ice cover extent and water outflow in the climate model [51]. Neither is a particularly elegant solution to an open problem.

An alternative to increasing the resolution is to consider adaptive mesh techniques, which allow better approximations to be made in the relevant areas. Several current methods utilise mesh refinement to increase the resolution in certain areas which work well provided the domain is reasonably well understood and the areas that require higher resolution are approximately known and unchanging. There are also a number of methods which move the computational mesh nodes to the required areas and have been shown to be more robust than non-adaptive methods [105]. Currently these move the nodes independently of time and are controlled by a monitor function which can be difficult to define [22]. In some other fields the movement of the mesh nodes is defined in terms of a time dependent velocity, which provides a clearer definition of the monitor function and allows the mesh to be influenced by its previous position(s). Currently this approach has not been applied to the dynamical ice flow equations.

The amount of information from satellites, aircraft and ground based measurements of ice sheets and glaciers is increasing. The glaciology community is beginning to make use of these observations in conjunction with numerical models using the techniques of data assimilation to produce the best possible representation. The atmospheric and

oceanic communities have been developing these techniques for many years, but the application to glaciology is in its infancy. In addition the application of data assimilation has largely been restricted to fixed grid methods, naturally since these are the most prominent methods used in operation. However it has been shown that adaptive methods are useful tools in the right situation [99], and at some point there will be a requirement to combine numerical adaptive methods with data assimilation.

Therefore there appears to be a gap in both the use of moving meshes and data assimilation applied to the field of glaciology. There also has been little development of data assimilation methods on moving meshes regardless of application. It is this gap that we seek to begin filling. We now lay out our aims for this thesis, followed by an overview of the key results and a detailed chapter-by-chapter plan.

## 1.1 Aims

In this thesis our main objectives are to:

- Develop a moving mesh method to equations governing dynamical ice flow.
- Use data assimilation to combine observations with a moving mesh model of dynamical ice flow.

In particular we aim:

1. To apply the conservation of mass fraction moving mesh method of Baines, Hubbard and Jimack [8], henceforth known as BHJ, to the one-dimensional shallow ice approximation equation used within glaciology.
2. To analyse the impact of internal glacier flow on the movement of the ice boundary.
3. To use a sequential 3D-Var data assimilation scheme in conjunction with the moving mesh to improve the predicted ice profile.

4. To build an extended scheme capable of including observations of positional features within the data assimilation method to improve the representation of the domain.
5. To extend the moving mesh method and the 3D-Var scheme to two horizontal dimensions and demonstrate the difficulties encountered when considering this more complex scenario.

## 1.2 Key Results Achieved

In this thesis we show that:

- Moving mesh methods are an effective tool to model the shallow ice equations quickly and accurately.
- Data assimilation can be performed on a moving mesh domain.
- Including the numerical mesh within the data assimilation scheme can improve the accuracy of the domain prediction in 1D.

Specifically we show that:

1. Using a moving mesh scheme based upon conserving fractional mass to simulate a 1D shallow ice flowline model can accurately simulate the key features of the ice sheet with minimal computational cost.
2. The impact of the flow velocity at the boundary is dependent on the local profile of the ice thickness, with an infinitely steep gradient required for the boundary to flow.
3. Results compare favourably to both the exact solution and fixed grid approximations to the European Ice Sheet Modelling INiTiative (EISMINT) experiment.
4. A sequential 3D-Var data assimilation scheme can incorporate observations into a moving mesh dynamical model.

5. With the chosen moving mesh method a recalculation of the total mass is required when assimilating to ensure mass conservation.
6. By extending the data assimilation scheme in 1D to include the numerical mesh we can find an improved solution of the mesh, enabling greater accuracy.
7. The moving mesh scheme readily extends to two horizontal dimensions.
8. The 3D-Var scheme can be applied to a 2D moving mesh to improve the numerical approximation.

### 1.3 Thesis Outline

In chapter 2 we begin by introducing the field of glaciology. We highlight the main driving forces behind the flow of ice and introduce the full Stokes model for simulating this flow. We then discuss how this is simplified to the shallow ice approximation model relevant to the work in this thesis.

We then give an introduction to adaptive mesh modelling in chapter 3, describing different ways a mesh may be adapted to improve the numerical approximation to the solution. In particular we focus on a moving mesh scheme, the relative mass conservation method of BHJ [8] that we will be applying to the shallow ice model in this thesis. We then discuss the current use of adaptive meshes within the field of glaciology.

Chapter 4 begins with a general introduction to data assimilation and some of the algorithms used operationally. We discuss the reasons for choosing the 3D-Var sequential method in this thesis over the other methods. We then look at the use of data assimilation within glaciology and the types of data that are available. Finally we discuss the attempts at using data assimilation on adaptive meshes.

In chapter 5 we analyse the behaviour of the internal flow velocity and its effect

on the boundary, providing conditions on the local glacier profile required to induce movement at the glacier front. We then apply the BHJ scheme to the shallow ice approximation. The scheme is discretised to form a numerical moving mesh method using finite differences as a means of approximation. We use a test scenario to illustrate the ability of the method to replicate aspects of glacier flow, before using the radially symmetric EISMINT problem to assess the benefits of the approach over existing methods.

We apply the 3D-Var data assimilation algorithm to the moving mesh method in chapter 6. We determine the required components of the algorithm and the modifications needed to apply it to a moving mesh model instead of a fixed grid. This is tested using a twin experiment applied to the test scenario introduced in the previous chapter. We propose an extension to the algorithm to include the numerical mesh within the data assimilation algorithm, allowing the mesh to be updated at the assimilation time and the potential to include observations of positional features. The changes required to the components of the algorithm are examined, before we demonstrate the impact on the solution.

In chapter 7 we extend the moving mesh method to two horizontal dimensions. We rewrite the method in a weak formulation, so that we may discretise the method using a finite element approximation. Again we use a test scenario to assess the movement of the mesh, before testing against the EISMINT scenario.

We extend the 3D-Var algorithm to be applied to the 2D moving mesh method in chapter 8. We determine the components of the algorithm for use with a 2D moving finite element model. Using a twin experiment we test the 3D-Var scheme, demonstrating an improved estimation to the true ice thickness profile. We then discuss the extended algorithm and the options available to apply the algorithm, with the benefits and difficulties of each.

Finally, in chapter 9 we summarise the conclusions made throughout this thesis and discuss the limitations of the methods introduced. We highlight potential extensions for future development of these methods.

# Chapter 2

## Glaciology

In this chapter we examine the rheology of ice and the way this has been implemented into a definition for the interior deformation for use within mathematical models. We examine the full Stokes equations in the context of dynamical ice flow and the simplification to the Shallow Ice Approximation (SIA). We detail the assumptions that are made in this assumption order to compute forecasts, with a detailed look at the equations that will be used in this thesis.

### 2.1 Introduction

Glaciers and Ice Sheets are subjects of much speculation over their contribution towards sea level rise as ice melts in response to climate change. As ice is removed from the glacier system the behaviour of the remaining ice can change dynamically as a response to this melting. It is therefore important to understand the processes that drive dynamical glacier flow in order to accurately simulate changes that may occur.

At this stage it is worth introducing a few definitions to describe the different features of grounded ice:

- **Ice Sheet** - A glacier of considerable thickness and more than 50,000 sq. km in area, generally slow moving across a large scale. However, they tend to feed

many outlet glaciers. Currently only Antarctica and Greenland are classed as ice sheets.

- **Ice Cap** - Ice caps are a dome-shaped cover of perennial snow and ice. They are classified as small ice sheets, generally less than 50,000 sq. km in size.
- **Ice Stream** - Ice streams are channelised glaciers that flow more rapidly than the surrounding body of ice.
- **Alpine Glacier** - A glacier occupying a valley, usually high in mountainous terrain.
- **Outlet Glacier** - Glaciers which emerge from larger ice sheets but are constrained like alpine glaciers.
- **Glacier Front** - The moving boundary of ice that advances or retreats.
- **Ice Divide** - A topographic separation of either multiple glaciers or a glacier/rock interface where there is zero horizontal velocity.

There exists a variety of mathematical models to describe the movement of ice, ranging in complexity. We now present the key driving forces behind the movement of ice before presenting a selection of these models, concentrating solely on ones which apply to grounded ice.

## 2.2 Ice Rheology

For the most part ice sheets and glaciers are made up from *Polycrystalline ice*, where the composing crystals vary in orientation and size. This is due to the formation of ice from snowflakes landing with randomly distributed grains, leading to the overall behaviour of ice being treated as isotropic [48]. The behaviour of ice is not always isotropic and work has been done on implementing anisotropic behaviour into models developed for isotropic ice (see e.g. [73]). In this work we shall retain isotropic ice

behaviour.

Under low levels of stress ice behaves in a viscoelastic manner, whereas under larger levels of stress the elastic effect is negligible and the ice behaves like a non-linear, non-newtonian fluid. In general ice is treated as viscous with the elastic behaviour ignored.

In an ideal world a mathematical equation linking together the key components of stress, rate of strain and ice properties such as temperature would exist to describe dynamical ice flow. However this has not yet been discovered, if indeed such a relationship exists at all. In order to gain some understanding of how ice moves, some simplifications need to be made. If it is assumed that ice is incompressible, a not unreasonable assumption in most cases, then the strain rate ( $\epsilon$ ) is proportional to deviatoric stress ( $\sigma'$ ) [82]. This provides a common constitutive relationship acting in the cartesian directions  $x, y, z$ :

$$\dot{\epsilon}_{ij} \propto \sigma'_{ij}, \quad i, j = x, y, z. \quad (2.1)$$

The most commonly used relationship is Nye's generalisation of Glen's flow law [40; 83]

$$\dot{\epsilon}_{ij} = A \left( \frac{\dot{\epsilon}_e}{A} \right)^{1-1/n} \sigma'_{ij} \quad (2.2)$$

where  $A$  and  $n$  are flow law parameters and  $\dot{\epsilon}_e$  is the effective strain rate. Most dynamical modelling of ice flow is based upon extracting the velocity field from this relationship, which works well but is by no means a complete description of ice flow.

The two flow law parameters are unknown quantities which have empirical estimates from laboratory experiments. Generally it is accepted that the flow law exponent  $n = 3$  is sufficient in the majority of cases [108; 44]. For the rate factor  $A$ , a modification is made to the Arrhenius equation to fit the laboratory and field data [44]:

$$A = A_0 \exp \left[ -\frac{Q}{RT} + \frac{3C}{(T_0 - T)^k} \right], \quad (2.3)$$

where  $T$  is the temperature of the ice and the remaining variables are constant with values are given in Table 2.1. The flow law parameter in Eq. (2.3) is dependent on the temperature of the ice and has a log-linear relationship, except close to the melting point. The variability in  $A$  is quite drastic and has a large influence on the speed of

Symbol	Value	Definition
$A_0$	$9.302 \cdot 10^{-2} Pa^{-3} yr^{-1}$	Normalising factor
$Q$	$7.88 J(mol)^{-1}$	Activation energy
$R$	$8.314 J(molK)^{-1}$	Gas constant
$T_0$	$273.39 K$	Reference temperature
$C$	$0.49836 K^k$	Empirical constant
$k$	1.17	Unitless constant

**Table 2.1:** Table of typical values for Hookes modified Arrhenius equation. [13]

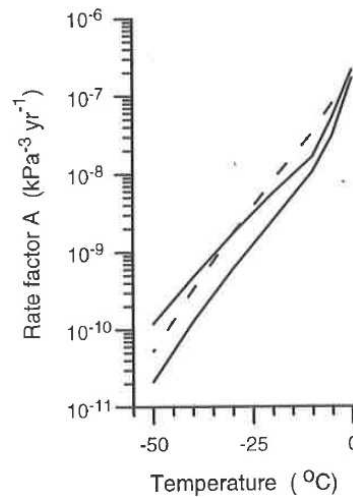


**Figure 2.1:** The rate factor  $A$ , determined by [27; 44]. The value of  $A$ , and as a result the speed at which ice diffuses varies dramatically as the temperature of the ice changes. (Image from [102])

the ice flow (see Figure 2.1).

Glen's flow law is not the only relationship between stress and strain. An alternative is the Smith-Morland flow law [94], which solves the problem of infinite viscosity when  $\sigma_e \rightarrow 0$  that can occur within Glen's flow law. According to [94] it also fits the laboratory experimental data better than Glen's flow law, though since is not widely used we shall retain the use of Glen's flow law in this thesis. There are also flow laws for dealing with

anisotropic ice (see [5; 38]), which we will not consider here.

## 2.3 Mass Continuity

The mass continuity of ice may be derived by considering a column of ice stretching from the base to the surface (see Figure 2.2).

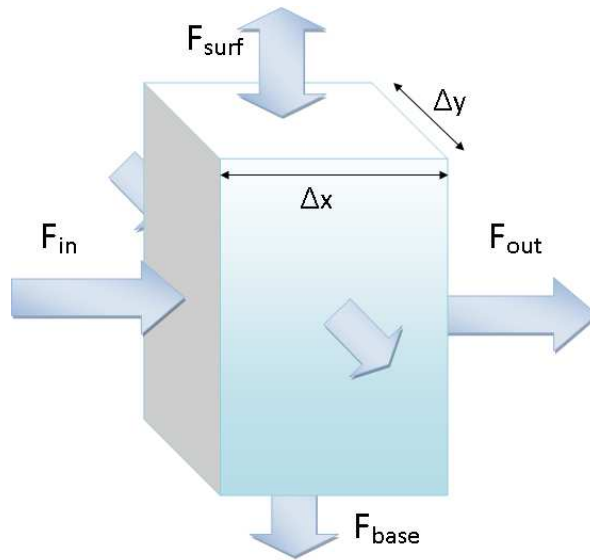


**Figure 2.2:** Mass changes in a column of ice (Modified from [10])

The flux of ice entering this column from the rest of the glacier is given by:

$$F_{in} = \text{inflow in x-direction} + \text{inflow in y-direction} \quad (2.4)$$

$$= hu^x \Delta y + hu^y \Delta x. \quad (2.5)$$

where  $h = h(\mathbf{x}, t)$  is the thickness (or height) of the ice and  $(u^x, u^y)$  is the ice velocity in the Cartesian directions. The ice leaving the column is expressed by:

$$F_{out} = \text{outflow in x-direction} + \text{outflow in y-direction} \quad (2.6)$$

$$= (h + \Delta h)(u^x + \Delta u^x) \Delta y + (h + \Delta h)(u^y + \Delta u^y) \Delta x. \quad (2.7)$$

Mass can also differ in the column due to accumulation/ablation at the surface and melting/refreezing at the base,

$$F_{surf} = m_s \Delta x \Delta y \quad (2.8)$$

$$F_{base} = m_b \Delta x \Delta y, \quad (2.9)$$

where  $m_s$  and  $m_b$  is the mass flux at the surface and base respectively and can be positive or negative. The change in volume therefore is:

$$\frac{\partial V}{\partial t} = \frac{\partial h}{\partial t} \Delta x \Delta y = F_{in} - F_{out} + F_{surf} + F_{base} \quad (2.10)$$

$$\begin{aligned} &= -(u^x \Delta h + h \Delta u^x) \Delta y - (u^y \Delta h + h \Delta u^y) \Delta x \\ &\quad + m_s \Delta x \Delta y + m_b \Delta x \Delta y + \mathcal{O}(\Delta^3) \end{aligned} \quad (2.11)$$

Ignoring higher order terms, we divide through by  $\Delta x \Delta y$ , leaving the change in ice thickness as  $\Delta x, \Delta y \rightarrow 0$ :

$$\frac{\partial h}{\partial t} = -\frac{u^x \Delta h + h \Delta u^x}{\Delta x} - \frac{u^y \Delta h + h \Delta u^y}{\Delta y} + m_s + m_b \quad (2.12)$$

$$= -\frac{\partial(hu^x)}{\partial x} - \frac{\partial(hu^y)}{\partial y} + m_s + m_b \quad (2.13)$$

$$= -\nabla \cdot (h\mathbf{u}) + m \quad (2.14)$$

Eq. (2.14) is an equation of mass conservation as defined in [72], incorporating diffusivity and an external source term.

## 2.4 Models

The mass continuity equation (Eq. (2.14)) can describe the movement of ice thickness over the glacial domain, provided we are given the source term,  $m$ , and a description of the flow velocity,  $u$ . The source term is provided from external information, while the internal flow velocity requires further information. The most complete mathematical

description of dynamical ice flow comes from the set of full Stokes equations, which we will detail here. Due to the complexity of these equations many approximations to these equations have been made under different assumptions. We will also detail here the most commonly used simplification, the Shallow Ice Approximation (SIA) which we use throughout this thesis.

### 2.4.1 Full Stokes model

The full Stokes equations for ice sheets begin with the equations of motion [48]:

$$\frac{\partial \rho}{\partial t} + \nabla \cdot (\rho \mathbf{u}) = 0, \quad (2.15)$$

$$\rho \left( \frac{\partial \mathbf{u}}{\partial t} + (\mathbf{u} \cdot \nabla) \mathbf{u} \right) = -\nabla p + \nabla \cdot \sigma' + \rho \mathbf{g}, \quad (2.16)$$

where  $\rho$  is density,  $\mathbf{u}$  is velocity,  $p$  is pressure,  $\sigma'$  the deviatoric stress tensor and  $\mathbf{g}$  body forces. Ice is a slow moving body, which means the acceleration terms in the momentum equation are negligible. In addition there is very little change of density with depth or temperature, as the layers of snow and firn (old snow) are shallow compared to the main body of ice; in other words the body of ice may be treated as incompressible. Lastly the only body force acting on ice is gravity. Therefore the equations of motion Eqs. (2.15) and (2.16) can be written in the form

$$\nabla \cdot \mathbf{u} = 0, \quad (2.17)$$

$$\nabla p = \nabla \cdot \sigma' + \rho g. \quad (2.18)$$

Development of full Stokes models is still in its infancy. Currently a typical Stokes model will take a long time to run on a serial computer [56; 55]; however, there is an open source code available which is designed to run on parallel systems to reduce computational time [1].

### 2.4.2 Shallow Ice Approximation (SIA)

One of the most widely used simplifications of the Stokes equations is the Shallow Ice Approximation (SIA). It is a zero-order model and while it is generally considered to

be a coarse approximation; computationally it is very cheap. The SIA is based upon three primary assumptions [48]:

Firstly the ice sheet is considerably wider than it is thick, and the gradients are small. i.e.

$$\Delta z \ll \Delta x, \Delta y. \quad (2.19)$$

This is a reasonable assumption, as  $\Delta x, \Delta y \sim \mathcal{O}(100km+)$  and  $\Delta z \sim \mathcal{O}(1km)$ . Secondly it is assumed that the flow of ice is primarily in the horizontal directions, with

$$u^z \ll u^x, u^y, \quad (2.20)$$

Again this is a reasonable assumption for many scenarios; for example the Vostok ice core showed it took  $\sim 400,000$  years for ice to travel  $\sim 3km$  in depth [87]. This means that the vertical strain rate  $\epsilon_{zz}$  is set to zero. Thirdly, the assumption is that the change in stress and consequently, strain, is negligible in the horizontal directions compared to vertically. i.e.

$$\frac{\partial \sigma_{xz}}{\partial x} = \frac{\partial \sigma_{yz}}{\partial y} = 0. \quad (2.21)$$

Applying these three assumptions leaves the following equations

$$\frac{\partial u^z}{\partial z} = - \left( \frac{\partial u^x}{\partial x} + \frac{\partial u^y}{\partial y} \right), \quad (2.22)$$

$$\frac{\partial p}{\partial x} = \frac{\partial \sigma_{xz}}{\partial z}, \quad (2.23)$$

$$\frac{\partial p}{\partial y} = \frac{\partial \sigma_{yz}}{\partial z}, \quad (2.24)$$

$$\frac{\partial p}{\partial z} = \rho g. \quad (2.25)$$

Since density is constant, we may depth average Eqs. (2.22) to (2.25) to further reduce the number of variables to find the flow velocity  $u$ , using Glens flow law (Eq. (2.2)) to give

$$\mathbf{u} = - \frac{2A}{n+2} \rho^n g^n h^{n+1} |\nabla s|^{n-1} \nabla s, \quad (2.26)$$

where  $s$  is the surface elevation. The combination of Eqs. (2.14) and (2.26) provides a full description of the shallow ice approximation [48; 77]. Further details on how to get from the balance equations to Eq. (2.26) can be found in [48; 102; 13].

### 2.4.3 Other Models

There are many models which sit within the spectrum between full Stokes and the SIA. Most of these sit within a class of models known as Longitudinal Stress Approximations. The general aim here is to start with the SIA and re-introduce horizontal gradients of longitudinal stress into the momentum equations, which result in changes to the constitutive relationship Eq. (2.2). The variations in the methods of including this stress and the approximations made provide a variety of models [43], for example one of the main models in this class computes the longitudinal stresses on various layers throughout the ice sheet [85; 14], as opposed to at the surface like most of the models in the class, e.g. [71]. While each of these provides a better approximation than the SIA, the increased level of complexity means there are fewer examples out there with which to test our numerical method. As such the SIA will be used throughout this thesis.

## 2.5 Summary

In this chapter we examined the rheology of ice and the definitions of stress and strain. We showed how these concepts relate to form a flow law describing the deformation of ice under its own weight.

We then derived the mass continuity equation by considering the fluxes into a column of ice to obtain the main equation that will be used in this thesis.

Lastly, we detailed the full Stokes equations for conservation of momentum in glacier flow, before making a number of assumptions to simplify these equations to the shallow ice approximation.

# Chapter 3

## Numerical Modelling

In order to solve differential equations such as the shallow ice equation in glaciology we turn to numerical methods to approximate the solution of the mathematical equations. In this chapter we look at the different types of adaptive mesh modelling and the benefits they have over traditional fixed grid methods. We introduce a type of adaptive mesh model where the nodes of the mesh are moved in accordance to a prescribed requirement — that the relative mass is conserved throughout, to provide a dynamical evolution of the mesh. We then discuss the types of adaptivity that have been used within numerical models of ice sheets and define some terminology for use in this thesis.

### 3.1 Introduction

Many physical problems are evolutionary in nature and can be represented in mathematical terms by time dependent partial differential equations (PDEs). Of these physical problems many are non-linear in nature, exhibit unpredictable behaviour and contain localised transient features which are difficult to approximate numerically. Traditionally, standard numerical solutions to these PDEs are achieved by taking the physical domain and solving on a computational one by dividing the domain into a set of grid points. The solution is then approximated on each grid point and pieced together to gain an overall picture across the domain. Evolutions of the approximate solution to

the differential equations upon this domain then formulate solutions over space and time.

The basic form of a numerical scheme is a so-called fixed grid method, which has a rigid regular structure that is generally well understood and straightforward to achieve. There are however limitations in this approach. For instance, in some areas of the domain there may be features that exhibit sharp changes in some quantity over small spatial scales, the most obvious being a steep physical gradient. The ability to represent these features is limited by the distance between grid points. Since the grid is generally uniform, reducing the distance between grid points will decrease the spacing globally, which increases the resolution of the numerical solution and achieves greater accuracy. However increasing the resolution across the whole domain also increases the computational time, sometimes to an impractical level.

Another limitation with fixed grid structures lies with problems where the domain in question alters in size. To resolve this the computational domain needs to be large enough to cover any change in size that potentially could occur. This leads to a number of grid points effectively going unused, which uses more computational time. In addition the location of some features, such as the boundary, will require interpolation or extrapolation to resolve their location on the domain.

With these limitations in mind a number of alternative methods exist that modify the structure of the numerical domain to reduce errors in the solution.

## 3.2 Adaptive Meshes

As an alternative to formulating a numerical solution on a rigid structured domain, it can be beneficial to adapt the grid and the numerical solution to suit the problem. These methods have existed for many years with the aim of creating irregular grids on which to numerically approximate a more accurate solution than a fixed grid method. Adaptive meshes provide an efficient simulation for many physical problems. Broadly speaking these adaptive schemes can be split into three main categories;

- *h-refinement* - The spatial mesh is refined in regions where higher accuracy, and thus increased resolution is required. This increases the number of nodes by subdividing the relevant mesh cells.
- *p-refinement* - The order of numerical approximation is increased locally in areas where more accuracy is needed.
- *r-refinement* - Also known as moving mesh methods. The number of nodes remains constant but the location of these nodes are distributed across the grid to areas where they can provide the most information.

In addition these types of refinement can also be combined to improve the robustness of the representations (see e.g. [6]).

As a compromise between fixed grid and adaptive mesh methods, the *h*- and *p*-refinement techniques can be used at an initial time to provide greater accuracy in required areas. These methods are still fixed grid methods with a predetermined variable resolution. They do however require prior knowledge, exact or estimated, in order to determine the location for the refinement, which will in general change with time.

Instead it is preferable for adaptive meshes to respond to the evolution as part of the adaptive process such that the refinement is performed automatically. To implement such schemes a *solution indicator* is required to determine the adaption. There are many methods for defining the solution indicator: the most common is the use of error estimates; however, a variety of other techniques exist.

The dynamical ice flow model presented in this thesis contains features where high resolution is required, most critically close to the location of the moving glacier front. In steady state the location of these features would be known and a pre-refined or *h-refinement* technique would be applicable. However glaciers are rarely in a steady state and the boundary is constantly moving over time. For a domain that is frequently changing shape and size, *r-refinement* techniques are well suited to provide an efficient approximation as the moving boundaries are implicitly defined.

While the use of *r-refinement* methods tend to be less popular than other adaptive techniques, they can be incredibly useful in numerical approximations. In particular

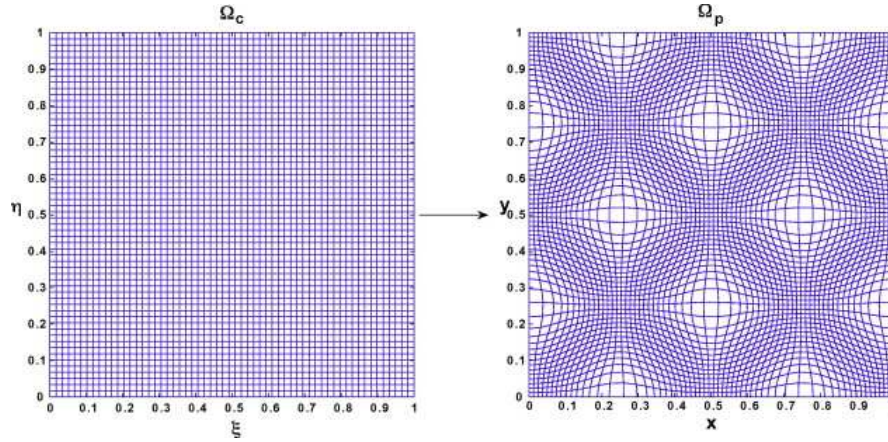


**Figure 3.1:** Example mesh mapping from a uniform computational domain (left) to an irregular physical domain (right). [17]

the time-dependent expanding or contracting nature of many problems can be better approximated without the need for extra grid points. It can also be demonstrated that, in one-dimensional problems at least, *r-refinement* methods can resolve sharp transient features without the need for an excessive increase in mesh nodes [74].

There exists a number of techniques for generating the nodal movement in moving mesh methods, which can be classified into two subcategories; location and velocity based methods [22].

In location based methods the mesh is redistributed at each time step by directly redefining the positions of the nodes. This generally involves mapping from a uniform computational grid to the *r*-refined physical grid, like the 2D example in Figure 3.1. The mappings for these methods are often found by minimising some functional related to a mapping indicator, sometimes known as a monitor function. One such indicator is the equidistribution principle (e.g. [46; 12]) which chooses some property, such as the arc length, to be distributed evenly over the physical domain. Another commonly used indicator is the energy of a harmonic mapping [100]. The construction of these mappings is straightforward in one dimension, but can be more difficult in higher dimensions [8]. In addition they need to be converted to velocities for incorporation into time-dependent PDEs such as the mass continuity of ice, Eq. (2.14).

Velocity based techniques solve for the time derivative of the nodal positions, known

as the mesh velocity. The mesh velocity field is then integrated to provide the new mesh. As these methods are similar to Lagrangian type methods used in fluid dynamics they suffer from some of the same deficiencies, such as mesh tangling [18].

In the work of Miller and Miller [76] the mesh movement is approximated by minimising the PDE residual in a finite element framework. A deformation map method has also been used by a number of authors [66; 20]. Cao *et al.*[21] have used the geometric conservation law (GCL) to form a functional to find the velocity through minimisation.

A similar approach uses a local conservation principle, a modified version of the GCL, to directly find discrete velocities [7], which we will now describe in more detail such that it may be applied to the glaciology problem in this thesis.

### 3.3 A Relative Mass Conservation Method

One approach for defining the velocity at any time interval is the BHJ method [7; 8]. This method is applicable to any mathematical model that is a balance between the rate of change of a volumetric quantity, the flow of said quantity across the volume boundary (known as flux) and any potential source or sink, where there is a change to the overall mass of the domain. As such the monitor function is chosen to control the relative mass of a set of subdomains which cover the entire domain and may overlap. Consider a non-mass conserving PDE of the form

$$h_t = \mathcal{F}(h) + m, \quad (3.1)$$

where  $t$  is time,  $h = h(\mathbf{x}, t)$  is a positive dependent variable such as mass,  $\mathcal{F}$  is a nonlinear spatial operator containing a combination of  $h$  and its spatial derivatives, and  $m$  is a source function independent of  $h$ . The total mass may be found by integrating the dependent variable over the entire domain and is defined by

$$\theta = \int_{\Omega(t)} h d\mathbf{x}. \quad (3.2)$$

Since the PDE, Eq. (3.1), is non-mass conserving the variable  $\theta$  varies over time, so a relative mass conservation principle is introduced by normalising the mass in any

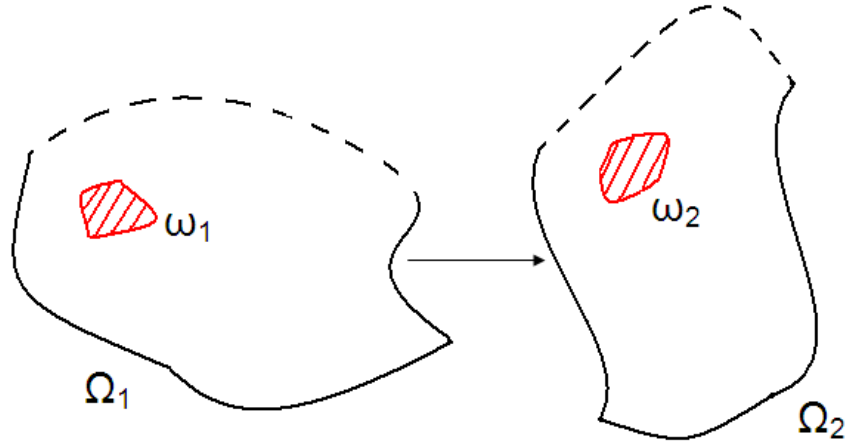


**Figure 3.2:** *Relative mass conservation concept for a velocity based moving mesh method. The mass of  $\omega_1$  and  $\omega_2$  as a fraction of the total mass  $\Omega_1$  and  $\Omega_2$  respectively are identical but the absolute mass is allowed to vary.*

subdomain by the total mass and keeping it constant in time [7]. This principle is demonstrated in Figure 3.2 for the subdomain  $\omega(t)$  of  $\Omega(t)$ . Mathematically the principle may be written as

$$\frac{1}{\theta} \int_{\omega(t)} h d\mathbf{x} = \mu(\omega), \quad (3.3)$$

where  $\mu$  is a constant for each subdomain, independent of time. Note that in the special case where  $\omega = \Omega$ , then  $\mu = 1$ . Eq. (3.3) applies a constraint to the PDE (Eq. (3.1)), from which the motion of the domain  $\Omega$  and its interior may be inferred.

To generate the velocity for the interior nodes based upon the relative conservation principle, we rearrange Eq. (3.3) and differentiate with respect to time. This can then be written in the modified Lagrangian form

$$\frac{d}{dt} \left( \int_{\omega(t)} h d\mathbf{x} \right) = \dot{\theta} \mu(\omega), \quad (3.4)$$

where  $\dot{\theta}$  is the temporal derivative of the total mass  $\theta$ . The Reynolds Transport Theorem [78; 110] (see Appendix B.4) can then be applied to transform it into an Eulerian form which explicitly contains the velocity. This velocity represents the deformation of the domain and is not necessarily the same as the flow velocity, e.g.  $\mathbf{u}$  in Eq. (2.26). Under

this transformation Eq. (3.4) becomes

$$\int_{\omega(t)} h_t d\mathbf{x} + \oint_{\partial\omega(t)} h\mathbf{v}\cdot\mathbf{n}d\Gamma = \dot{\theta}\mu(\omega), \quad (3.5)$$

where  $\mathbf{v}\cdot\mathbf{n}$  is the normal boundary velocity for the boundary  $\partial\omega$  of the region  $\omega$ . By applying the Divergence Theorem to the surface integral, Eq. (3.5) can be written as

$$\int_{\omega(t)} \{h_t + \nabla\cdot(h\mathbf{v})\} d\mathbf{x} = \dot{\theta}\mu(\omega), \quad (3.6)$$

where  $\mathbf{v}$  is any sufficiently smooth velocity field that coincides with the normal velocity at the boundary. Note that  $h_t$  can be taken from the original PDE, Eq. (3.1), to leave

$$\int_{\omega(t)} \nabla\cdot(h\mathbf{v})d\mathbf{x} = \dot{\theta}\mu - \int_{\omega(t)} (\mathcal{F}(h) + m) d\mathbf{x}. \quad (3.7)$$

The rate of change in total mass  $\dot{\theta}$  can be found using the special case  $\omega = \Omega$ , such that Eq. (3.7) simplifies and rearranges to

$$\dot{\theta} = \int_{\Omega(t)} (\mathcal{F}(h) + m) d\mathbf{x} + \int_{\omega(t)} \nabla\cdot(h\mathbf{v})d\mathbf{x}, \quad (3.8)$$

$$= \int_{\Omega(t)} (\mathcal{F}(h) + m) d\mathbf{x} + \oint_{\partial\Omega(t)} (h\mathbf{v})\cdot\mathbf{n}d\Gamma, \quad (3.9)$$

where we have applied the Divergence Theorem (see Appendix B.5). The rate of change in total mass can then be explicitly found provided that  $h = 0$  or  $\mathbf{v}\cdot\mathbf{n}$  is prescribed on the boundary.

In problems of one spatial dimension Eq. (3.7) reduces to an explicit equation for the velocity field,

$$v = \frac{1}{h} \left[ \dot{\theta}\mu - \int_0^{\hat{x}(t)} (\mathcal{F}(h) + m) dx \right], \quad (3.10)$$

for some subdomain  $(0, \hat{x}(t))$  of the domain  $[0, b(t)]$ .

In higher spatial dimensions Eq. (3.7) is not sufficient to determine a unique solution  $\mathbf{v}$ , for which an additional constraint is required. Here we follow [21] in prescribing the vorticity, the curl of the velocity field  $\mathbf{v}$ . In particular, by assuming that the flow is irrotational, the curl of the velocity field is zero. Therefore there exists a velocity potential  $\psi$  such that

$$\mathbf{v} = \nabla\psi. \quad (3.11)$$

Substitution into Eq. (3.7) then gives a unique solution for the velocity potential (to the extent of a constant), with  $h = 0$  or  $\mathbf{v} \cdot \mathbf{n}$  prescribed on the boundary. The velocity field  $\mathbf{v}$  can then be recovered from Eq. (3.11) [21]. The evolution of mesh nodes  $\mathbf{x}$  of the domain can be found from

$$\frac{d\mathbf{x}}{dt} = \mathbf{v}. \quad (3.12)$$

Additionally the evolution of the total mass can be determined by integrating

$$\frac{d\theta}{dt} = \dot{\theta}, \quad (3.13)$$

substituting for  $\dot{\theta}$  from Eq. (3.9).

Finally the solution  $h$  can be recovered from the relative conservation principle, Eq. (3.3), at the new time in the form

$$\left[ \frac{1}{\theta} \int_{\omega} h d\mathbf{x} \right] = \mu(\omega) = \left[ \frac{1}{\theta} \int_{\omega} h d\mathbf{x} \right]^{t=0}, \quad (3.14)$$

where  $t = 0$  represents the initial time. The RHS of Eq. (3.14) is known from initial conditions.

We call this the conservation of mass fraction (CMF) moving mesh method and an algorithm for this method based upon the above argument is as follows:

### ***CMF Moving Mesh Procedure***

1. *Initially:* Compute the total mass  $\theta$  (from Eq. (3.2)) and the relative conservation constants  $\mu(\omega)$  (in Eq. (3.3)) at the initial time.
2. Calculate the temporal derivative of the total mass  $\dot{\theta}$  from Eq. (3.9), assuming that  $h = 0$  or  $\mathbf{v} \cdot \mathbf{n}$  is given on  $\partial\Omega$ .
3. Find the velocity field  $\mathbf{v}$  from Eq. (3.7), using a velocity potential in more than one dimension.
4. Advance the nodes of the mesh in time using Eq. (3.12) and a suitable time-stepping scheme.

5. Update the total mass at the new time from Eq. (3.13), again with a suitable time-stepping scheme.
6. Recover the solution  $h$  at the new time step from the relative conservation principle Eq. (3.3).
7. Repeat steps 2 – 6 until the desired final time.

This algorithm will be applied to the shallow ice equations in later chapters of this thesis. While there is no formal proof available, experience has shown that the mesh points tend to move to areas where higher resolution is required, most likely because it relies on physical properties of the model to generate the mesh velocity.

### 3.4 Adaptive Ice Sheet Models

In general the use of adaptive methods in the glacial modelling community has been limited. The majority of numerical solutions to the ice sheet equations are fixed grid methods with either fixed resolution or a predetermined variable resolution. Variable resolution methods are useful when the areas that require greater accuracy are known in advance; however, the problem of modelling the moving terminus of the glacier is not conducive to variable resolution methods.

The nature of the ice sheet equations can cause the modelling results to suffer from numerical problems. The spacing between grid points is critically important, especially in certain areas such as the moving front which exhibit steep gradients. However, limitations in computational power provide a limit on the resolution of the grid. Numerical errors may initially start small, but increase non-linearly over time with the high level of non-linearity in the mathematical equations [101].

There is therefore a strong argument for the use of adaptive grids within dynamical ice flow modelling. We summarise the situation below.

#### Fixed Grids

Of the fixed grid approaches there exists multiple ways to discretise the domain to

obtain a solution. The most popular is a finite difference type approach, which uses a regular grid to allow easy calculation of the ice flux and velocities at the nodes (for example [19; 45]). Furthermore, solving the equations on staggered grids, where some variables are approximated between the nodes can help to reduce numerical inconsistencies (see e.g. [86]).

A small number of methods use a finite element procedure, where the problem is solved using a set of equations derived from the weak formulation of the governing equations. The finite element method allows for a greater flexibility in the domain structure; however, the resulting solutions can be computationally expensive. The best example of a fixed finite element method is the model of Antarctica shown in [35; 36; 81], while there is also the open source code Elmer/Ice which contains solvers for various problems [1]. A finite volume method has also been employed on non-regular grids, such as in [53; 60].

### **Adaptive Meshes**

The most common type of adaptivity used are *h-refinement* techniques. Within the ice sheet modelling community there have been a few attempts at applying these methods. The first notable attempt appears in 1996 when Lam and Dowdeswell tested a number of existing h-refinement methods within a finite volume shallow ice model [62]. As in this thesis, the authors were concerned with the accuracy achieved in modelling the moving front of the glacier. They concluded that while the adaptivity has little effect on the steady state solution, the motion of the boundary was significantly smoother with less spurious fluctuations than with a comparable unrefined fixed grid method. This came at a computational cost roughly 1.8 times higher.

The first known *h-refinement* method to include two horizontal dimensions appears in Starr [97], where the author demonstrates the potential accuracy gains as well as the improvement in computational cost to meet similar levels of accuracy. In addition, many h-refinement methods use the AMR (adaptive mesh refinement) technique, which contains a fine mesh where required with a series of 'blocks' of decreasing levels of refinement moving further away from the dense regions. For example [23] uses the

method within a finite element framework to develop error estimates and the likes of [39; 24] use AMR to estimate the point at which an ice sheet begins to float, known as the grounding line. While not developed specifically for ice sheet modelling, the Parallel Hierarchical Adaptive MultiLevel Project (PHAML) has recently been integrated into the community ice sheet model (CISM) to allow a combined *hp-adaptive* method for this next generation ice sheet model [112].

A location based *r-refinement* method is introduced in [43], where a one-dimensional flowline model is approximated on a stretchable grid. The stretched grid is transformed onto a fixed computational domain  $\xi \in [0, 1]$ , similar to Figure 3.1. The one-dimensional version of the shallow ice equations (Eq. (2.14)) can then be written in the transformed co-ordinates as

$$\frac{\partial h}{\partial t} = -\frac{1}{b(t)} \frac{\partial hu}{\partial \xi} + \frac{\dot{b}(t)}{b(t)} \xi \frac{\partial h}{\partial \xi} + m \quad (3.15)$$

where  $b(t)$  represents the moving glacial front. A good comparison between this method and similar fixed grid approaches for approximating the glacial grounding line can be found in Vieli [105], which concluded that the stretched grid approach is more robust than the fixed grid methods which were sensitive to the horizontal grid spacing. There is further development of this stretched grid method applied to the grounding line problem in [93].

Additionally the Ice Sheet System Model (ISSM) developed by NASA is a location based adaptive method that uses the surface velocity to reduce errors [63].

At present it appears that there has been no attempt at applying a velocity-based *r-refinement* method to the dynamical ice flow problem. These methods are more widely used in the field of oceanography and efforts have been made in the related field of sea ice dynamics [107].

This thesis will develop the velocity-based CMF moving mesh method introduced in Section 3.3 to the shallow ice equations to assess the ability of this type of method to simulate dynamical ice flow.

### 3.5 Terminology

In much of the literature the definition of the dimensions of the model depends on the author. For the purpose of clarity we define here the definitions used throughout this thesis:

**One-Dimensional Model:-** A model that contains one horizontal dimension and is vertically integrated to a single layer. In some pieces of literature this is referred to as a  $1\frac{1}{2}$ D model.

**Two-Dimensional Model:-** A scenario with two horizontal dimensions, again vertically integrated to a single layer. Sometimes referred to as a  $2\frac{1}{2}$ D model.

In addition the following definitions are proposed to distinguish between fixed and adaptive methods:

**Grid:-** The term 'grid' refers to the numerical domain for fixed grid methods. The structure of the domain is rigid in nature and the grid points are generally evenly distributed.

**Mesh:-** A 'mesh' is the numerical domain within adaptive models. It implies the structure is more flexible and subject to change, either through additional nodal points or the movement of the numerical domain.

## 3.6 Summary

In this chapter we introduced the concept of adaptive mesh techniques and the scenarios in which they provide improvements in terms of accuracy and computational cost, compared with traditional fixed grid methods. In particular we focused on r-refinement methods, referred to hereafter as moving mesh methods. We defined in detail a velocity based moving mesh method that conserves relative mass that will be applied to the shallow ice approximation equations in chapter 5.

We then considered numerical solutions of ice sheet models, examining the previous attempts to apply adaptive mesh techniques to the equations governing dynamical ice flow.

# Chapter 4

## Data Assimilation

In this chapter we introduce the concept of data assimilation, a procedure which uses a combination of a numerical model and observations to produce a statistically best representation of the model variables. We look at the basic aims of data assimilation and the initial set up, before discussing three methods that are commonly used in practice with applications such as numerical weather prediction and oceanography. We then look at the use of data assimilation within the field of glaciology, with a thought to the potential observations that are available for use within the assimilation. Lastly we look at how data assimilation has previously been used with adaptive mesh models.

### 4.1 What is Data Assimilation?

Numerical models are frequently used in physical systems to provide forecasts of the state of the system in the future. While these models can provide good estimates, uncertainties in the initial input data often lead to errors as the simulation evolves.

Similarly it is rare for a complete set of information defining all the required variables and parameters to be observed at a specific time. This information, in the form of measured observations, also contains uncertainty and random noise in addition to being incomplete.

The idea therefore, is to construct a method to combine numerical models with

observations to produce more accurate representations of the current state of the system. This is known as data assimilation (DA) within the fields of climate, atmospheric and oceanic modelling. It does however bear close resemblance to the fields of inverse problems and control theory.

Data assimilation methods combine observations with a discrete dynamical model of the form

$$\mathbf{z}_{k+1} = \mathcal{M}\mathbf{z}_k + (\boldsymbol{\epsilon}_m)_k \quad k = 0, 1, \dots \quad (4.1)$$

where the vector  $\mathbf{z}_k \in \mathbb{R}^q$  is known as the *state vector* and contains every variable within the dynamical model at the time  $t_k$ . The model operator  $\mathcal{M}$  is a nonlinear function that defines the evolution of the state variables from time  $t_k$  to  $t_{k+1}$ . The vector  $(\boldsymbol{\epsilon}_m)_k$  represents the error introduced through the model operator  $\mathcal{M}$ . If we assume the model is perfect [80], then this error may be ignored, with  $(\boldsymbol{\epsilon}_m)_k = 0$ .

In addition, suppose at time  $t_k$  there are  $p$  observations available that can be related to the state vector by

$$\mathbf{y}_k = \mathcal{C}_k\mathbf{z}_k + (\boldsymbol{\epsilon}_o)_k \quad k = 0, 1, \dots \quad (4.2)$$

where the vector  $\mathbf{y}_k \in \mathbb{R}^p$  contains all the observations at time  $t_k$ . The vector  $(\boldsymbol{\epsilon}_o)_k \in \mathbb{R}^p$  contains the observation errors, which are assumed to be uncorrelated and unbiased [65].

It is worth noting that in general the problem is under-determined as there are fewer observations available than elements in the state vector, such that  $p < q$ . This introduces the need for the operator  $\mathcal{C}_k : \mathbb{R}^q \rightarrow \mathbb{R}^p$ , a function known as the observation operator which maps the model variables in the state vector to the predicted values of the observations.

For data assimilation the observations  $\mathbf{y}_k$  are statistically combined with our estimated (or forecast) state vector  $\mathbf{z}_k^f$  to gain the most accurate description of the state of the system, called the *analysis*  $\mathbf{z}^a$ .

## 4.2 Data Assimilation Algorithms

There are numerous variations of data assimilation, each with their own benefits. In general these can be classed into two types of method; *sequential schemes*, which evolve the dynamical model (Eq. (4.1)) to a point in time with available observations, whereby the assimilation procedure occurs before the model continues, and *variational schemes* which incorporate observations from a window of time simultaneously to improve the initial conditions for the dynamical model.

Here we introduce three methods which are commonly used for operational purposes; the first of which is the primary method used in this thesis, while the other two are introduced for discussion purposes. The notation used throughout follows [50] where possible; however, some symbols are changed to avoid confusion with those used in glaciology.

### 4.2.1 3D-VAR

The 3D-VAR method [25; 69; 79] is a variational method based upon a maximum a posteriori probability estimate that considers only the spatial dimensions of the system. The removal of the temporal variation means the 3D-VAR approach is essentially a sequential scheme. The *analysis state* is found by minimising a cost function that balances the model state  $\mathbf{z}_k$  with the forecast state  $\mathbf{z}_k^f$  and observations  $\mathbf{y}_k$ . This cost function takes the form

$$J(\mathbf{z}_k) = \frac{1}{2}(\mathbf{z}_k - \mathbf{z}_k^f)^T \mathbf{B}_k^{-1}(\mathbf{z}_k - \mathbf{z}_k^f) + \frac{1}{2}(\mathbf{y}_k - \mathcal{C}_k \mathbf{z}_k)^T \mathbf{R}_k^{-1}(\mathbf{y}_k - \mathcal{C}_k \mathbf{z}_k) \quad (4.3)$$

where the forecast state comes from an evolution of the dynamical model in Eq. (4.1), applied to the previous analysis solution. i.e.

$$\mathbf{z}_k^f = \mathcal{M} \mathbf{z}_{k-1}^a. \quad (4.4)$$

The matrices  $\mathbf{B}_k \in \mathbb{R}^{q \times q}$  and  $\mathbf{R}_k \in \mathbb{R}^{p \times p}$  are symmetric, positive definite covariance matrices that statistically represent the variances and covariances of the errors in the forecast and observations respectively. In essence these matrices control the balance

between the forecast and observations and can be thought of as a weighting between the two.

The cost function Eq. (4.3) can also be derived from Bayes' Theorem;

$$p(\mathbf{z}|\mathbf{y}) = \frac{p(\mathbf{y}|\mathbf{z})p(\mathbf{z})}{p(\mathbf{y})} \quad (4.5)$$

where the analysis solution is the solution with the maximum probability given the observations  $\mathbf{y}$  and an initial guess  $\mathbf{z}^f$  [59]. Assuming each of the probabilities in Eq. (4.5) is Gaussian, we obtain the cost function in Eq. (4.3).

To minimise this cost function we use iterative techniques such as the Newton algorithm, steepest descent or conjugate gradient, which can be computationally costly. A control variable transform can be applied to increase the efficiency of the iterations and speed up convergence.

### Best Linear Unbiased Estimate

An alternative method to minimising the cost function is to derive an explicit formula for the analysis solution. Differentiating Eq. (4.3) with respect to the model state yields the gradient, given by

$$\nabla J(\mathbf{z}_k) = \mathbf{B}_k^{-1}(\mathbf{z}_k - \mathbf{z}_k^f) + \mathbf{C}_k^T \mathbf{R}_k^{-1}(\mathbf{y}_k - \mathbf{C}_k \mathbf{z}_k) \quad (4.6)$$

where  $\mathbf{C}_k \in \mathbb{R}^{p \times q}$  is the linearised version of observation operator  $\mathcal{C}_k$ . The analysis solution therefore satisfies

$$\nabla J(\mathbf{z}_k^a) = 0. \quad (4.7)$$

Rearranging Eqs. (4.6) and (4.7) and applying matrix identities leads to the Best Linear Unbiased Estimate (BLUE) [65] for the analysis solution

$$\mathbf{z}_k^a = \mathbf{z}_k^f + \mathbf{K}_k(\mathbf{y}_k - \mathbf{C}_k \mathbf{z}_k^f) \quad (4.8)$$

where  $\mathbf{K} \in \mathbb{R}^{q \times p}$  is known as the gain matrix [79], given by

$$\mathbf{K}_k = \mathbf{B}_k \mathbf{C}_k^T (\mathbf{C}_k \mathbf{B}_k \mathbf{C}_k^T + \mathbf{R}_k)^{-1}. \quad (4.9)$$

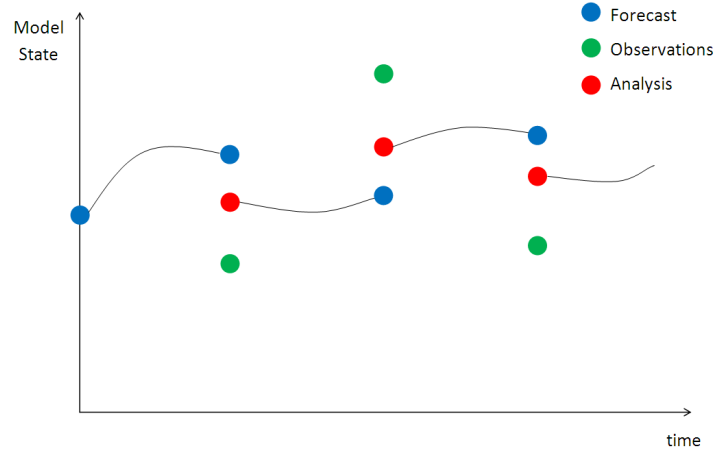


**Figure 4.1:** *Concept cartoon of the optimal 3D-VAR data assimilation scheme, using each set of observations sequentially.*

This gives us a solution that is equivalent to iteratively minimising the cost function and enables the 3D-VAR problem to be solved sequentially [68]. This is shown pictorially in Figure 4.1, where the analysis solution is evolved using the dynamical model in Eq. (4.4) to provide the forecast at the next assimilation time.

We now provide more information about the individual components of Eq. (4.8).

### Observation Operator

Observations of variables in the system are generally unevenly distributed through both space and time and contain gaps where no data is available. It is unlikely that a perfect one-to-one correspondence exists between observations  $y$  and the state forecast  $\mathbf{z}^f$ . The observation operator maps the state vector to observation space so it is directly comparable to the observations by:

$$\mathbf{y}_k = \mathcal{C}_k(\mathbf{z}_k), \quad (4.10)$$

with

$$\mathcal{C}_k : \mathbb{R}^q \rightarrow \mathbb{R}^p. \quad (4.11)$$

Observations occur either as a direct measurement of the dynamical model variables or indirectly via a mathematical relationship.

Using direct observations the observation operator is a linear interpolation matrix of size  $p \times q$ , where each row represents the interpolation of the state vector to an individual observation. The elements of each row then correspond to the coefficients of the interpolation.

For indirect observations the operator  $\mathcal{C}_k$  maps the model variables via a physical relationship to be comparable with the observations and is generally non-linear. For computational purposes this is generally linearised for use in a data assimilation scheme, potentially introducing further error [95].

### Observation Error Covariance Matrix

The symmetric, positive definite observation error covariance matrix  $\mathbf{R}$  statistically describes the uncertainty in the errors contained in the observation vector  $\mathbf{y}$  and is defined as

$$\mathbf{R}_k = E[\boldsymbol{\epsilon}_o \boldsymbol{\epsilon}_o^T]_k, \quad (4.12)$$

where  $E[\cdot]$  denotes the expected value and  $(\boldsymbol{\epsilon}_o)_k = \mathbf{y}_k - \mathcal{C}_k \mathbf{z}_k$ . These errors arise from a number of sources, such as inaccuracies of the measuring instrument, physical features that are too small to represent in the model or errors that occur in the observation operator.

### Background Error Covariance Matrix

The matrix  $\mathbf{B}$  is symmetric, positive definite and referred to as the background error covariance matrix. It is statistically defined as

$$\mathbf{B}_k = E[\boldsymbol{\epsilon}_b \boldsymbol{\epsilon}_b^T]_k, \quad (4.13)$$

where  $(\boldsymbol{\epsilon}_b)_k = \mathbf{z}_k^f - \mathbf{z}_k$  is the difference between the model prediction and the state of the system. These errors arise primarily from errors in the initial conditions of the system.

Arguably the most important part of any data assimilation problem [11], the background error covariance matrix  $\mathbf{B}_k$  is also one of the most difficult to determine since

these errors are unknown and require approximation. In addition to representing uncertainty in the errors in the dynamical model, the elements in  $\mathbf{B}_k$  act to spread the information from observations; i.e. how an observation at a point affects the nearby points or how observations of one type of variable influence other variables [16]. This spreading can be seen in Eq. (4.9) as the matrix  $\mathbf{B}$  is the last operation in the calculation of the gain matrix and is the reason why the background error covariance matrix is so critical to the data assimilation scheme.

### 4.2.2 Kalman Filter

An alternative approach is a sequential method known as the Kalman Filter [57; 58]. The difference between the Kalman Filter and 3D-VAR is the evolution of the background error covariance matrix  $\mathbf{B}$ . With the Kalman Filter this matrix evolves using information from the current analysis and the dynamical model to forecast the covariances to the next assimilation time.

The sequential equation for calculating the analysis state vector is the same as the one used in 3D-VAR, Eq. (4.8):

$$\mathbf{z}_k^a = \mathbf{z}_k^f + \mathbf{K}_k(\mathbf{y}_k - \mathbf{C}_k \mathbf{z}_k^f), \quad (4.14)$$

subject to

$$\mathbf{z}_k^f = \mathcal{M} \mathbf{z}_{k-1}^a. \quad (4.15)$$

The gain matrix is given by

$$\mathbf{K}_k = \mathbf{P}_k^f \mathbf{C}_k^T (\mathbf{C}_k \mathbf{P}_k^f \mathbf{C}_k^T + \mathbf{R}_k)^{-1}. \quad (4.16)$$

Here the background error covariance matrix is expressed by  $\mathbf{P}_k$  to distinguish the method from 3D-VAR. After calculating the analysis state vector, the analysis background error covariance matrix is calculated using the following equation:

$$\mathbf{P}_k^a = (\mathbf{I} - \mathbf{K}_k \mathbf{C}_k) \mathbf{P}_k^f \quad (4.17)$$

This is then explicitly forecast forward using the linearised version of the dynamical model Eq. (4.4);

$$\mathbf{P}_{k+1}^f = \mathbf{M} \mathbf{P}_k^a \mathbf{M}^T, \quad (4.18)$$

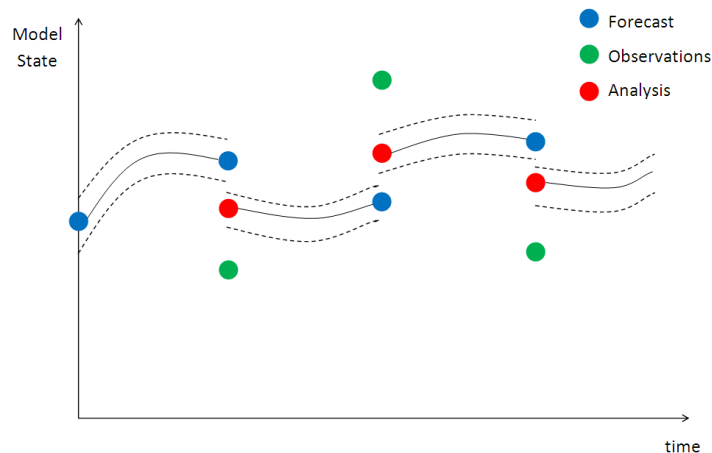


**Figure 4.2:** *Concept cartoon of the Kalman Filter data assimilation scheme, a sequential scheme where the background error covariance matrix (dotted lines) is evolved through time in addition to the solution.*

and the process begins again. This approach means the error covariances are dependent on the model flow and can carry the statistical information about the forecast errors through time rather than assuming fixed error covariances (see Figure 4.2). Information from all the previous assimilation steps are taken into account, making the Kalman Filter an accurate method that is the optimal sequential solution. However in practice the CPU power required to forecast the background error covariance matrix means it is seldom used operationally.

### 4.2.3 4D-VAR

One of the drawbacks with the 3D-VAR approach is that observations are assimilated at set moments in time, which means that unless they are taken at the same moment they need to be interpolated to the required time, which results in a temporal error being introduced. It is generally computationally unfeasible for sequential schemes to assimilate at every time observations occur so we turn to variational schemes to incorporate their distribution in time.

The 4D-VAR data assimilation scheme improves the estimate of the state vector at the initial time [64] so that when the dynamical model evolves the state vector better

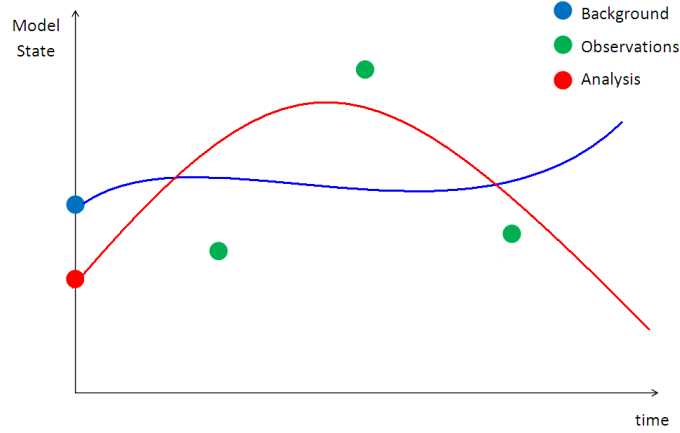


**Figure 4.3:** *Concept cartoon of the 4D-VAR data assimilation scheme, which utilises all observations simultaneously to provide the best estimate of the system state.*

matches the available data (see Figure 4.3). Observations can then taken at the time they occur until the end of a specified time window, the length of which varies depending on the application. The cost function to minimise is then expressed by

$$J(\mathbf{z}_0) = \frac{1}{2}(\mathbf{z}_0 - \mathbf{z}_0^f)^T \mathbf{B}_0^{-1}(\mathbf{z}_0 - \mathbf{z}_0^f) + \frac{1}{2} \sum_{i=0}^p (\mathbf{y}_i - \mathbf{C}_i \mathbf{z}_i)^T \mathbf{R}_i^{-1}(\mathbf{y}_i - \mathbf{C}_i \mathbf{z}_i), \quad (4.19)$$

subject to

$$\mathbf{z}_i = \mathcal{M}(t_0, t_i, \mathbf{z}_0), \quad (4.20)$$

i.e. the state vector at time  $t_i$  is the solution to the dynamical model evolution of  $\mathbf{z}$  at the initial time  $t = 0$ . Eq. (4.19) differs from the 3D-VAR cost function Eq. (4.3) by the introduction of a summation over the observations distributed in time. In order to minimise Eq. (4.19) with respect to the initial state and thus implement a 4D-VAR scheme, the gradient of the cost function requires an adjoint model [31], which steps backward in time but involves linearising the dynamical model. In many cases the adjoint is difficult to calculate, particularly when the dynamical model is highly non-linear. The solution to the 4D-VAR cost function implicitly evolves the background error covariances over the time window. This means that both the Kalman Filter and 4D-VAR methods give an identical analysis at the end of a time window when the dynamical model is linear and the same data is used.

## 4.3 Data Assimilation in Glaciology

Assimilation in the field of glaciology is still very much in its infancy. While its use is common place in atmospheric and oceanic modelling, glaciologists have only recently began to look at incorporating observations into their models.

For example, in [3] observations of the rate of thickness change are used to enforce covariance relationships between the rate of thickness change, the flux divergence and the accumulation rate. In [106] observations of surface velocity are used to reconstruct the flow and stress fields of an Antarctic ice shelf, with the eventual aim of predicting the potential collapse of the shelf.

More recently an adjoint 4D-VAR style method for a flowline model has been developed in [41], where the authors discuss the difficulties in reconstructing the basal stresses within glaciers. Another attempt at constructing a 4D-VAR adjoint method focuses on trying to find the best estimate of the climatic temperature and volume of a flowline model with the aim of extending to a more advanced model in the future [15].

### 4.3.1 Available Observations

In recent times the observational network of ice has improved dramatically. The use of satellites in particular has provided a wealth of information to aid the understanding of glaciological processes [4].

For example, satellite radar altimetry is able to accurately measure the surface elevation of ice sheets [9; 67], while visible imagery can be used to locate the ice extent or key features [52]. More recently the CRYOSAT missions are returning accurate information regarding changes in ice thickness for land ice and values for the thickness of sea ice [30]. The most common observation available is the surface velocity, which can be determined by analysing a succession of radar images, although the change in velocity with depth will then need to be inferred [54].

Sensors fitted to aircraft can provide more detailed information such as the thickness

of the ice [70]. In situ ground measurements tend to give very detailed information but are generally sparse, both temporally and spatially. In particular the accumulation rate of snow to ice is measure by ice-cores and snowpits [103], with some form of interpolation required to cover the entire domain.

Historical data is even more limited, primarily due to ice sheets existing in remote areas of the planet. Sparse information of past surface velocity, changes in thickness and accumulation rate exist, though it is both spatially and temporally limited.

## 4.4 Data Assimilation on Adaptive Meshes

The use of adaptive meshing techniques within data assimilation methods is also an area of interest in its infancy. The application of  $h$ -adaptivity and nested mesh numerical models can be achieved relatively easily [29], whereas  $r$ -adaptive schemes prove more difficult.

It has been determined that location based  $r$ -adaptive methods can be incorporated into an adjoint solution of a 4D-VAR method with benefits to the overall CPU time [33; 34]. The UK Met Office is currently looking at allowing the use of static  $r$ -adaptive methods within their existing 4D-VAR framework. This is achieved by including an additional transformation to simplify the background elements of the cost function [88; 89].

There is however a lack of study into the use of velocity based  $r$ -adaptive meshes within data assimilation. These moving mesh methods directly solve the evolution of the domain, which we may observe through the use of visible imagery yet this information is currently underused.

## 4.5 Summary

In this chapter we introduced the general dynamical model equations and the data assimilation problem used within geophysical fields such as meteorology and oceanog-

raphy. We have given a brief introduction to three commonly used methods, where we discussed the benefits of each. In chapter 6 we will utilize the first of these, the 3D-VAR method, to a moving mesh ice flow model.

We examined the current state of data assimilation in the cryospheric fields and the attempts to apply the techniques to dynamical ice flow models. We discussed the availability of observations, before detailing the application of data assimilation to adaptive mesh methods.

# Chapter 5

## A 1D Moving Glacier Model

In this chapter we begin by looking at the shallow-ice PDE for modelling dynamical glacier flow. We look at how the model is set up and the property of total mass and its evolution over time. We then consider the diffusive element of velocity at the front of the glacier and the condition upon which this value is non-zero and the scenarios to which it applies. We also describe a steady state solution for time-independent accumulation/ablation rates.

Next we describe the application of the BHJ method described in Chapter 3 to the shallow ice model from Chapter 2. We detail the extraction of a net velocity from the conservation of mass fraction, which results in movement based upon both the diffusive flow velocity and the accumulation/ablation terms. From there we will develop a numerical approximation to the equations in this moving mesh method using a finite difference scheme, before demonstrating the method using a simple test scenario. Finally we compare the method to existing numerical models using a standardised scenario.

### 5.1 The Shallow-Ice Glacier PDE

For many glaciers, such as Nigardsbreen in Norway [84], the flow is dominated by movement along the centre of the glaciers, known as the flowline. It is therefore practical to represent these using a one-dimensional model along this flow line. To do this the  $x$ -

component is set to follow the flow line, starting at the top of the glacier with movement in the  $y$ -direction ignored. Recall from Eq. (2.14) the mass balance equation;

$$\frac{\partial h}{\partial t} + \nabla \cdot (h\mathbf{u}) = m, \quad (5.1)$$

which in one-dimension can be simplified to [48]:

$$\frac{\partial h}{\partial t} + \frac{\partial(hu)}{\partial x} = m. \quad (5.2)$$

As before,  $h = h(x, t)$  is the ice thickness and  $m = m(x, t)$  is the ice-equivalent accumulation rate (including the effect of ablation). In Eq. (5.2),  $u = ch^{n+1}s_x^n$  is the diffusive flow velocity of an isothermal ice sheet from Eq. (2.26), describing the movement induced by the ice deforming under its own weight.

A typical domain for a flow line model is shown in Figure 5.1. The left-hand boundary represents the ice divide, a section of ice which is connected to either a rock face [61] or a further expanse of slower moving ice not included in the model domain [111]. Mathematically we treat this section as static and represent this boundary with a no-flux condition at the fixed origin  $x = 0$ ;

$$\left. \frac{\partial h}{\partial x} \right|_{x=0} = 0, \quad \left. u \right|_{x=0} = 0, \quad \left. \frac{dx}{dt} \right|_{x=0} = 0. \quad (5.3)$$

Conversely, at the right-hand boundary (referred to as the ice margin, or moving front) the ice converges to meet the bed [104], but the location of the boundary moves as the front advances or retreats. We will consider glaciers where the gradient at the boundary is negative,  $h_x < 0$ , i.e. the moving front does not overturn on itself. We identify this moving boundary  $x = b(t)$ , with the condition

$$\left. h \right|_{x=b} = 0. \quad (5.4)$$

It is common to non-dimensionalise equations such as Eq. (5.2) that contain physical quantities. We detail this scaling in Chapter 7 when the model is presented in two-dimensional form with the understanding it is also applied to the 1D model.

We now consider the change in mass over the entire domain. The total ice thickness, denoted here by  $\theta(t)$  and defined as

$$\int_0^{b(t)} h dx = \theta(t), \quad (5.5)$$

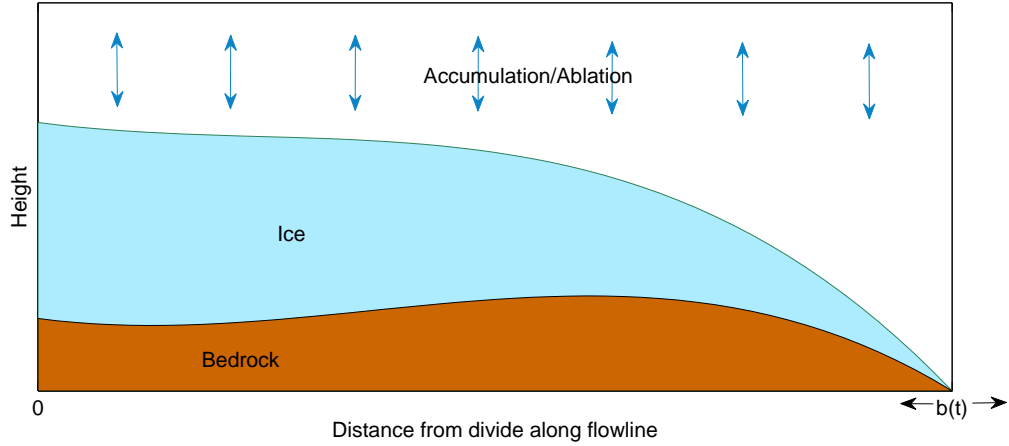


**Figure 5.1:** Glacier domain along flowline from the fixed ice divide at  $x = 0$  to the moving front at  $x = b$

can be differentiated with respect to time to determine the overall change in mass.

Using Leibnitz' integral rule (see section B.1) gives

$$\dot{\theta} = \frac{d}{dt} \int_0^{b(t)} h dx \quad (5.6)$$

$$= \int_0^{b(t)} \frac{\partial h}{\partial t} dx + h \frac{dx}{dt} \Big|_{x=0}^{b(t)} \quad (5.7)$$

Under the boundary conditions (Eqs. (5.3) and (5.4)) the second term is zero. Substituting Eq. (5.2) into Eq. (5.7) leaves

$$\begin{aligned} \dot{\theta} &= - \int_0^{b(t)} \frac{\partial}{\partial x} [hu] dx + \int_0^{b(t)} m dx \\ &= -hu \Big|_{x=0}^{b(t)} + \int_0^{b(t)} m dx \end{aligned} \quad (5.8)$$

Using the boundary conditions again forces the first term to be zero, since at the ice divide we require the ice to remain stationary, implying  $u = 0$ . This leaves the change in ice thickness over the domain as

$$\dot{\theta} = \int_0^{b(t)} m dx. \quad (5.9)$$

As a result any change in the total ice thickness over the whole glacier is due solely to the source term in Eq. (5.9), i.e. the global change in ice thickness equates to the net accumulation/ablation over the whole glacier.

## 5.2 Characteristics of the Shallow Ice PDE Model

We now examine features of the model that provide insight into the behaviour of glaciers under certain conditions. Firstly we consider the diffusive flow component and its impact on the moving glacier front before considering a steady state solution where the ice thickness profile remains constant over time.

### 5.2.1 Diffusive Velocity at the Glacier Front

Glaciers are unique entities as they facilitate an overall advance or retreat of their expanse despite the fact that the diffusive flow is unidirectional. Naturally there will also occur periods where the front is stationary, either at the cross period between advance and retreat or simply a momentary pause in movement (momentary on a glacial time scale). Here we assess the movement of the glacier front generated by the diffusive flow velocity  $u$  in Eq. (5.1).

Under the Shallow Ice Approximation detailed in Section 2.4.2 the 1D diffusive velocity  $u$  in Eq. (5.2) can be written as

$$u = ch^{n+1}s_x^n, \quad (5.10)$$

where  $c = -2A\rho^n g^n / (n + 2)$ , under the assumption that temperature and density are constant throughout the glacier. This means that the parameter  $c$  can be written as a single negative constant. The surface elevation,  $s$ , is the total height of the glacier including the topographical bed as well as the ice thickness. For simplicity we begin by making the further assumption that the bed is flat, with  $s = h$ , so that

$$u = ch^{n+1}h_x^n. \quad (5.11)$$

Expressing the diffusive velocity in the form of Eq. (5.11) suggests a problem when applying the boundary condition  $h = 0$  at  $x = b(t)$ , apparently yielding a zero diffusive velocity and resulting in a boundary that only moves as a result of accumulation or ablation. However, it is perfectly possible for the diffusive velocity  $u$  to be non-zero

when  $h = 0$  and  $h_x$  is infinite such that  $h^{n+1}h_x^n$  is finite.

To demonstrate this we shall perform an analysis on the local profile of the flow velocity, close to the moving front. We begin by utilising the chain rule of differentiation to write Eq. (5.11) in the more useful form

$$u = c(h^{(n+1)/n}h_x)^n = c\left(\frac{n}{2n+1}\right)^n \{(h^{(2n+1)/n})_x\}^n, \quad (5.12)$$

from which it can be seen that the diffusive velocity is finite at the boundary provided that  $(h^{(2n+1)/n})_x$  is finite.

We now wish to analyse the conditions under which Eq. (5.12) provides a non-zero velocity at the boundary. To achieve this we note that the profile of ice thickness must satisfy the boundary condition  $h = 0$  at  $x = b$ , and therefore at any moment in time it must contain the factor  $(b - x)$ . We may then let  $\alpha = \alpha(t) > 0$  be the largest real number such that  $h$  close to the moving boundary  $b$  can be written in the form

$$h = (b - x)^\alpha g(x) \quad (5.13)$$

where the function  $g(x) > 0$  is finite and has a finite derivative at the boundary  $x = b$ . Then

$$h^{(2n+1)/n} = ((b - x)^\alpha g(x))^{(2n+1)/n} = (b - x)^{\alpha(2n+1)/n} G(x), \quad (5.14)$$

where  $G(x) = g(x)^{(2n+1)/n} > 0$  is also finite and has a finite derivative at  $x = b$ . The value of  $u$  in Eq. (5.12) at the boundary is proportional to the derivative of Eq. (5.14), which assuming continuity of  $u$  and  $G$  in the vicinity of the boundary, can be found by taking the limit as  $x$  tends to  $b$

$$\lim_{x \rightarrow b} (h^{(2n+1)/n})_x = \lim_{x \rightarrow b} [\{(b - x)^{\alpha(2n+1)/n} G(x)\}_x]. \quad (5.15)$$

We then note that since both

$$\lim_{x \rightarrow b} [(b - x)^{\alpha(2n+1)/n} G(x)] = 0 \quad \text{and} \quad \lim_{x \rightarrow b} (b - x) = 0,$$

we may employ L'Hopital's rule (see Section B.2), leading Eq. (5.15) to become

$$\lim_{x \rightarrow b} (h^{(2n+1)/n})_x = - \lim_{x \rightarrow b} \frac{(b - x)^{\alpha(2n+1)/n} G(x)}{(b - x)} = - \lim_{x \rightarrow b} (b - x)^{(\alpha(2n+1)/n)-1} G(x). \quad (5.16)$$

It follows that the limit of the diffusive velocity (Eq. (5.12)) is proportional to

$$\lim_{x \rightarrow b} (b - x)^{\alpha(2n+1)-n}. \quad (5.17)$$

Since  $n$  is a given exponent, there exists a critical value for the power  $\alpha$ , denoted  $\alpha_c$ , which leads to the following properties for the diffusive velocity  $u$  at the boundary as  $x \rightarrow b$ ;

$$\text{Case 1: } \alpha > \alpha_c \quad \Rightarrow \quad u \rightarrow 0 \text{ as } x \rightarrow b, \quad (5.18)$$

$$\text{Case 2: } \alpha = \alpha_c \quad \Rightarrow \quad u \text{ remains finite as } x \rightarrow b, \quad (5.19)$$

$$\text{Case 3: } \alpha < \alpha_c \quad \Rightarrow \quad u \rightarrow \infty \text{ as } x \rightarrow b \text{ (momentarily)}. \quad (5.20)$$

where the critical value of  $\alpha$  is given by

$$\alpha_c = \frac{n}{(2n + 1)}. \quad (5.21)$$

Thus the ice diffusion induces no movement at the boundary when the ice thickness profile given in Eq. (5.13) has a value of  $\alpha$  in the range defined by Case 1. As the profile changes over time and  $\alpha$  tends to the critical value  $\alpha_c$  in Eq. (5.21), the Case 2 condition is met and the diffusive velocity is then non-zero. If the thickness profile changes to the form of Case 3 then the velocity is momentarily unphysical.

### Specific Value for the ice flow exponent, $n$

At this point we focus on a specific value for the ice flow exponent,  $n = 3$ , which is an empirically found standard value in ice sheet modelling [102]. Eqs. (5.18) to (5.20) can then be rewritten using Eq. (5.21):

$$\text{Case 1: } \alpha > \frac{3}{7} \quad \Rightarrow \quad u \rightarrow 0 \text{ as } x \rightarrow b, \quad (5.22)$$

$$\text{Case 2: } \alpha = \frac{3}{7} \quad \Rightarrow \quad u \text{ remains finite as } x \rightarrow b, \quad (5.23)$$

$$\text{Case 3: } \alpha < \frac{3}{7} \quad \Rightarrow \quad u \rightarrow \infty \text{ as } x \rightarrow b \text{ (momentarily)}. \quad (5.24)$$

We may demonstrate the impact of Eq. (5.21) with  $n = 3$  by using an initial thickness profile with the simple function  $g(x) = (1 + x)^\alpha$  in Eq. (5.13) with the boundary  $b = 1$ ,

such that

$$h = (1 + x)^\alpha(1 - x)^\alpha. \quad (5.25)$$

By varying the value of  $\alpha$  we see the diffusive velocity at the boundary  $u_b$  is discontinuous at the moment  $\alpha$  reaches  $3/7$  from above (Figure 5.2(a)), jumping from zero to a finite value. In Figure 5.2(b) we see  $u$  in the vicinity of the boundary for varying values of  $\alpha$ . As we approach the critical value from above the discontinuity forms until  $\alpha$  reaches  $3/7$  itself, at which point a non-zero finite velocity exists and the boundary begins to move as a result of diffusion.

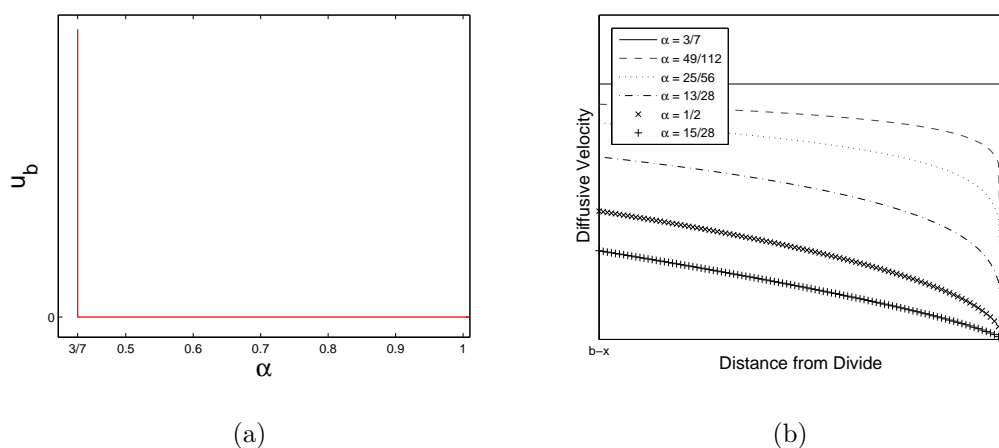
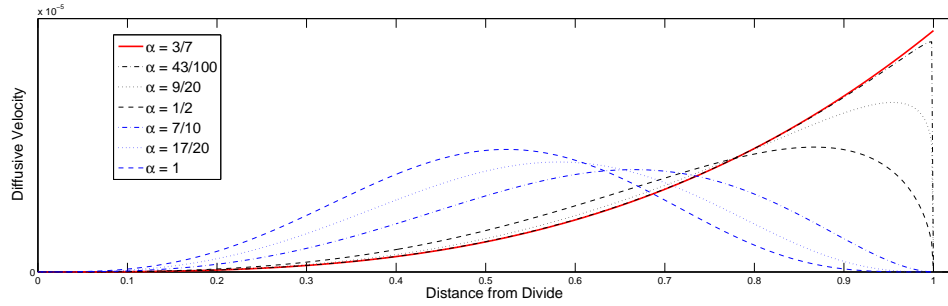
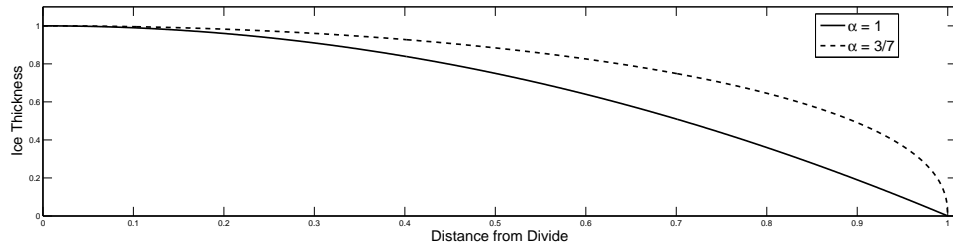


**Figure 5.2:** Varying the parameter  $\alpha$  in Eq. (5.13) with  $g(x) = (1 + x)^\alpha$  leads to a critical value when considering the diffusive velocity at the glacier front. a) As  $\alpha \rightarrow 3/7$  from above the boundary diffusive velocity  $u_b$  jumps to a finite value. b) Velocity in the vicinity of the boundary for varying values of  $\alpha$ . As  $\alpha \rightarrow 3/7$  the velocity profile steepens, maintaining a zero velocity on the boundary until  $\alpha$  reaches  $3/7$ , at which point it jumps to a finite value

Continuing with this specific example, we consider the diffusive velocity over the whole domain (Figure 5.3(a)) where we see that not only does the value of  $\alpha$  affect the velocity of the boundary, but the velocity profile as a whole. We see the peak value for the diffusive velocity moves from close to the centre of the domain when  $\alpha = 1$ , to the boundary as  $\alpha$  approaches  $3/7$ . When it reaches this value the peak velocity is located at the boundary itself. In Figure 5.3(b) we see that when  $\alpha$  reaches the critical value



(a)



(b)

**Figure 5.3:** (a) Diffusive velocity. As  $\alpha \rightarrow 3/7$ , the peak velocity approaches the boundary, and when  $\alpha = 3/7$  (red line) the boundary velocity is finite whereas all other values have a zero boundary velocity. (b) Ice thickness profiles for  $\alpha = 1$  (solid) and  $\alpha = 3/7$  (dashed). Notice the infinite gradient at the boundary when  $\alpha = 3/7$

the gradient of the ice at the boundary  $b = 1$  is unbounded, which we highlighted as a requirement to get a non-zero velocity in Eq. (5.11).

### Incorporating the glacier bed

The above analysis has been performed under the assumption that the bed of the glacier is flat. In reality this is rarely the case, so we may define the surface elevation as a summation of the bed and ice components

$$s = z + h, \quad (5.26)$$

where  $z = z(x)$  represents the topography under the glacier. Continuing with the

assumption that  $n = 3$  allows us to write the diffusive velocity from Eq. (5.10) as

$$u = ch^4[(z + h)_x]^3 \quad (5.27)$$

$$= ch^4[z_x + h_x]^3 \quad (5.28)$$

$$= cz_x^3 h^4 + 3cz_x^2 h^4 h_x + 3cz_x h^4 h_x^2 + ch^4 h_x^3. \quad (5.29)$$

Note that the last term in Eq. (5.29) is the same as the single term in the flat bed scenario, Eq. (5.11). Expressing the terms in Eq. (5.29) in the same form used in Eq. (5.12) we get

$$u = cz_x^3 h^4 + \frac{3c}{5} z_x^2 (h^5)_x + \frac{c}{3} z_x \{(h^3)_x\}^2 + \frac{9c}{343} \{(h^{7/3})_x\}^3. \quad (5.30)$$

The inclusion of a bed does not change the structure of the ice thickness, so again we may substitute in the expression for  $h$  given in Eq. (5.13)

$$u = cz_x^3 (b - x)^{4\alpha} g(x)^4 + \frac{3c}{5} z_x^2 ((b - x)^{5\alpha} g(x)^5)_x + \frac{c}{3} z_x \{((b - x)^{3\alpha} g(x)^3)_x\}^2 + \frac{9c}{343} \{((b - x)^{7\alpha/3} g(x)^{7/3})_x\}^3. \quad (5.31)$$

The diffusive velocity at the moving boundary is found by taking the limit of  $u$  as  $x \rightarrow b$ ,

$$\lim_{x \rightarrow b} u = \lim_{x \rightarrow b} \left[ cz_x^3 (b - x)^{4\alpha} g(x)^4 + \frac{3c}{5} z_x^2 ((b - x)^{5\alpha} g(x)^5)_x + \frac{c}{3} z_x \{((b - x)^{3\alpha} g(x)^3)_x\}^2 + \frac{9c}{343} \{((b - x)^{7\alpha/3} g(x)^{7/3})_x\}^3 \right]. \quad (5.32)$$

The first term tends to zero at the boundary and again we apply L'Hopital's rule to the remaining three terms individually to leave

$$u(b) = -\frac{3c}{5} z_b^2 \lim_{x \rightarrow b} [(b - x)^{5\alpha-1} g(x)^5] + \frac{c}{3} z_b [-\lim_{x \rightarrow b} \{(b - x)^{3\alpha-1} g(x)^3\}]^2 + \frac{9c}{343} [-\lim_{x \rightarrow b} \{(b - x)^{7\alpha/3-1} g(x)^{7/3}\}]^3. \quad (5.33)$$

The analysis of the non-flat bed scenario leads to the same critical value of  $\alpha$  defined in Eq. (5.21), as the following argument shows. Using the same technique here, but treating these terms separately leads to a situation where each term provides a different

critical value of  $\alpha$  to the one found previously. The first term yields the value of  $1/5$ , the second  $1/3$  and since the last term is the same as the flat bed, its critical value is  $3/7$  as before.

Since  $\alpha$  cannot go below any of these values without encountering an infinite velocity (see Eq. (5.20)), the lower limit for  $\alpha$  must be the largest value, namely  $3/7$ . Therefore the flat bed analysis holds and the same condition for a diffusive velocity on the boundary exists regardless of whether there is a topographic bed present.

In addition, while we made the assumption in Eq. (5.10) that the temperature and density were constant, the analysis above is in fact independent of these parameters since the analysis applies to a factor of  $h$ . In other words, if temperature and density varied spatially they could be included within  $g(x)$  which does not impact the condition upon  $\alpha$ . Differing these values will provide a different value for the finite velocity achieved when Case 2 is met; however, the boundary velocity will remain zero while in Case 1 regardless of the temperature or density.

We now have a condition upon the ice thickness profile which allows the diffusive flow of the boundary to be non-zero. In the absence of any accumulation/ablation this is the sole cause for movement of the ice and it would be possible to determine when the glacier remains stationary and when movement will begin.

## 5.2.2 Steady-state solution

It is possible for glaciers to enter an equilibrium state where the net mass of ice remains constant over a period of time. We now introduce a solution to this equilibrium state, known as a steady state solution, which will be used to test the accuracy of our numerical model later in the chapter.

One approach to finding this steady state solution is to rewrite the problem as an energy functional and minimise, see [56], though here we will directly find a solution by integration. Glaciers enter steady state when the amount of ice accumulated is balanced by the amount lost through ablation. Mathematically we require the change

in ice thickness to be zero,  $h_t = 0$ , which reduces Eq. (5.2) to

$$(h(x)u(x))_x = m(x), \quad (5.34)$$

where we assume the ice equivalent accumulation rate  $m$  to be independent of time in order to maintain equilibrium. By integration we may write Eq. (5.34) as

$$hu = \int_0^x m(y)dy \quad (5.35)$$

where  $y$  is a dummy variable. Substituting the flat bed diffusive velocity  $u$  from Eq. (5.11) gives

$$ch^{n+2}h_x^n = \int_0^x m(y)dy, \quad (5.36)$$

which we may write in an alternate form similar to Eq. (5.12)

$$c \left( \frac{n}{2n+2} \right)^n \{ (h^{(2n+2)/n})_x \}^n = \int_0^x m(y)dy. \quad (5.37)$$

Next we move all the constants over to the right hand side before raising both sides to the power of  $1/n$ ,

$$(h^{(2n+2)/n})_x = \left( \frac{2n+2}{nc^{1/n}} \right) \left( \int_0^x m(y)dy \right)^{1/n}. \quad (5.38)$$

Integrating a second time gives

$$h^{(2n+2)/n} = \left( \frac{2n+2}{nc^{1/n}} \right) \int_b^x \left( \int_0^y m(z)dz \right)^{1/n} dy \quad (5.39)$$

where  $z$  is a second dummy variable of integration. Finally raising both sides to the power of  $n/(2n+2)$  gives the ice thickness at any point  $x$  in steady state

$$h(x) = \left( \frac{2n+2}{nc^{1/n}} \right)^{n/(2n+2)} \left[ \int_b^x \left( \int_0^y m(z)dz \right)^{1/n} dy \right]^{n/(2n+2)}. \quad (5.40)$$

In order to reconstruct the ice thickness profile using Eq. (5.40), we require the location of the moving boundary  $b$ , which in steady state will be stationary. To find this value we require the net accumulation and ablation across the whole domain to be zero, so that although the glacier ice is still flowing the overall movement is zero. Therefore in steady state:

$$\int_0^b mdx = 0 \quad (5.41)$$

With Eqs. (5.40) and (5.41), if we know the ice equivalent accumulation rate across the entire domain or we choose a function to represent it that is time independent, we can find the location of the boundary and thus construct the corresponding steady state profile. We make use of this profile to test the results of our moving mesh scheme in Section 5.5.1.

## 5.3 Glacier Movement

We now turn our attention to constructing a method that describes the overall movement of the glacier. This net velocity incorporates the ice diffusive velocity and accumulation/ablation effects. The method for finding this velocity is based upon the BHJ method discussed in Section 3.3.

### 5.3.1 Conserving Mass Fractions (CMF)

For a time-dependent PDE with a source term, the relative mass of a local subdomain is conserved by enforcing the conservation principle (Eq. (3.3)) over time. For glaciers with ice thickness  $h$  this may be written mathematically as

$$\frac{\int_0^{\hat{x}(t)} h dx}{\int_0^{b(t)} h dx} = \frac{1}{\theta(t)} \int_0^{\hat{x}(t)} h dx = \mu(\hat{x}), \quad (5.42)$$

applied to any moving subdomain  $(0, \hat{x}(t))$  of  $[0, b(t)]$ , with  $0 \leq \hat{x} \leq b$ . The variable  $\theta$  in Eq. (5.42) represents the total mass defined in Eq. (5.5). We remark that when described in this manner the constant-in-time function  $\mu(\hat{x}) \in [0, 1]$  forms a cumulative function with  $\mu(0) = 0$  and  $\mu(b) = 1$ . This method is referred to as the Conservation of Mass Fractions (CMF) approach throughout this thesis.

To extract a velocity we begin by differentiating Eq. (5.42) with respect to time to

leave

$$\frac{d}{dt} \int_0^{\hat{x}(t)} h dx = \mu \frac{d\theta}{dt} \quad (5.43)$$

$$= \mu \int_0^{b(t)} m dx, \quad (5.44)$$

where we refer back to the differential property of total mass Eq. (5.9). Carrying out the time differentiation on the left hand side of Eq. (5.44) using Leibnitz' Integral Rule gives

$$\frac{d}{dt} \int_0^{\hat{x}(t)} h dx = \int_0^{\hat{x}(t)} h_t dx + \left( h \frac{d\hat{x}}{dt} \right) \Big|_0^{\hat{x}(t)}. \quad (5.45)$$

Applying the boundary condition in Eq. (5.3) forces the velocity  $d\hat{x}/dt$  to be zero at the ice divide  $x = 0$ . Substituting for  $h_t$  from the shallow ice PDE Eq. (5.2) leaves

$$\begin{aligned} \frac{d}{dt} \int_0^{\hat{x}(t)} h dx &= \int_0^{\hat{x}(t)} (-(hu)_x + m) dx + \left( h \frac{d\hat{x}}{dt} \right) \Big|_{\hat{x}(t)} \\ &= \int_0^{\hat{x}(t)} m dx + \left( h \frac{d\hat{x}}{dt} - hu \right) \Big|_{\hat{x}(t)}, \end{aligned} \quad (5.46)$$

where again the boundary condition in Eq. (5.3) requires the flow velocity  $u$  to be zero at the fixed boundary  $x = 0$ . Combining Eq. (5.44) and Eq. (5.46) we obtain the net velocity of an arbitrary interior point  $\hat{x}(t)$  to be

$$\frac{d\hat{x}}{dt} = u + \frac{\left[ \mu \int_0^{b(t)} m dx - \int_0^{\hat{x}(t)} m dx \right]}{h}. \quad (5.47)$$

This velocity describes the net overall movement of a point in the glacial domain as a combination of the flow velocity  $u$  and the accumulation rate  $m$ . Using this we may determine the changes in the domain over time.

### 5.3.2 Net Velocity at the Glacier Front

The velocity given by Eq. (5.47) describes the movement of any interior point. Assuming continuity of the velocity the corresponding net velocity at the moving front at  $x = b$  may be indentified by taking the limit of Eq. (5.47) as  $\hat{x}(t) \rightarrow b$ ;

$$\lim_{\hat{x}(t) \rightarrow b} \frac{d\hat{x}}{dt} = u|_b + \lim_{\hat{x}(t) \rightarrow b} \frac{1}{h} \left[ \mu \int_0^{b(t)} m dx - \int_0^{\hat{x}(t)} m dx \right]. \quad (5.48)$$

The limit is undefined since  $h \rightarrow 0$  as  $\hat{x} \rightarrow b$ ; however, since the quantity in square brackets also  $\rightarrow 0$  as  $\hat{x}(t) \rightarrow b$ , then by l'Hopital's Rule (assuming continuity of  $\frac{dx}{dt}$  and  $m$  in the vicinity of the boundary);

$$\lim_{\hat{x}(t) \rightarrow b} \frac{d\hat{x}}{dt} = u|_b + \lim_{\hat{x}(t) \rightarrow b} \left\{ \frac{\frac{d}{d\hat{x}(t)} \left[ \mu \int_0^{b(t)} m dx - \int_0^{\hat{x}(t)} m dx \right]}{h_x} \right\} \quad (5.49)$$

$$= u|_b + \lim_{\hat{x}(t) \rightarrow b} \left\{ \frac{\frac{\theta'}{\theta} h - m}{h_x} \right\} \quad (5.50)$$

$$= \left( u - \frac{m}{h_x} \right) \Big|_{x=b} \quad (5.51)$$

This is the velocity at the boundary, which incorporates the accumulation  $m$  (normalised by the local gradient  $h_x$ ) as well as the diffusive velocity  $u$ . Since  $h_x < 0$  at the front  $x = b$ , the second term in Eq. (5.51) is positive or negative depending on whether  $m$  is positive or negative.

If the gradient  $h_x$  at the front is shallow, the net boundary velocity is mainly influenced by the accumulation/ablation component and allows the front to advance or retreat. Conversely, for steep gradients the accumulation term becomes less important and the flow velocity  $u$  dominates. This means that the front is susceptible to the analysis of the diffusive velocity in Section 5.2.1: in this case the overall movement of the glacier front can then only advance or stay, not retreat.

### 5.3.3 Radial Adjustment

Some glaciological features, such as an Ice Dome (a mass of ice with a rounded, gently sloping dome [2]) can crudely be represented using a one dimensional radial model. It is also beneficial to create idealistic radially symmetric configurations to obtain steady state solutions for higher dimensional models [92]. For a radially symmetric icesheet the shallow-ice PDE (Eq. (5.2)) can be adjusted to give

$$\frac{\partial h}{\partial t} + \frac{1}{r} \frac{\partial(rhu)}{\partial r} = m \quad (5.52)$$

where the diffusive velocity (Eq. (5.11)) becomes

$$u = -\frac{2Ah}{n+2}\rho^n g^n h^n \left(\frac{\partial h}{\partial r}\right)^n. \quad (5.53)$$

In addition the total mass defined in Eq. (5.5) is now calculated using

$$\phi = \int_0^{b(t)} h r dr, \quad (5.54)$$

whose rate of change is

$$\dot{\phi} = \frac{d}{dt} \int_0^{b(t)} h r dr = \int_0^{b(t)} m r dr. \quad (5.55)$$

The CMF approach of Eq. (5.42) is based upon the assumption that relative mass is conserved. In a radially symmetric environment this implies that

$$\frac{1}{\phi} \int_0^{\hat{r}(t)} r h dr = \nu(\hat{r}), \quad (5.56)$$

where the constants  $\nu$  are independent of time and represent the radial equivalent of the constants  $\mu$  (Eq. (5.42)). These are defined on any moving subdomain  $(0, \hat{r}(t))$  of  $[0, b(t)]$  leading, in a similar way as in Section 5.3.1, to a similar expression for net velocity

$$\frac{d\hat{r}}{dt} = u + \frac{\left[ \nu \int_0^{b(t)} m r dr - \int_0^{\hat{r}(t)} m r dr \right]}{h} \quad (5.57)$$

With this small adjustment we are able to simulate a radially symmetric domain using a one-dimensional approach.

## 5.4 Numerical Approximation

With the method for extracting the net movement of a glacier outlined in Section 5.3 we now define the techniques to numerically approximate this approach in the form of a moving mesh method. We begin by detailing the numerical flowline model before examining the numerical approximation to the velocity at the glacier front and finally the numerical radial model.

### 5.4.1 A Finite Difference Scheme

We now describe a finite difference numerical scheme based on the CMF approach in Section 5.3. Denoting the mesh nodes by  $\{X_i\}$  for  $(i = 1, 2, \dots, N)$ , the initial domain may be discretised such that

$$0 = X_1(t) < X_2(t) < \dots < X_N(t) = b(t). \quad (5.58)$$

We define  $H_i$ ,  $U_i$  and  $\mu_i$  as the discrete approximations of  $h(X_i)$ ,  $u(X_i)$  and  $\mu(X_i)$  respectively. To initialise the moving mesh scheme the domain  $\{X_i\}$  and the ice thickness  $\{H_i\}$  is required. The numerical scheme forms an algorithm that can be split into three stages;

#### Stage 1

The first stage of the algorithm approximates the mesh velocity from Eq. (5.47) using finite differences to give a discrete velocity at each interior node in the form

$$\frac{dX_i}{dt} = U_i - \frac{\left\{ \mu_i \int_0^{b(t)} m dx - \int_0^{X_i(t)} m dx \right\}}{H_i} \quad (5.59)$$

$$= -c \left( \frac{n}{2n+1} \right)^n \left( \frac{H_i^{(2n+1)/n} - H_{i-1}^{(2n+1)/n}}{X_i - X_{i-1}} \right)^n - \frac{\left\{ \mu_i \int_0^{b(t)} m dx - \int_0^{X_i(t)} m dx \right\}}{H_i}, \quad (5.60)$$

where the derivative of  $h^{(2n+1)/n}$  in  $u$  is approximated using an upwind difference and the integrals are approximated by the composite trapezium rule (see Section B.3).

#### Stage 2

In the second stage we advance each of the nodes  $X_i$  forward in time using an explicit Euler scheme,

$$X_i^{k+1} = X_i^k + \Delta t \left( \frac{dX_i}{dt} \right)^k. \quad (5.61)$$

for all  $i$ . Here  $k$  denotes the time discretisation level. The same approach is applied to the total mass  $\theta^{k+1}$ . Using Eq. (5.9), the explicit Euler equation for updating the total

mass is given by

$$\theta^{k+1} = \theta^k + \Delta t \int_0^{b^{k+1}} m dx. \quad (5.62)$$

where again we approximate the integral using the trapezium rule.

Explicit Euler time-stepping is sufficient for our purpose provided that the time step is sufficiently small to ensure stability and prevent the nodes from crossing each other's path. While there is no formal definition for a moving mesh time-step, we may use as a guideline the general rule for diffusion equations:

$$\Delta t \leq \frac{(\Delta x)^2}{2D}, \quad (5.63)$$

where  $D = ch^{n+2}|s_x|^{n-1}$  is the diffusivity of the PDE.

### Stage 3

After finding the new locations for each of the nodes, the final stage of the algorithm recovers values for the ice thickness  $H_i$  at each of the nodes using a discretised form of the conservation principle (Eq. (5.42)). Since the integral in Eq. (5.42) is constant in time for all  $\hat{x}(t)$ , we may approximate this equation in the form

$$\frac{1}{\theta^{k+1}} \left[ \int_{X_{i-1}}^{X_{i+1}} h dx \right]^{k+1} = \mu_{i+1} - \mu_{i-1} \quad (5.64)$$

where the limits in the integral arise from an incremental form of Eq. (5.42). Approximating Eq. (5.64) by a midpoint rule, we obtain

$$H_i^{k+1} = \frac{\theta^{k+1}(\mu_{i+1} - \mu_{i-1})}{(X_{i+1}^{k+1} - X_{i-1}^{k+1})}, \quad (5.65)$$

which provides the ice thickness at the next time step. Eq. (5.65) forces the relative mass to be conserved in time, thus maintaining the initial principle of the method.

## 5.4.2 Numerical Diffusive Velocity at the Glacier Front

We now relate the numerical approximation to the diffusive velocity at the front to the analysis in Section 5.2.1. Recall that the upwind approximation  $U_i$  to the diffusive

velocity  $u(X_i)$  in Eq. (5.60) is

$$U_i = -c \left( \frac{n}{2n+1} \right)^n \left( \frac{H_i^{(2n+1)/n} - H_{i-1}^{(2n+1)/n}}{X_i - X_{i-1}} \right)^n \quad (5.66)$$

Hence the approximation to the diffusive velocity at the glacier front  $U_N$  is given by

$$U_N = c \left( \frac{n}{2n+1} \right)^n \frac{(H_{N-1})^{2n+1}}{(X_N - X_{N-1})^n}, \quad (5.67)$$

since  $H_N = 0$ . At first glance this bears little resemblance to the analytic diffusive velocity at the boundary Eq. (5.17), where

$$u(b) \propto (b-x)^{(2n+1)\alpha-n}. \quad (5.68)$$

But by rewriting this expression, using Eq. (5.13) we obtain

$$u(b) \propto \frac{(b-x)^{(2n+1)\alpha}}{(b-x)^n} \quad (5.69)$$

$$\approx \frac{h^{(2n+1)}}{(b-x)^n}, \quad (5.70)$$

since  $h \propto (b-x)^\alpha$ . Eq. (5.70) has a very similar form to Eq. (5.67). Asymptotically when  $X_{N-1}$  is close to  $X_N (= b)$  and  $\alpha > n/(2n+1)$ , the expressions in Eqs. (5.67) and (5.70) are small, but this is not the case if  $\alpha = n/(2n+1)$  as demonstrated in Section 5.2.1.

Therefore the closer together the nodes are at the glacier front, the more effective Eq. (5.67) is at providing a good approximation to Eq. (5.70). We may then say that the numerical scheme closely reflects the analytic behaviour of the diffusive velocity.

### 5.4.3 Radial Adjustment - Numerics

The numerical approximation to the radial adjustment made in Section 5.3.3 is very similar to the non-radial scenario in Section 5.4.1. The radial domain is discretised into a mesh  $\{R_i\}$ , where  $(i = 1, 2, \dots, N)$  and

$$0 = R_1(t) < R_2(t) < \dots < R_N(t) = b(t). \quad (5.71)$$

We define  $H_i$  and  $\nu_i$  to represent  $h(R_i)$  and  $\nu(R_i)$  respectively. Again the algorithm can be split into three stages;

### Stage 1

Stage 1 of the algorithm approximates the velocity Eq. (5.57) by finite differences to give

$$\frac{dR_i}{dt} = -c \left( \frac{n}{2n+1} \right)^n \left( \frac{H_i^{(2n+1)/n} - H_{i-1}^{(2n+1)/n}}{R_i - R_{i-1}} \right)^n - \frac{\left\{ \nu_i \int_0^{b(t)} m r dr - \int_0^{R_i(t)} m r dr \right\}}{H_i} \quad (5.72)$$

at each node  $R_i$ .

### Stage 2

The second stage advances the mesh nodes  $R_i(t)$  with this velocity by the explicit Euler scheme

$$R_i^{k+1} = R_i^k + \Delta t \left( \frac{dR_i}{dt} \right)^k \quad (5.73)$$

for all  $i$ . The total mass  $\phi$  is also updated using an explicit Euler equation on Eq. (5.55) to give

$$\phi^{k+1} = \phi^k + \Delta t \int_0^{b^{k+1}} m r dr. \quad (5.74)$$

where we approximate the integral using the composite trapezium rule.

### Stage 3

Finally the discrete ice thickness  $H_i$  is recovered algebraically from the incremental form of Eq. (5.56)

$$\frac{1}{\phi^{k+1}} \left[ \int_{\hat{R}_{i-1}(t)}^{\hat{R}_{i+1}(t)} r h dr \right]^{k+1} = \nu_{i+1} - \nu_{i-1}, \quad (5.75)$$

using a midpoint discretisation:

$$H_i^{k+1} = \frac{\phi^{k+1}(\nu_{i+1} - \nu_{i-1})}{(R_{i+1}^{k+1})^2 - (R_{i-1}^{k+1})^2} \quad (5.76)$$

As with the non-radial approximation the relative mass is conserved in time and the algorithm is repeated at each time step.

## 5.5 Experiments

We now examine two scenarios to evaluate the moving mesh method. The first is a simple test scenario designed to demonstrate the method covering the core aspects of glacier flow, while the second is a radially symmetric scenario designed to test and compare the efficiency of numerical ice sheet models.

### 5.5.1 Testing the Model

For an initial test we shall examine the ice thickness profile encountered during the diffusive velocity analysis (Section 5.2.1). The initial profile is of the form

$$h = (b^2 - x^2)^\alpha \quad (5.77)$$

on an initial domain  $x \in [0, b]$  where  $x = 0$  is fixed and the initial moving front  $x_b = 1$ .

For the source term  $m$  we use the quadratic function

$$m = \gamma \left(1 - \frac{x^2}{\beta}\right), \quad (5.78)$$

where  $\beta$  defines where the source term changes from accumulation to ablation (called the equilibrium line) and  $\gamma$  is a parameter to control the scale of the source term. This function is independent of time and as such there exists a steady state solution as detailed in Section 5.2.2. Using Eq. (5.41) it can be shown that in steady state the boundary,  $b_{ss}$ , will be located at

$$b_{ss} = \sqrt{3\beta}. \quad (5.79)$$

Using the parameters defined in Table 5.1 we may test the numerical model and its behaviour.

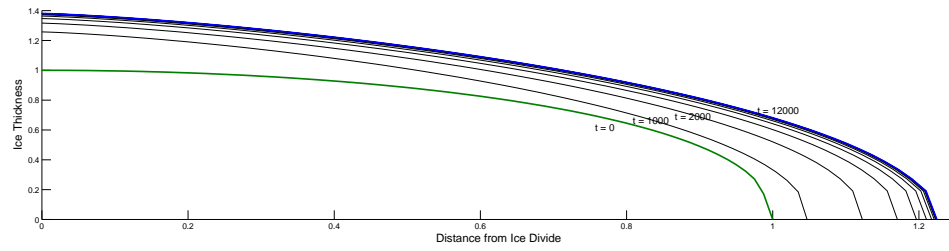
Physical Parameters	
$n = 3$	Flow-law exponent
$A = 10^{-16}(Pa)^{-3}a^{-1}$	Flow-law parameter
$g = 9.81ms^{-2}$	Acceleration of gravity
$\rho = 910kgm^{-3}$	Ice density
$c = -2Ag^n\rho^n/(n + 2)$	Constant Parameter
$\gamma = 0.0005$	Scale of accumulation rate
Computational Data	
$N = 26$	Number of gridpoints
$\Delta x^0 = 0.02$	Initial grid spacing
$\Delta t = 0.05$	Time Step
$T$	Final Time

**Table 5.1:** Values of the physical parameters in the test model and the computational data used in the test equations.

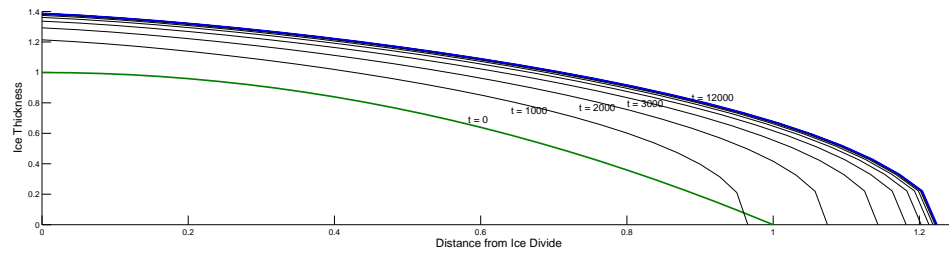
**Glacier in Advance:**  $\alpha = 3/7$ ,  $\beta = \frac{1}{2}$ ,  $T = 12000a$

By choosing the equilibrium line  $\beta = 1/2$  such that the boundary of the steady state solution is greater than the initial boundary we can demonstrate an advancing glacier. We set  $\alpha = 3/7$  to satisfy the condition on the diffusive velocity for initial movement in Eq. (5.21). We observe in Figure 5.4(a) an overall increase in the amount of ice in the domain, along with movement of the front towards the steady state boundary  $b_{ss} = \sqrt{1.5}$  defined in Eq. (5.79). Since there is an initial diffusive velocity the movement of the numerical nodes of the mesh are all in the same direction (see Figure 5.5(a)).

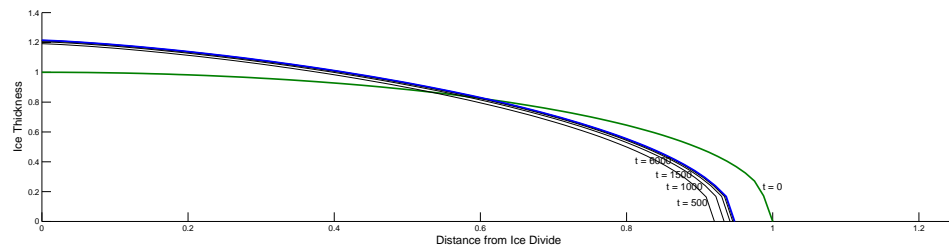
Conversely if we set  $\alpha = 1$  so that the diffusive velocity on the boundary is initially zero, we observe that the boundary actually begins to retreat due to ablation from the source term Eq. (5.78). However as the ice thickness profile changes over time to satisfy the condition on the diffusive velocity at the boundary, the glacier begins to advance to reach its steady state profile (see Figures 5.4(b) and 5.5(b)).



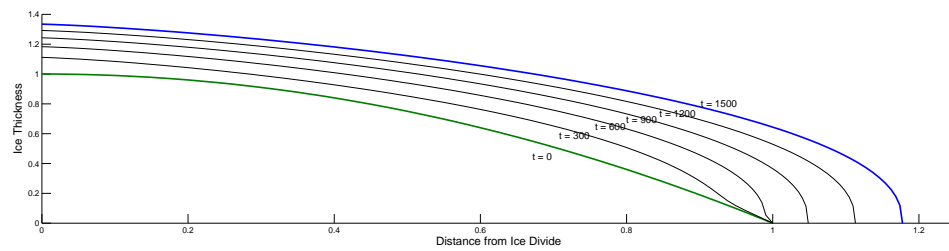
(a) Advancing Glacier;  $\alpha = 3/7, \beta = \frac{1}{2}$



(b) Advancing Glacier;  $\alpha = 1, \beta = \frac{1}{2}$



(c) Retreating Glacier;  $\alpha = 3/7, \beta = \frac{3}{10}$



(d) Initially Stationary Glacier;  $\alpha = 1, \beta = 1$

**Figure 5.4:** 1D test equations: Ice thickness over the domain evolving from the initial profile (green) to a final steady state profile (blue).

**Glacier in Retreat:**  $\alpha = 3/7, \beta = \frac{3}{10}, T = 6000a$

Let us now choose the equilibrium line to be located close to the ice divide ( $x = 0$ ), for example,  $\beta = 3/10$ . Under this condition the location of the steady state boundary

(Eq. (5.79)) is to the left of the initial boundary. We therefore expect the front of the glacier to retreat and the ice thickness to decrease.

In Figure 5.4(c) we see a rapid initial retreat, where the boundary moves further back than the steady state location. The glacier then appears to stabilise and advances back up to the steady state location. This is shown in the nodal characteristics plot (Figure 5.5(c)) where we observe the initial retreat followed by a slow advance back to the steady state boundary. Crucially we see the interior points also retreat in line with the boundary which means the nodes avoid crossing each others paths, an important stability property for any moving mesh method.

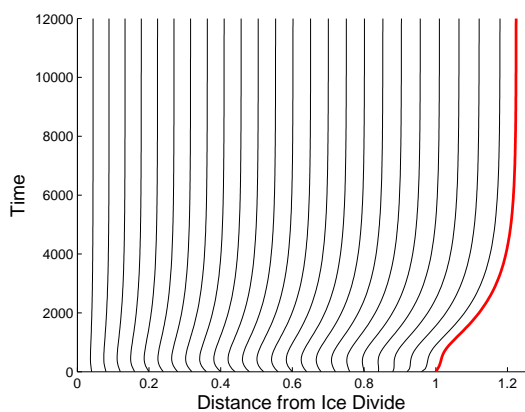
**Stationary Front:**  $\alpha = 1, \beta = 1, T = 1500a$

Selecting  $\beta = 1$  in Eq. (5.78) yields zero accumulation/ablation at the initial boundary  $b = 1$ . Under this condition the diffusive velocity becomes the sole contribution to the velocity at the boundary, Eq. (5.51). Therefore the boundary responds to the analysis in Section 5.2.1 and by setting  $\alpha = 1$  we ensure the boundary is initially stationary.

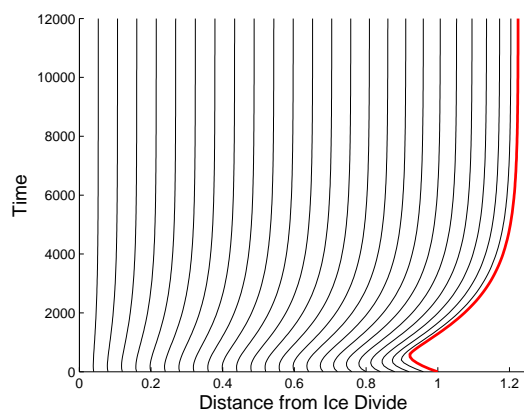
It is clearly visible in Figure 5.4(d) that the profile evolves towards an infinite gradient at the front to satisfy the finite diffusive velocity criteria in Eq. (5.19). Once this criteria is met the front begins to advance. Examining the movement of the mesh nodes in Figure 5.5(d) we can see that the interior nodes move towards the boundary as the interior ice is flowing, until this boundary profile is satisfied and the boundary itself begins to move.

**Summary**

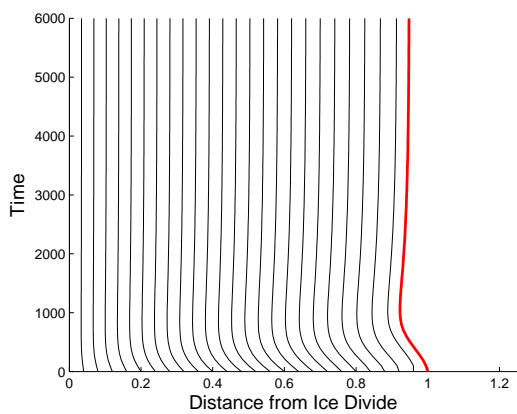
We have shown that the numerical approximation described in Section 5.4.1 can competently model a glacier that is advancing, retreating or remaining stationary. The method itself is computationally cheap, each scenario running in under a minute for the experimental data given. We now turn our attention to a practical example for comparison with existing glacier models.



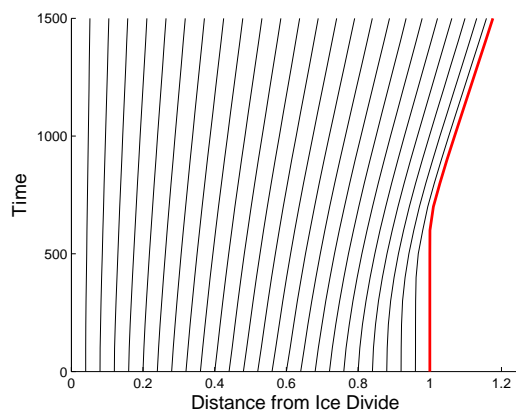
(a) Adv. Glacier;  $\alpha = 3/7, \beta = \frac{1}{2}, T = 12000a$



(b) Adv. Glacier;  $\alpha = 1, \beta = \frac{1}{2}, T = 12000a$



(c) Retreating Glacier;  $\alpha = 3/7, \beta = \frac{3}{10}, T = 6000a$



(d) Initially Stationary Glacier;  $\alpha = 1, \beta = 1, T = 1500a$

**Figure 5.5:** Evolution of the mesh nodes over time, including the boundary point (red) representing the glacier front.

### 5.5.2 European Ice Sheet Modelling INiTiative

The European Ice Sheet Modelling INiTiative (EISMINT) experiments [49] give a set of standard benchmark scenarios to test and compare numerical models of ice sheet behaviour. The initial paper [49] contains information about two scenarios; the first is a fixed margin experiment on a square domain which deals with calculating the ice discharge at the boundary and the second is a radially symmetric situation with a moving boundary. We shall replicate the second experiment using the radially adjusted CMF method detailed in Section 5.3.3.

The experiment begins with a flat bed with zero ice present. The CMF method is dependent on preserving relative mass, for which we need an initial mass to calculate. To achieve this we take the ice thickness profile after one time-step, which corresponds to the source term only as there is no ice to diffuse. This term is given by

$$m = \min\{0.5, \gamma(\beta - x)\}, \quad (5.80)$$

and so the initial profile of ice thickness is

$$h^0 = \Delta t \times \min\{0.5, \gamma(\beta - x)\} \quad (5.81)$$

with  $x \in [0, 4.5 \times 10^5]$ . In Eq. (5.81) the equilibrium line is located at  $\beta = 4.5 \times 10^5 m$  and the scale of the source term is given by  $\gamma = 10^{-5} a^{-1}$ . Again the source term is independent of time, so there exists a steady state solution. Using a radially adjusted version of Eq. (5.41)

$$\int_0^{b(t)} m r dr = 0 \quad (5.82)$$

we may calculate the steady state boundary location to be

$$b_{ss} = 579.81 km, \quad (5.83)$$

and the steady state ice thickness may be reconstructed using the method in Section 5.2.2.

Physical Parameters	
$n = 3$	Flow-law exponent
$A = 10^{-16}(Pa)^{-3}a^{-1}$	Flow-law parameter
$g = 9.81ms^{-2}$	Acceleration of gravity
$\rho = 910kgm^{-3}$	Ice density
$m = \min\{0.5, \gamma(\beta - x)\}$	Ice equivalent accumulation/ablation (source)
$\gamma = 10^{-2}ma^{-1}km^{-1}$	Slope of source function
$\beta = 450km$	Equilibrium line location
Computational Data	
$N = 16$	Number of gridpoints
$\Delta r^0 = 3 \times 10^4m$	Initial grid spacing
$\Delta t = 2a$	Time Step
$T = 3 \times 10^5a$	Final Time

**Table 5.2:** Values of the physical parameters in the model and the computational data used in the EISMINT scenario.

The physical parameters for the model are provided in Table 5.2 along with the numerical data. For direct comparison with the fixed grid methods grid methods presented in [49], performed on a  $31 \times 31$  regular rectangular grid, the 1D moving mesh model uses 16 grid points, initially spaced evenly. This allows for a time step of  $2a$ , up to a final time of  $30,000a$ . Note that the unit  $a$  refers to one *annum*, equivalent to one year. Computationally this solution takes less than five seconds to run on a standard desktop.

As the problem is radially symmetric, the results of the one-dimensional flowline method may be presented as a circle which allows for comparison with two-dimensional methods.

The numerical solutions to the experiment in [49] are found using traditional fixed grid methods on evenly spaced grids. This means that they require some form of extrapolation or interpolation to find the boundary location as the boundary generally falls between two grid points in a 1D flowline model or four with a 2D grid. As a

result fixed grid methods on a regular two-dimensional rectangular grid, such as those presented, do not return a perfect circle due to the location of the grid points, as shown in Figure 5.6(a). This is not an issue with the flowline models such as the one used here, which when rotated naturally give a circle (see Figure 5.6(b)).

Instead a direct comparison between flowline models would provide more of an insight. When comparing, we see that the moving mesh method is able to get significantly closer to the exact ice thickness profile than the equivalent fixed grid method in Figure 5.6(c), especially close to the moving front. We also see from Figure 5.6(d) that the diffusive velocity in steady state is similar between the two approaches, with the main difference arising at the boundary, where the diffusive velocity can be explicitly calculated in the moving mesh approach. The fixed grid schemes require interpolation to calculate this value.

Expressing these results in Table 5.3 shows that the CMF moving mesh solution is able to get much closer to the exact boundary position than the average fixed grid solution, while the thickness at the ice divide (where  $r = 0$ ) is slightly higher than both the fixed grid and exact solutions. This is most likely due to an underestimation of the flow velocity in the accumulation regions of the domain, which is visible when compared to the fixed grid in Figure 5.6(d). A slower velocity transports less ice to the areas where mass is lost due to ablation resulting in an overestimation of the ice thickness in the accumulation regions, where the divide is located.

We have demonstrated that the moving mesh method provides a better approximation than traditional fixed grid methods to a flowline model using the same number of grid points. We have also tested the model using scenarios containing time-dependent source terms, such as the sinusoidally varying expression found in [49]. In these cases we found that the moving mesh method produces a good approximation and is able to deal effectively with a domain that is continuously advancing and retreating.

### Convergence

An important test of any numerical model is its ability to converge towards the exact solution as the number of mesh points is increased. For a source term  $m$  that is independent of time we can calculate the analytic steady state solution using Section 5.2.2

Experiment	Divide Thickness (m)	Boundary Position (km)
Avg EISMINT	2856.9	594.9
Moving Mesh	3005.3	576.9
Exact	2951.5	579.81

**Table 5.3:** Comparison between the average EISMINT experiment results, the moving mesh approach and the exact steady state solution.

$N$	Boundary position (km)	Divide thickness (m)
16	576.894	2995
31	579.104	2983
61	579.636	2981
Exact	579.814	2952

**Table 5.4:** Table of 1D values for boundary position and divide thickness with varying number of mesh nodes.

to provide exact values. We shall check convergence of the moving mesh scheme at the steady state using the EISMINT data (see Section 5.5.2), for an increasing number of mesh points.

Table 5.4 shows that both the position of the moving boundary,  $X_N$  and the ice thickness at the divide,  $H_1$  ( $= H(X_1)$ ) converge toward the exact solution as the number of mesh points increases.

Shown in Table 5.5 is the relative error of the boundary position and the relative error of the divide ice thickness with respect to the reference value. We see that the error decreases for increasing numbers of mesh points. Assuming that relative error for the boundary is  $\propto N^{-p}$  where  $p$  is the order of convergence, we find  $p \approx 2$ . The  $L_2$  norm of the relative ice thickness (discretely defined as  $H = (H_1, H_2, \dots, H_N)$ ) shows evidence of superlinear convergence.

$N$	$ X_b^{\text{exact}} - X_b / X_b^{\text{exact}} $	$\ H^{\text{exact}} - H\ _2/\ H^{\text{exact}}\ _2$
16	0.0050	0.0093
31	0.0012	0.0052
61	0.0003	0.0021

**Table 5.5:** *Error analysis for varying mesh nodes.*

We therefore find that the numerical CMF moving mesh method is convergent with second order accuracy.

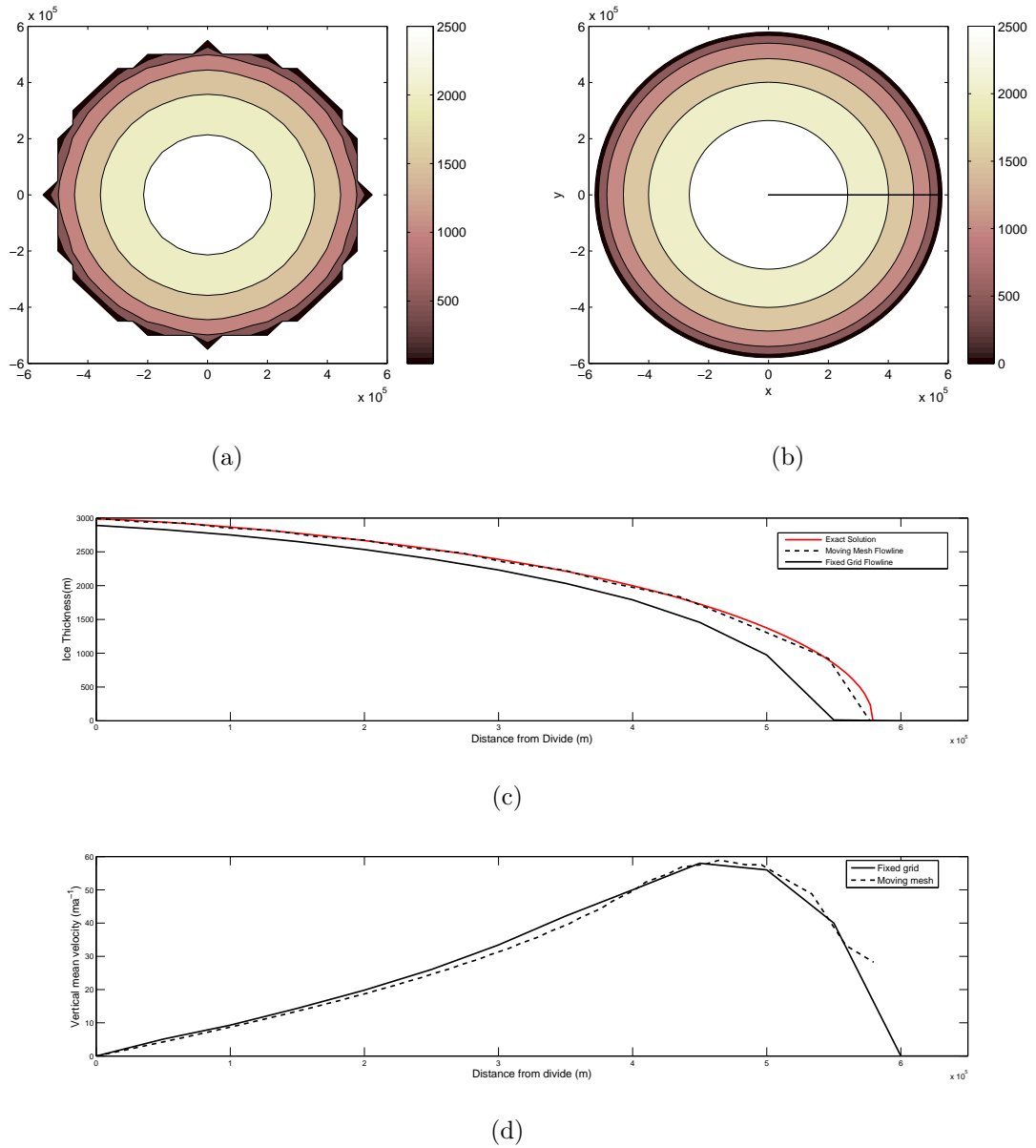


**Figure 5.6:** *Steady-state solutions to the EISMINT scenario: a) A 2D fixed grid method. b) 1D Moving mesh flowline radial model converted to 2D. c) Ice thickness profile along the flowline: exact (red), moving mesh (dash), fixed grid (solid). d) Diffusive velocity: moving mesh (dash), fixed grid (solid).*

## 5.6 Summary

In this chapter we began by looking at the shallow-ice glacier PDE and some of its features. In particular we looked at the diffusive component of velocity at the moving boundary. We developed a condition upon the profile of the ice thickness that determines if there exists a finite diffusive velocity at the boundary or if that element is stationary. This condition was shown to be independent of temperature, density and the presence of a topographical bed.

We then developed a procedure for modelling the flow using relative mass conservation to determine a velocity comprised of the diffusive velocity and accumulation/ablation. This method was then approximated numerically by a moving mesh solution using finite differences, along with a modified method for a radially symmetric solution.

The numerical model was then tested, firstly against a test function to demonstrate the model is able to achieve the advance, retreat and stationary movements that glaciers are capable of. Secondly we applied the model to the EISMINT moving mesh scenario, where the results compare favourably against both the fixed grid methods used previously and the exact solution.

# Chapter 6

## Data Assimilation on Moving Meshes in 1D

In this chapter we look at applying the concepts of data assimilation to combine observations with our moving mesh model to provide a best estimate of the real state of the ice sheet. We apply an optimised 3D-Var scheme to the model introduced in the previous chapter and show the impact on the components of the scheme when the mesh is moving. We test this scheme using a twin experiment applied to the test scenario in the previous chapter.

We then proceed to build an extended scheme that treats the numerical mesh as a set of unknown state variables in order to include observations of positional features. We demonstrate how these observations alter our numerical predictions and highlight some of the challenges that arise with this extension.

### 6.1 3D-VAR on a Moving Domain

The observational network across the Earth has improved dramatically in recent years, giving us the opportunity to apply data assimilation to models in the cryospheric field. Here we apply the 3D-VAR scheme to our shallow ice moving mesh model. When assimilating on a moving mesh it is clear that the numerical domain will contain errors

in its representation of the physical domain, which does not occur in a fixed grid model. We now detail the differences in the algorithm when assimilating on a moving mesh.

As described in Chapter 4 the optimal 3D-VAR analysis at time  $t_k$  is given by the equation:

$$\mathbf{z}_k^a = \mathbf{z}_k^f + \mathbf{K}_k(\mathbf{y}_k - \mathbf{C}_k\mathbf{z}_k^f), \quad (6.1)$$

subject to the dynamical model

$$\mathbf{z}_k^f = \mathcal{M}\mathbf{z}_{k-1}^a, \quad (6.2)$$

where  $\mathbf{z}_k \in \mathbb{R}^q$  is a vector containing the unknown state variables. The superscript  $a$  represents the ‘*analysis*’ or best estimate of the state of the system and the previous guess or *forecast* is denoted using the superscript  $f$ .

To obtain an analysis solution the forecast is corrected at each assimilation time by a weighted difference between the observations  $\mathbf{y}_k \in \mathbb{R}^p$  and the predicted observations  $\mathbf{C}_k\mathbf{z}_k^f$ , where  $\mathbf{C}_k$  is known as the observation operator. The matrix weight  $\mathbf{K}$  is optimally [65] chosen to be

$$\mathbf{K}_k = \mathbf{B}_k\mathbf{C}_k^T(\mathbf{C}_k\mathbf{B}_k\mathbf{C}_k^T + \mathbf{R}_k)^{-1}, \quad (6.3)$$

where  $\mathbf{B}_k \in \mathbb{R}^{q \times q}$  and  $\mathbf{R}_k \in \mathbb{R}^{p \times p}$  are the background and observation error covariance matrices respectively.

The 3D-Var method is preferred to the other methods introduced in Chapter 4 as it provides an optimal explicit equation for the analysis solution. In addition the choice of the background error covariance matrix in the moving mesh environment can reduce the impact of some of the deficiencies of the 3D-VAR scheme (see Section 6.1.3).

We now define the components of the 3D-Var scheme on the basis that the state vector contains the ice thickness variables only, i.e.

$$\mathbf{z}_k = \mathbf{H}_k, \quad (6.4)$$

with  $\mathbf{z}_k \in \mathbb{R}^N$ , for the  $N$  mesh points in the model.

### 6.1.1 Observation Operator

The observation operator maps the state vector to observational space so that it is directly comparable to the observations. The primary variable in our shallow ice model is the thickness of the ice,  $h$ . Observing the ice thickness directly provides a value for the thickness itself, along with positional information for the location of the observation. Since the location is unlikely to align with the mesh points in a model, we use a linear interpolation technique to express the observation in terms of the nearest mesh points. An appropriate form for a single observation  $y_j$  located between the mesh points  $x_{i-1}$  and  $x_i$  would be

$$y_j = \beta_1 h_{i-1} + \beta_2 h_i, \quad (6.5)$$

where  $\beta_1$  and  $\beta_2$  are interpolation coefficients defined as follows. Let observation  $y_j$  occur at known location  $x^*$ , then

$$\beta_1 = \frac{x_i - x^*}{x_i - x_{i-1}}, \quad \text{and} \quad (6.6)$$

$$\beta_2 = \frac{x^* - x_{i-1}}{x_i - x_{i-1}}. \quad (6.7)$$

Therefore for every observation of ice thickness, the corresponding row  $j$  in  $\mathbf{C}$  contains the coefficients  $\beta_1$  and  $\beta_2$  located at  $C_{j,i-1}$  and  $C_{j,i}$  respectively. We assume that every observation lies within the numerical domain of the model.

### 6.1.2 Observation Error Covariance Matrix

The observation error covariance matrix  $\mathbf{R}$  is a symmetric, positive definite  $p \times p$  matrix. It represents the uncertainty in the errors in the observations which may arise from sources such as inaccuracies of the measuring instrument, subscale features that are too small to represent in the model or errors in the observation operator  $\mathbf{C}$ . As this matrix is related to errors in the observations and not the dynamical model it is independent of the moving mesh method.

A common assumption is to treat the errors in each observation as independent of the others, a reasonable assumption with direct measurements. Using observations of

the ice thickness means we may treat  $\mathbf{R}$  as a diagonal matrix. If each observation has the same error variance,  $\sigma_o^2$ , we may write the observation error covariance matrix as

$$\mathbf{R} = \sigma_o^2 \mathbf{I}, \quad \mathbf{R} \in \mathbb{R}^{p \times p}. \quad (6.8)$$

### 6.1.3 Background Error Covariance Matrix

The background error covariance matrix  $\mathbf{B}$  is a symmetric, positive definite  $q \times q$  matrix representing the uncertainty in the errors in the prior state of the system.

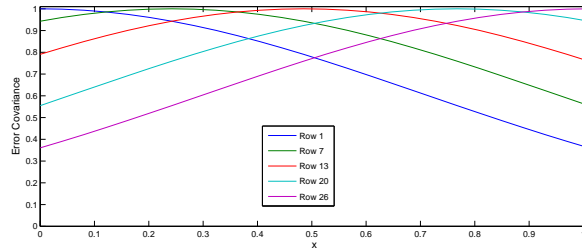
This matrix is crucial, particularly in the optimal 3D-VAR scheme as it contributes towards the spread of information from observations to the state variables. It is common to approximate the error covariances using an analytic correlation function. There are many options available, the simplest would be to define  $\mathbf{B}$  as a diagonal or tri-diagonal matrix; however, in a problem such as ice sheet modelling observations can be sparsely distributed and these simple options limit the spread of information from observations so are generally insufficient [28].

Instead we define a modified Gaussian function [91] which is defined over the entire domain and depends on the distance between the grid points of variables. The elements of  $\mathbf{B}$  are given by

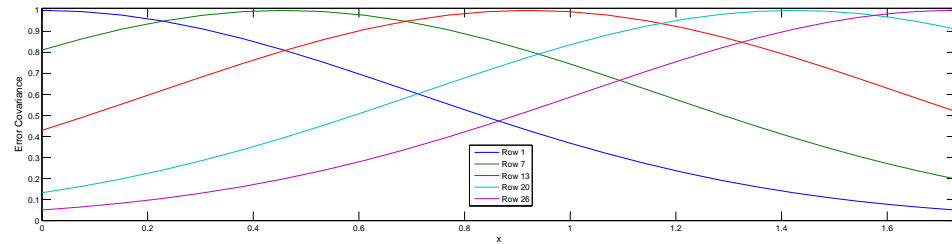
$$b_{ij} = \sigma_b^2 \exp^{-L(x^{(i)} - x^{(j)})^2}, \quad i, j = 1, \dots, N \quad (6.9)$$

where  $L$  is the inverse of a background correlation length scale and  $\sigma_b^2$  is the error variance associated with each ice thickness variable. On an evenly spaced grid each row (or column) forms similar functions across the domain centred on different values of  $x$  (see Figure 6.1(a)).

The modified Gaussian function Eq. (6.9) is not restricted to an evenly spaced grid, which is beneficial to both  $h$ - and  $r$ - adaptive mesh methods. Moreover as the mesh evolves according to a moving mesh approach, the function reflects this with larger values in locations where the mesh nodes have moved closer together and a reduction when they have moved further apart. For instance using the test scenario from Section 5.5.1 with 26 mesh nodes and  $\beta = 1$ , when  $t = 12000$  the same rows of the matrix now have the structure in Figure 6.1(b) since the nodes near the glacier front are closer together



(a)



(b)

**Figure 6.1:** A modified SOAR equation for rows of  $\mathbf{B}$  relating to different places in the domain. a) evenly spaced grid with even structure, b) unevenly spaced mesh after evolution.

than those near the divide.

By viewing all of the rows together we are able to see the global change in the covariances as a result of the change in mesh. Figure 6.2 shows the elements of the background error covariance matrix, where the colour in position  $i, j$  represents the size of  $\mathbf{B}_{i,j}$ . Initially the mesh is evenly spaced and the matrix  $\mathbf{B}$  has a striped diagonal structure (Figure 6.2(a)). As the domain increases in size and the mesh nodes spread out, we see two main differences (Figure 6.2(b)). Firstly there are smaller covariances in the outer regions since the domain, and thus the overall distance between mesh points, has increased in size. Secondly, the mesh is no longer evenly spaced so the striped diagonal structure has curved to reflect areas where the nodes are closer, specifically towards the moving front. This allows control on how information is passed between the variables as the mesh evolves. In these figures the number of mesh nodes has been increased to 121 in order to demonstrate the changes smoothly.

One of the drawbacks of the 3D-VAR method is that the background error co-

variances are static, whereas by defining the matrix  $\mathbf{B}$  in the form above involves a recalculation at each assimilate time. The error covariances are then determined by the mesh evolution and implicitly depend on the non-linear flow of the numerical model. More advanced data assimilation schemes such as the Kalman Filter method introduced in Section 4.2.2 directly evolve the background error covariance matrix is using the model equations, generally in a linear form.

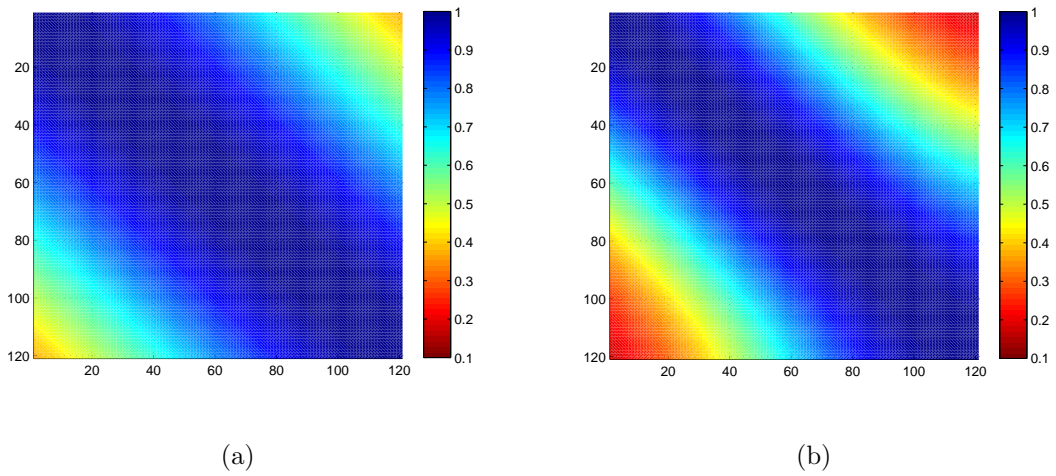


**Figure 6.2:** Background error covariance matrix  $B$  using the Gaussian function Eq. (6.9); a) at the initial time when the mesh is evenly spaced, b) at  $t = 12000$  when the mesh has moved.

### 6.1.4 Analysis Solution and Mass Conservation

By performing a step of an assimilation scheme the mass of the glacier is altered using external information in the form of observations of ice thickness. The CMF moving mesh method detailed in Section 5.3.1 is based on conserving relative mass. It is clear that the conservation principle (Eq. (5.42))

$$\frac{1}{\theta(t)} \int_0^{\hat{x}(t)} h dx = \mu(\hat{x}), \quad (6.10)$$

used to define the mesh deformation velocity and the ice thickness profile no longer holds when an assimilation step is made. Therefore an analysis solution or ‘reset’ of

some of the values is required before the numerical model can continue. Therefore at every assimilation cycle, after calculating the analysis solution to the ice thickness using Eq. (6.1), we recalculate the total mass  $\theta$  such that the analysis solution of the mass is

$$\theta^a(t) = \int_0^{b^a(t)} h^a dx, \quad (6.11)$$

and the mass fraction constants  $\mu$  are redefined as

$$\frac{1}{\theta^a(t)} \int_0^{\hat{x}^a(t)} h^a dx = \mu^a(\hat{x}^a), \quad (6.12)$$

before the forecast step in the dynamical model. The analysis mass and equivalent mass fraction constants then correspond to the analysis estimation of the state variables.

Alternatively we could treat the total mass variable  $\theta$  as an unknown variable and include it within the state vector (Eq. (6.15)). This would involve extending the background error covariance matrix  $\mathbf{B}$  and as a result the complexity, but would open up the possibility of including ‘observations’ of the total mass from sources such as energy balance or global climate models.

The reset requirement is specific to the conservation based methods of mesh movement, models which do not depend on the total mass will not experience this issue. In this work we will calculate the analysis solution to the total mass and mass fraction constants at the end of the assimilation step.

### 6.1.5 3D-Var Algorithm for CMF Moving Mesh

We now present the 3D-VAR algorithm for assimilating on a moving domain using the conservation of mass fractions method from Section 5.3.1.

1. Calculate a forecast of the state vector  $\mathbf{z}^f$  by evolving the numerical model of the CMF method (Section 5.4.1) using the previous analysis solution as model inputs. This gives forecast values of the numerical mesh  $\mathbf{X}^f$ , the ice thickness  $\mathbf{H}^f$  and the total mass  $\theta^f$ . We also know the constant in time mass fractions  $\mu$ .
2. Use the optimal 3D-VAR formulation (Eq. (6.1)) to produce a new analysis solution of the ice thickness  $\mathbf{H}^a$  using observations available at the current time. The

analysis solution to the numerical mesh is identical to the forecast, with  $\mathbf{X}^a = \mathbf{X}^f$ .

3. Calculate the analysis solution of the total mass  $\theta^a$  and update the mass fractions  $\mu^a$  using Eqs. (6.11) and (6.12).
4. Evolve the analysis solution using the dynamical model to produce a forecast at the next time step.
5. Repeat steps 2-4.

## 6.2 A Test Experiment

We will now test the 3D-VAR method applied to the moving mesh method using the test scenario in Section 5.5.1. Since we are using a test scenario, real observations do not exist and need to be generated from the numerical model. To achieve this we assume the true initial conditions are known and the model is perfect. The system is evolved with these initial conditions and the output recorded. Observations are then taken as a sample from this output, with random noise added to replicate observational error.

We then choose a set of initial conditions that are incorrect, from which we evolve the system until a chosen time when we apply the data assimilation scheme using observations from the previous output. This procedure is known as a *twin experiment*.

### 6.2.1 Initial Conditions

#### Reference Solution

To generate the observations for a *twin experiment* we first define the known set of exact initial conditions. Let the true initial ice thickness be the function

$$h = 1 - x^2, \quad x \in (0, 1). \quad (6.13)$$

The system is evolved using the method described in Section 5.4.1, with  $\Delta t = 0.2a$  and the initial domain spacing,  $\Delta x = 0.01m$ , corresponding to 101 mesh points. Both the

reference and forecast models evolve until an end time of  $T = 2000a$ , as we want to see the effects of including observations before the models reach a steady state solution. This design forms our reference solution, the output that provides our observations.

### Forecast Model

For our experiments design we estimate the initial ice thickness by the perturbed function

$$h = 1.1025 - x^2, \quad x \in (0, 1.05), \quad (6.14)$$

where we note that not only is the estimate of the ice thickness different but also the initial domain. As such the estimate of the total mass is different, along with the mass fractions used in the moving mesh method. The time step is taken to be the same as the reference solution so the observations can be taken at times that match the model without the need for temporal interpolation. We use 51 mesh points, an initial spacing of  $\Delta x = 0.021m$ .

By using a higher resolution model for the reference solution we are able to generate more accurate values to use as observations. While this has the potential to introduce errors into the system, experiments have determined that these are negligible.

### 6.2.2 Results

We include sets of 19 observations of ice thickness from the reference solution, taken at  $t = 500$  and  $t = 1500$ , sampled evenly across the domain with random noise taken from a normal distribution  $\epsilon_o \sim N(0, \sigma_o^2)$  with  $\sigma_o^2 = 0.05m$ . The background error variances  $\sigma_b^2$  is also set to  $0.05m$ . This represents an error of approximately 5% of the corresponding variables.

At the first assimilation time,  $t = 500$ , it can be seen in Figure 6.3(a) that there is a large difference between the forecast and reference thickness profiles. The analysis profile on the otherhand resembles the reference, except in the region at the front where the numerical model predicts there should be ice while in fact there is none there. This

is because there is no analysis solution to the numerical mesh. By the second assimilation time,  $t = 1500$  (Figure 6.3(b)), we see the forecast profile, which has evolved from the analysis solution at  $t = 500$ , is closer to the reference profile. This suggests that by solely assimilating observations of ice thickness future evolutions of the dynamical model implicitly propagate information over subsequent time steps. After assimilating at this time we see the analysis profile is even closer to the reference solution.

The implicit spread of information to the numerical mesh is emphasised in Figure 6.3(c) where we see the moving boundary point  $x = b(t)$  being pulled towards the reference location after each assimilation time.

Several experiments with a variety of initial conditions for  $x$  and  $h$ , along with varying samples of observations produced similar levels of improvement to the estimate of the ice thickness profile.

### 6.3 An Extended Scheme: Assimilating the Mesh

Data assimilation methods have been devised for a variety of applications, with the general assumption that the physical domain from which observations are taken and the corresponding representation by the model are known exactly (or at least assumed to be known exactly).

As we have seen the dynamical ice flow scenario (amongst others) occurs on a domain that is evolving in shape and size. In essence, the domain can be as much of an unknown as the variables within, especially since it is evolved using the dynamical model. With this in mind we propose an extension to existing data assimilation methods to directly include the unknown numerical mesh used in a moving mesh modelling process, such as the CMF method in Section 5.3.1.

Of course, the mesh itself has no physical meaning as it is a numerical tool to solve the model equations. While the location of the majority of mesh nodes is arbitrary, there are some exceptions. In particular the domain boundaries are real, physical locations that are assigned mesh nodes. Similarly there could be other key moving features in the interior of the domain which could be assigned mesh nodes in a moving mesh scheme.

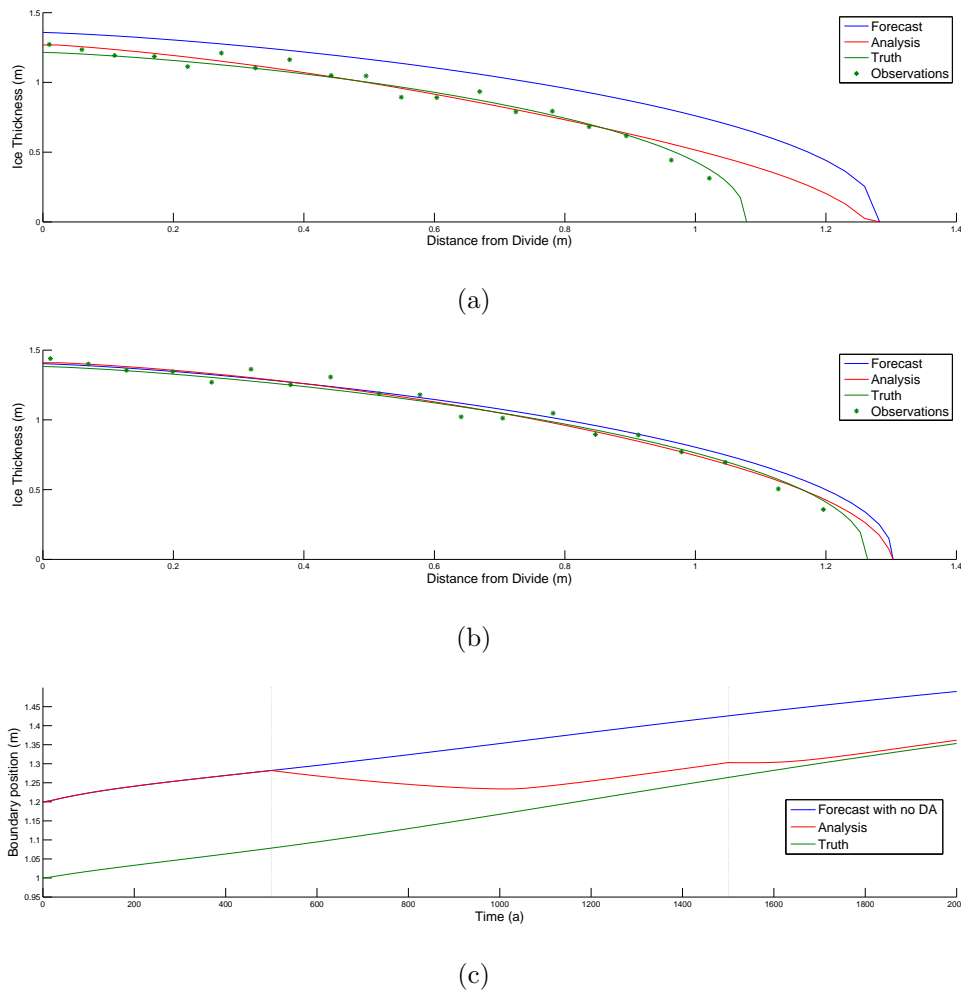


**Figure 6.3:** 1D moving mesh with data assimilation:- a-b) show the forecast, analysis and true ice thickness profile at  $t = 500$  and  $1500$  respectively, indicating the observations after noise is added. c) shows the time evolution of the boundary point  $x = b(t)$ .

For example r-adaptive mesh methods are often used to locate the grounding line (see [39; 24]), the point at which grounded ice begins to float. If the locations features such as this are observable then we may wish to include these types of observations. In this work we focus solely on observing the boundary.

In one-dimension the two mesh points at either end of the domain  $X_1$  and  $X_N$  are situated on the boundary and represent a physical location. These locations, fixed or otherwise, are observable points that we may make use of in a data assimilation scheme. While there is a limited number of these ‘physical’ mesh nodes, most moving

mesh methods rely on a known connectivity between points and so the extension to the data assimilation scheme must include all the nodes within the domain to avoid mesh tangling. The state vector  $\mathbf{z}$  in Eq. (6.1) becomes

$$\mathbf{z}_e = \begin{pmatrix} \mathbf{X} \\ \mathbf{H} \end{pmatrix}, \quad (6.15)$$

to accommodate the mesh nodes. The use of subscript  $e$  determines a component that has been extended.

The size of the state vector has increased by the number of mesh points ( $N$ ) in the model. Since our state vector previously only contained ice thickness variables located at each of these points,  $\mathbf{z}_e \in \mathbb{R}^{2N}$  is now twice the size of the original state vector. Extending the state vector will alter the other components of the data assimilation scheme, which we shall detail here.

### 6.3.1 Observation Operator Extension

The observation operator for observations of ice thickness can be extended by writing

$$\mathbf{C}_e = \begin{pmatrix} \mathbf{0} & \mathbf{C} \end{pmatrix} \quad (6.16)$$

where  $\mathbf{C}_e \in \mathbb{R}^{p \times 2N}$  and  $\mathbf{C} \in \mathbb{R}^{p \times N}$  is the observation operator before the extension detailed in Section 6.1.1.

In addition we wish to include observations of positional features, such as the boundary location. The observation operator may then be written

$$\mathbf{C}_e = \begin{pmatrix} \mathbf{C}_x & \mathbf{0} \\ \mathbf{0} & \mathbf{C} \end{pmatrix}, \quad (6.17)$$

where the rows in  $\mathbf{C}_x$  correspond to observations of positional features. These observations differ from standard observations in that instead of each observation representing a variable with a corresponding position, the information is solely of the position of a feature itself.

Since in one-dimension our moving mesh model estimates these features by associating a mesh point to them, there is a direct one-to-one relationship between the

observation of the position and the model estimation of this position. Therefore no interpolation is required and each row in  $\mathbf{C}_x$  consists solely of a 1 in the column associated with the mesh point for that boundary.

### 6.3.2 Observation Error Covariance Matrix Extension

The extended observation error covariance matrix still assumes the observations are independent, and as such we may write

$$\mathbf{R}_e = \begin{pmatrix} \mathbf{0} & \mathbf{R} \\ \sigma_{ox}^2 \mathbf{I} & \mathbf{0} \end{pmatrix} \quad (6.18)$$

where  $\sigma_{ox}^2$  is the error variance relating to observations of positional features.

### 6.3.3 Background Error Covariance Matrix Extension

The biggest change under the extended scheme lies within the background error covariance matrix. We may write the matrix in the form

$$\mathbf{B}_e = \begin{pmatrix} \mathbf{B}_{xx} & \mathbf{B}_{xh} \\ (\mathbf{B}_{xh})^T & \mathbf{B} \end{pmatrix}, \quad (6.19)$$

where  $\mathbf{B}_{xx}$  represents the error covariance matrix between the mesh points and  $\mathbf{B}$  is the previous matrix of error covariances for the ice thickness variables. The matrix  $\mathbf{B}_{xh}$  represents the covariances between errors in the mesh points and the ice thickness which we refer to as the cross-covariance matrix.

The error covariances relating to the ice thickness, matrix  $\mathbf{B}$ , are the same as the original background error covariance matrix defined in Section 6.1.3 using a modified Gaussian function (Eq. (6.9)). Similarly the errors in the mesh node locations can also be defined by their proximity to each other and as such we may define their covariances using the same modified Gaussian function

$$\{\mathbf{B}_{xx}\}_{ij} = \sigma_{bx}^2 \exp^{-L(x(i)-x(j))^2}, \quad i, j = 1, \dots, q \quad (6.20)$$

with a different variance  $\sigma_{bx}$ .

Since the mesh is an artificial representation of the domain, it is not immediately clear how to define  $\mathbf{B}_{xh}$ . While there exists a relationship between the mesh nodes and the ice thickness variables through the moving mesh conservation principle (Eq. (5.42)), it is non-linear. Other moving mesh methods may contain a linear relationship, but for the method used in this thesis we seek an alternative. One approach is to assume there is no relationship at all and define the cross-covariance error matrix as a  $N \times N$  zero matrix

$$\mathbf{B}_{xh} = \mathbf{0}. \quad (6.21)$$

This means that at the point of assimilation no information from observations regarding the mesh is passed to the ice thickness variables and vice versa, with the matrix  $\mathbf{B}$  taking the form in Figure 6.4(a). Therefore unless there are observations of both the ice thickness and the mesh nodes, the analysis solution relies on future progression of the numerical model to filter information through and the extended scheme is superfluous.

A second approach relates the mesh nodes that correspond to physical points with the other variables. In our model the first and last mesh point correspond to the physical domain boundaries, which we relate to the ice thickness variables across the domain. We define this relationship using the modified Gaussian function Eq. (6.9), where the corresponding rows of  $\mathbf{B}_{xh}$  are given by:

$$\{\mathbf{B}_{xh}\}_{1j} = \sigma_{bxh}^2 \exp^{-L(x(1)-x(j))^2}, \quad \text{and} \quad (6.22)$$

$$\{\mathbf{B}_{xh}\}_{Nj} = \sigma_{bxh}^2 \exp^{-L(x(N)-x(j))^2}, \quad j = 1, \dots, q, \quad (6.23)$$

with variance  $\sigma_{bxh}^2$ .

The structure of the matrix  $\mathbf{B}$  under these two approaches is visible in Figure 6.4 and we shall discuss the impact of each method through the experiments below.

A major drawback of extending the scheme is the size of the background error covariance matrix, which is *four* times the size. For systems with a large number of mesh points this may increase the computational requirements to an unfeasible level.

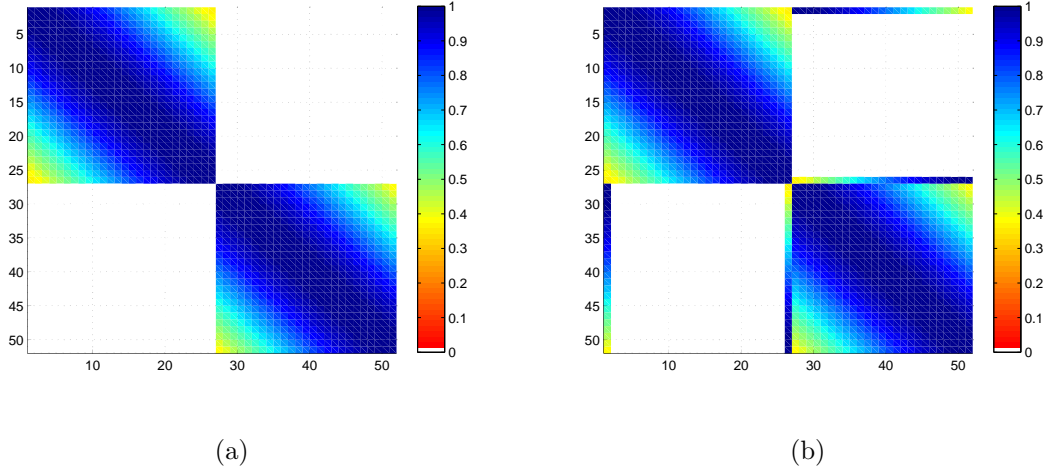


**Figure 6.4:** Background error covariance matrix for the extended scheme; a) without cross covariance terms between the mesh and the ice thickness, b) with cross covariances between the boundary points and the ice thickness providing additional rows/columns.

### 6.3.4 Extended 3D-Var Algorithm for CMF Moving Mesh

The algorithm for the extended 3D-VAR scheme applied to the CMF moving mesh method is given by:

1. Calculate a forecast of the state vector  $\mathbf{z}^f$  by evolving the numerical model of the CMF method (Section 5.4.1) using the previous analysis solution as model inputs. This gives forecast values of the numerical mesh  $\mathbf{X}^f$ , the ice thickness  $\mathbf{H}^f$  and the total mass  $\theta^f$ . We also know the constant in time mass fractions  $\mu$ .
2. Use the optimal 3D-VAR formulation (Eq. (6.1)) to produce a new analysis solution of both the numerical mesh  $\mathbf{X}^a$  and ice thickness  $\mathbf{H}^a$  using observations available at the current time.
3. Calculate the analysis solution of the total mass  $\theta^a$  and update the mass fractions  $\mu^a$  using Eqs. (6.11) and (6.12).
4. Evolve the analysis solution using the dynamical model to produce a forecast at the next time step.
5. Repeat steps 2-4.

## 6.4 Extended Scheme Experiments

Now that we have an extended data assimilation scheme capable of producing an analysis solution to the numerical mesh we will use the experimental design in Section 6.2 to investigate this scheme and its ability provide a better estimate of the state of the system. The observation noise is kept constant between these experiments so results are directly comparable. We will evaluate the impact of using observations of the boundary within the scheme, both with and without the cross covariance terms introduced in Section 6.3.3. The results are compared to the solution before the extension, as seen in Figure 6.3, which we shall refer to as the benchmark solution.

### 6.4.1 Observing the Boundary

We now include an observation of the moving boundary ( $x = b(t)$ ), in addition to the ice thickness observations, at both assimilation times,  $t = 500$  and  $t = 1500$ . The boundary observations are taken from the reference solution with random noise sampled from a normal distribution  $\epsilon_o \sim N(0, \sigma_{ox}^2)$  with  $\sigma_{ox}^2 = 0.05m$ . To demonstrate the impact of including these observations let the cross covariance background error variance  $\sigma_{bxh}^2 = 0m$  (i.e. Eq. (6.21) holds), which means no information is passed from the thickness profile to the mesh at the time of assimilation. As you can see in Figure 6.5(a), the extent of the domain is corrected along with the thickness profile. Since no information is passed between the mesh and the ice thickness, at the time of assimilation the analysis profile is actually a transformed version of Figure 6.3(a), i.e. the profile is identical but on a squeezed domain.

In Figure 6.5(b) we notice that the forecast profile is significantly closer to the true ice thickness profile than the forecast profile without a boundary observation shown in Figure 6.3(b). We can also see a ‘jump’ towards the true location of the boundary at the time of assimilation in Figure 6.5(c). As a result the convergence towards the true boundary location is significantly quicker than before.

It is also vital that the mesh points do not tangle when we alter the mesh at the as-

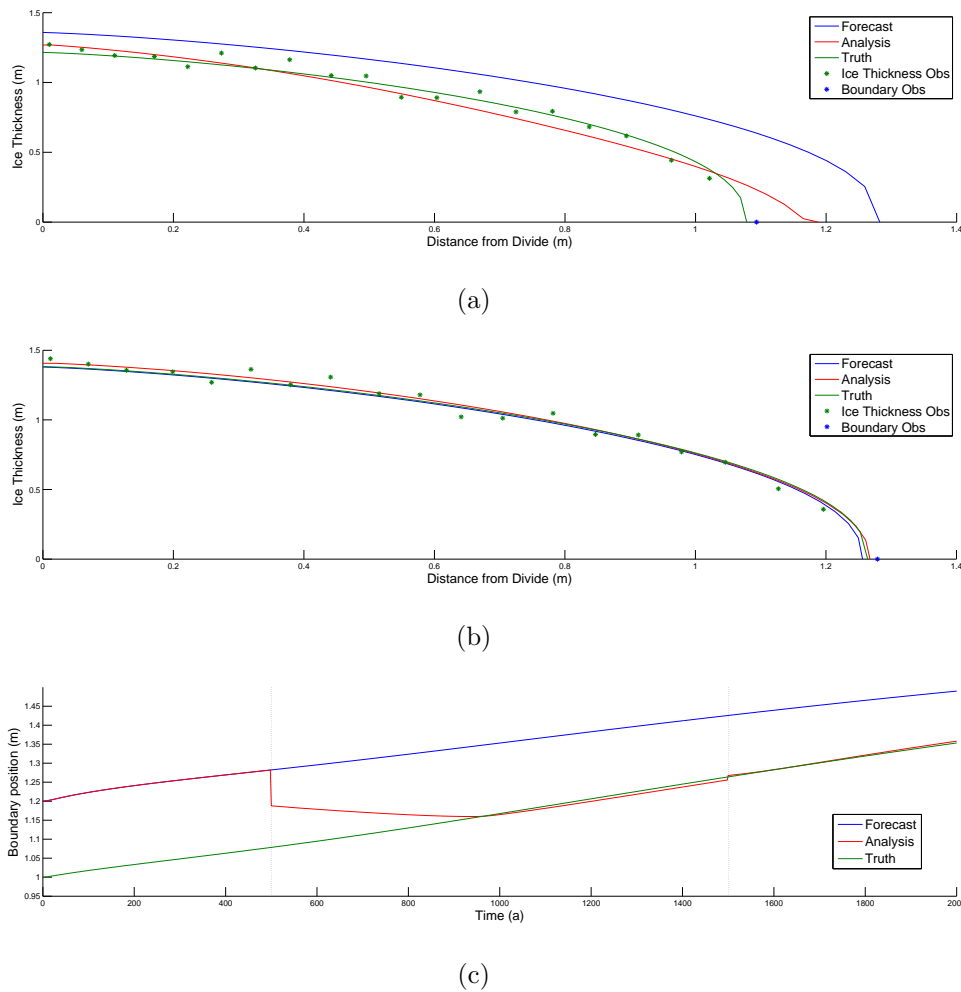


**Figure 6.5:** 1D moving mesh with data assimilation including observations of the boundary:- a-b) show the forecast, analysis and true ice thickness profile at  $t = 500$  and 1500 respectively, along with the observations after noise is added. c) shows the time evolution of the boundary point  $x = b(t)$ .

simulation point. Figure 6.6 shows the evolution of the mesh points for the benchmark scenario and the case including observations of the boundary. Naturally the benchmark solution evolves regularly with no influence on the mesh from any observations (Figure 6.6(a)), while the impact including a boundary observation in the assimilation is visible in Figure 6.6(b) by a change in direction of mesh nodes near the boundary. When the boundary observation is included we see an immediate knock on effect on the interior mesh points all the way across the domain, evident by the sharp ‘ridge’

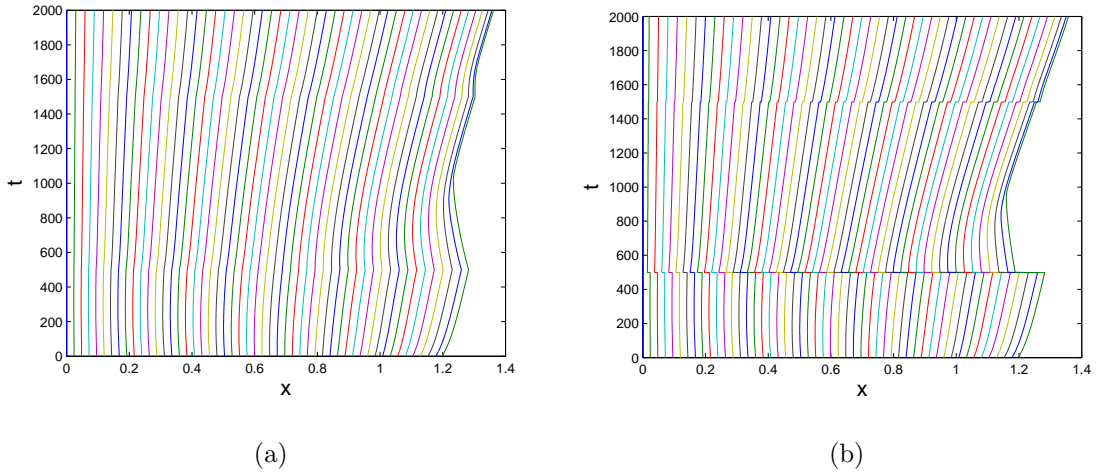


**Figure 6.6:** 1D moving mesh with data assimilation:- evolution of mesh nodes through time. a) benchmark solution, b) including observations of the boundary.

that appears at the assimilation times. This is due to the Gaussian function in  $\mathbf{B}_{xx}$  (Eq. (6.20)) spreading the information of the boundary location through the rest of the mesh.

## 6.4.2 Including Cross-Covariances

This next experiment analyses the impact of the cross-covariance part (Eqs. (6.22) and (6.23)) of the background error covariance matrix  $\mathbf{B}$  detailed in Section 6.3.3. We set  $\sigma_{bxh}^2 = 0.0075m$  in Eqs. (6.22) and (6.23) to allow information to be passed between the mesh and the ice thickness, but with a weaker relationship than exists between the mesh nodes or the ice thickness variables.

We see in Figure 6.7(a) that without observing the boundary the analysis estimate of the domain is an improvement over the forecast. While the improvement is not as significant as the scenario with a boundary observation (Figure 6.5(a)), it is still preferable to the benchmark solution where the domain is fixed at an assimilation time.

By including both the cross-covariance terms and a boundary observation we are making use of all the information available, which results in a further improvement at the first assimilation time,  $t = 500$ , as can be seen in Figure 6.8(a). By the second

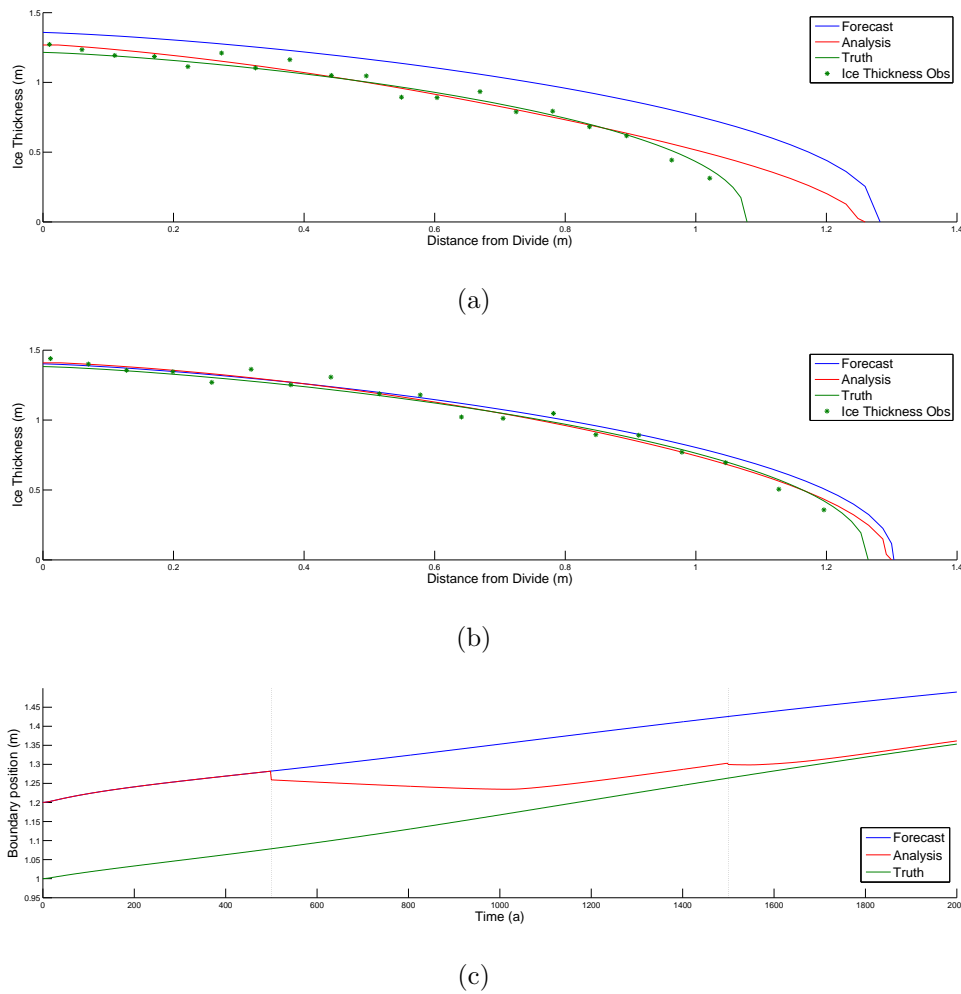


**Figure 6.7:** 1D moving mesh with data assimilation including cross-covariance terms in the extended background error covariance matrix,  $\mathbf{B}_e$ :- a-b) show the forecast, analysis and true ice thickness profile at  $t = 500$  and 1500 respectively, along with the observations after noise is added. c) shows the time evolution of the boundary point  $x = b(t)$ .

assimilation time,  $t = 1500$ , the forecasted profile is virtually indistinguishable from the true profile. At this point the random noise on the observations means the analysis solution is a slightly worse estimate of the truth, though the amount is negligible.

### 6.4.3 Discussion

We have shown that by extending the data assimilation scheme to incorporate the numerical mesh the prediction of the numerical domain and as a result the overall ac-

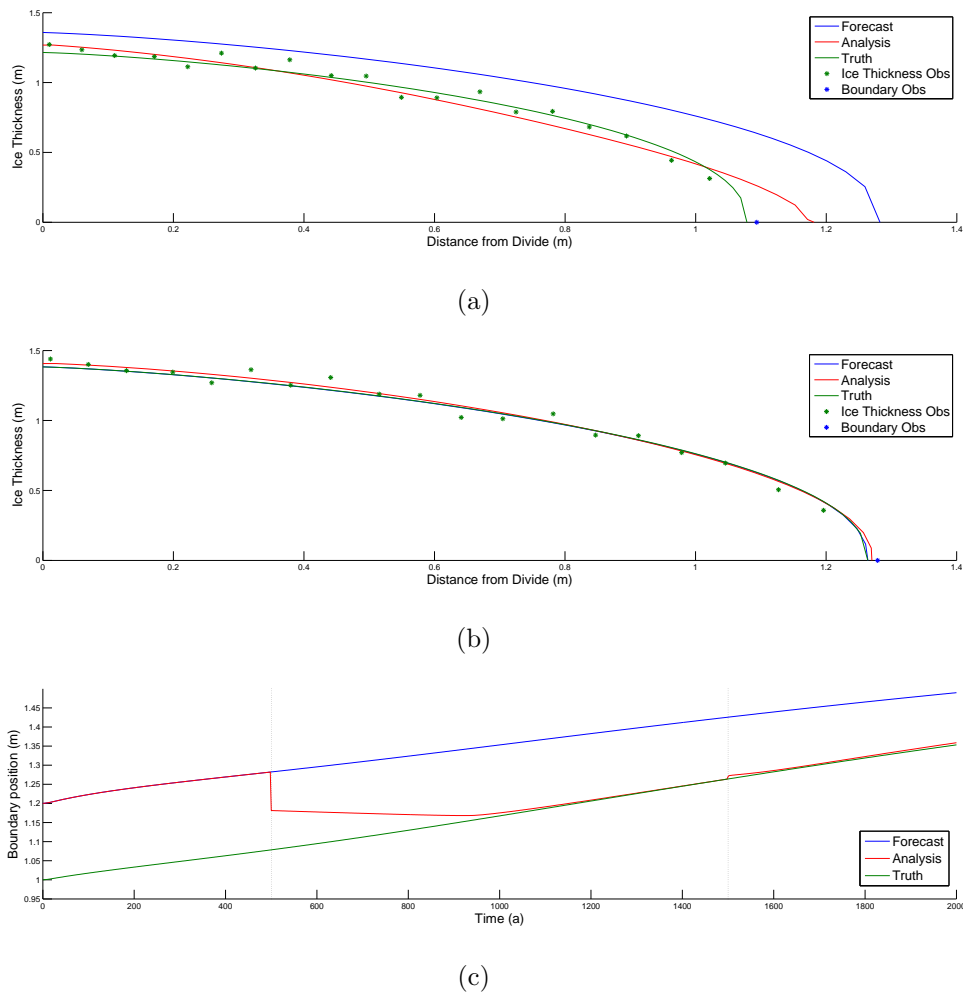


**Figure 6.8:** 1D moving mesh with data assimilation including cross-covariance terms in  $\mathbf{B}$  and boundary observations:- a-b) show the forecast, analysis and true ice thickness profile at  $t = 500$  and  $1500$  respectively, along with the observations after noise is added. c) shows the time evolution of the boundary point  $x = b(t)$ .

curacy is improved. The largest improvements in accuracy arose when observations of the boundary were directly included, while defining a cross-covariance matrix to spread the information from observations between the mesh and the ice thickness also saw improvements over the ordinary scheme.

In addition, experiments designed to explore the effects of the quantity of observations, along with their distribution in space and time show the scheme, both ordinary and extended, consistently improve the overall accuracy and are robust enough to cope

with the variations.

## 6.5 Summary

In this chapter we presented the 3D-VAR data assimilation scheme and detailed the differences to the various components that make up the scheme when applied is a moving mesh compared with a fixed grid. We discussed the need for an analysis solution to the total mass and mass fractions for the chosen method of mesh movement to ensure the mass conservation required.

We then tested the scheme using a twin experiment, where results showed the scheme can achieve improved predictions of the ice thickness profile at the moment of assimilation. This improvement then implicitly improved the estimate of the domain over future evolutions of the model.

We then provided an extension to the scheme to include the numerical domain in the state vector, with the aim of improving our prediction of the domain at the assimilation time. This allowed observations of positional co-ordinates to be included. The extended scheme included changes to the structure of many of the features in the 3D-VAR methods which we detailed.

We saw the benefits of the extended scheme to the analysis solution. We examined the impact of including an observation of the boundary, along with a cross-covariance relationship between the errors in the numerical mesh and the ice thickness profile. By including these cross-covariance terms we showed the improvement to the domain prediction, both with and without observations of the boundary.

# Chapter 7

## A 2D Moving Glacier Model

In this chapter we look at the shallow ice model in two horizontal dimensions. We begin by considering the total mass of the glacier and how it evolves over time, before non-dimensionalising the shallow ice PDE to remove the physical units.

We then extend the CMF moving mesh procedure for modelling ice sheet flow into two spatial dimensions by deriving a weak formulation of the relative mass conservation principle. The weak form may then be approximated using a finite element approach. We demonstrate the method using a test problem, before comparing results of the EISMINT scenario to both fixed grid and exact solutions.

### 7.1 The 2D Shallow Ice PDE

A one-dimensional flowline model such as the one presented in Section 5.3 is useful for providing a general view of simple glacial movement, but it is only applicable in certain scenarios. We therefore extend this model into two dimensions to include the flow in both horizontal directions with the aim of producing a more complete picture of the movement. In two dimensions the shallow ice mass balance equation (Eq. (2.14)) takes the form

$$h_t = m - \nabla \cdot (h\mathbf{u}) \tag{7.1}$$

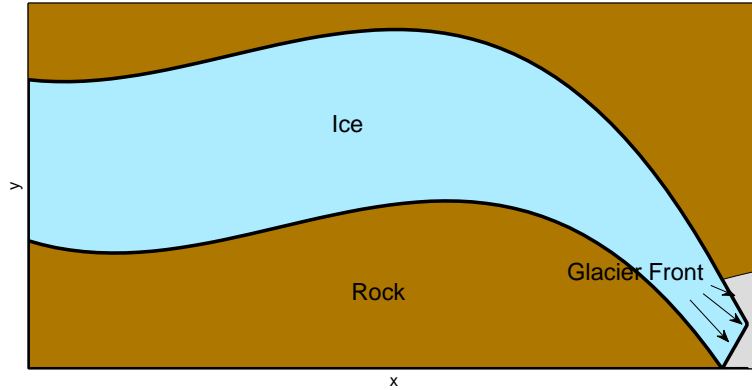


**Figure 7.1:** Arbitrary two-dimensional domain  $\Omega(t)$ , with a moving boundary exhibiting a Dirichlet condition at the glacier front ( $\Gamma_D$ ) and Neumann boundary conditions ( $\Gamma_N$ ) along the rock walls

where  $h = h(\mathbf{x}, t)$  is the thickness of the ice and  $m = m(\mathbf{x}, t)$  represents the ice-equivalent accumulation rate, both given in terms of positional coordinates  $(x, y)$ . The diffusive velocity  $\mathbf{u}$  is defined to have components  $(u^x, u^y)^T$ , which describes the flow in the  $x$  and  $y$  directions respectively.

A two-dimensional domain, Figure 7.1 for example, possesses two types of boundary. In the upper regions of a glacier and along the valley sides the boundary is defined by a rock face or slower moving ice, which we denote by  $\Gamma_N$ . There can be no flow across this boundary, so there exists a no-flux Neumann condition written as

$$\frac{\partial h}{\partial n} = 0, \quad \mathbf{u} \cdot \mathbf{n} = 0 \quad \text{on } \Gamma_N. \quad (7.2)$$

In the regions not bounded by these geographical features the ice meets the glacier bed and the boundary is free to move. This (Dirichlet) boundary is denoted  $\Gamma_D$  with the condition

$$h = 0 \quad \text{on } \Gamma_D. \quad (7.3)$$

### 7.1.1 Integral Property of Total Mass

We first consider the total mass of the glacier and its evolution over time. As in the one-dimensional case let  $\theta$  represent the total mass of the system. In two dimensions on a domain  $\Omega(t)$  this is defined as

$$\theta = \int_{\Omega(t)} h d\mathbf{x}, \quad (7.4)$$

under the assumption that density is constant. Differentiating Eq. (7.4) with respect to time using the Reynolds Transport Theorem (see Section B.4 for details, [90]) gives

$$\dot{\theta} = \frac{d}{dt} \int_{\Omega(t)} h d\mathbf{x}, \quad (7.5)$$

$$= \int_{\Omega(t)} h_t d\mathbf{x} + \oint_{\Gamma} (\mathbf{v} \cdot \mathbf{n}) h d\mathbf{x}. \quad (7.6)$$

where  $\mathbf{v} = |\mathbf{v}(\mathbf{x}, t)|$  is the component of the velocity at the boundary. Under the boundary conditions Eqs. (7.2) and (7.3) the surface integral term is zero. This leaves a volume integral over the whole domain. Substituting for  $h_t$  from the mass continuity PDE, Eq. (7.1), gives

$$\dot{\theta} = \int_{\Omega(t)} m d\mathbf{x} - \int_{\Omega(t)} \nabla \cdot (h\mathbf{u}) d\mathbf{x}. \quad (7.7)$$

In order to evaluate the divergence in the second term of Eq. (7.7) we note that since  $(h\mathbf{u})$  is continuous and differentiable we may apply the Divergence Theorem (see Section B.5) to obtain

$$\dot{\theta} = \int_{\Omega(t)} m d\mathbf{x} - \oint_{\Gamma} (h\mathbf{u}) \cdot \mathbf{n} d\mathbf{x}, \quad (7.8)$$

where again application of the boundary conditions force the surface integral to be zero. This leaves us with the expression

$$\dot{\theta} = \frac{d}{dt} \int_{\Omega(t)} h d\mathbf{x} = \int_{\Omega(t)} m d\mathbf{x} \quad (7.9)$$

to represent the change in total mass. As with the one-dimensional case this means that any change in the ice mass comes from the net effect of the source term over the entire glacier.

### 7.1.2 Non-Dimensionalisation of the Shallow Ice PDE

For many problems it is beneficial to non-dimensionalise the variables in order to avoid extreme values and understand the relative strengths of the features. Each variable within the PDE is scaled by a constant parameter to leave a dimensionless variable. The transformed variables for ice thickness, accumulation and flow velocity are given by

$$\bar{h} = \frac{h}{[h]}, \quad \bar{m} = \frac{m}{[m]}, \quad \bar{\mathbf{u}} = \frac{\mathbf{u}}{[u]}, \quad (7.10)$$

where the non-dimensional variables are represented with an overbar and the scaling parameters by square brackets. Similarly the non-dimensional time and space variables are

$$\bar{t} = \frac{t}{[t]}, \quad \bar{\mathbf{x}} = \frac{\mathbf{x}}{[l]}. \quad (7.11)$$

We can therefore write the shallow ice PDE from Eq. (7.1) in the form

$$\frac{[h]}{[t]} \bar{h}_{\bar{t}} = [m] \bar{m} - \frac{[h][u]}{[l]} \nabla \cdot (\bar{h} \bar{\mathbf{u}}) \quad (7.12)$$

It is important that the scaled shallow ice expression, Eq. (7.12), maintains the same balance of terms as the original PDE. Therefore to maintain balance

$$\frac{[h]}{[t]} = [m] = \frac{[h][u]}{[l]} \quad (7.13)$$

By definition of the shallow ice equation, the flat bed flow velocity  $\mathbf{u} = ch^4 |\nabla h|^2 \nabla h$  is given in terms of the ice thickness and gradient, which implies the scaling for the diffusive velocity is of the form

$$[u] = \frac{[h]^7}{[l]^3}. \quad (7.14)$$

Putting this into Eq. (7.13) implies that balance will be maintained provided

$$[h]^7 [t] = [l]^4. \quad (7.15)$$

Therefore to non-dimensionalise the shallow ice equation the user must define two scaling parameters from  $[h]$ ,  $[t]$  and  $[l]$ . Then the remaining parameter in Eq. (7.15) and  $[m]$  in Eq. (7.13) can be found such that the non-dimensional shallow ice PDE in

Eq. (7.12) has the same balance of terms as the full equation. We can then solve the modified PDE using the same techniques as before, with the output re-dimensionalised at the end. To save notation becoming cumbersome we shall express equations hereafter using the original notation; however, the results shown were calculated using a non-dimensionalised model.

## 7.2 Glacier Movement

In one dimension we developed a moving mesh method to describe the net glacier movement using a conservation principle to maintain relative mass over time. This method was then implemented numerically using a finite difference scheme to approximate the relevant equations. For a two-dimensional moving problem, finite differences are not a viable option as it is difficult to estimate the diffusion terms in Eq. (7.1) and the risk of mesh tangling is high. Instead we seek a finite element approximation which admits a locally once differentiable function. With this in mind the CMF method can be derived in a weak form to facilitate the finite element approach.

### 7.2.1 Conserving Mass Fractions (CMF) - Weak Formulation

The relative mass of a glacial subdomain with constant density is conserved through time according to the CMF principle

$$\frac{1}{\theta} \int_{\omega(t)} h d\mathbf{x} = \mu, \quad (7.16)$$

where  $\mu$  is constant in time and is applied to any moving subdomain  $\omega(t) \in \Omega(t)$ . The total mass  $\theta$  is defined in Eq. (7.4). To express Eq. (7.16) in a weak form we replace  $\omega(t)$  by  $\Omega(t)$  and include a continuous, differentiable test function  $w$ ,

$$\frac{1}{\theta} \int_{\Omega(t)} w h d\mathbf{x} = \mu, \quad (7.17)$$

where the  $w$  form a partition of unity. With this weak form we extract the net velocity by first differentiating Eq. (7.17) with respect to time to give

$$\frac{d}{dt} \left( \int_{\Omega(t)} wh d\mathbf{x} \right) = \mu \dot{\theta}. \quad (7.18)$$

To perform the time differentiation on the left hand side of Eq. (7.18) we employ the Reynolds Transport Theorem (Section B.4) to change from a Lagrangian perspective to an Eulerian one to produce

$$\int_{\Omega(t)} (wh)_t d\mathbf{x} + \oint_{\Gamma(t)} (wh)(\mathbf{v} \cdot \mathbf{n}) d\Gamma = \mu \dot{\theta}, \quad (7.19)$$

which by the product rule of differentiation gives

$$\int_{\Omega(t)} w_t h + wh_t d\mathbf{x} + \oint_{\Gamma(t)} (wh)(\mathbf{v} \cdot \mathbf{n}) d\Gamma = \mu \dot{\theta}. \quad (7.20)$$

The boundary integral contains the normal component of the net velocity  $\mathbf{v}$  that we seek on the surface elements  $d\Gamma$ . In order to calculate the velocity  $\mathbf{v}$  we convert the surface integral to a volume integral using the Divergence Theorem, giving

$$\int_{\Omega(t)} [w_t h + wh_t + \nabla \cdot (wh\mathbf{v})] d\mathbf{x} = \mu \dot{\theta}, \quad (7.21)$$

where again utilising the product rule of differentiation

$$\int_{\Omega(t)} [h(w_t + \mathbf{v} \cdot \nabla w) + wh_t + w \nabla \cdot (h\mathbf{v})] d\mathbf{x} = \mu \dot{\theta}. \quad (7.22)$$

By making the assumption that  $w$  is frozen in the moving domain  $\Omega(t)$ , which moves with velocity  $\mathbf{v}$ , it follows that the test function must satisfy the advection equation

$$w_t + \mathbf{v} \cdot \nabla w = 0. \quad (7.23)$$

Combining Eqs. (7.22) and (7.23) leaves

$$\int_{\Omega(t)} [wh_t + w \nabla \cdot (h\mathbf{v})] d\mathbf{x} = \mu \dot{\theta}. \quad (7.24)$$

We can substitute the rate of change in ice thickness  $h_t$  from the shallow ice PDE, Eq. (7.1), into the first term of Eq. (7.24) to give

$$\int_{\Omega(t)} w(m - \nabla \cdot (h\mathbf{u})) + w \nabla \cdot (h\mathbf{v}) d\mathbf{x} = \mu \dot{\theta}, \quad (7.25)$$

leading to

$$\int_{\Omega(t)} w \nabla \cdot (h \mathbf{v}) d\mathbf{x} = \mu \dot{\theta} - \int_{\Omega(t)} w m d\mathbf{x} + \int_{\Omega(t)} w \nabla \cdot (h \mathbf{u}) d\mathbf{x}. \quad (7.26)$$

The net velocity  $\mathbf{v}$  that we seek is now expressed in Eq. (7.26) in terms of spatial gradients. To extract the velocity itself we use integration by parts. Evaluating the left hand side of Eq. (7.26) gives

$$\int_{\Omega(t)} w \nabla \cdot (h \mathbf{v}) d\mathbf{x} = \oint_{\Gamma(t)} (wh \mathbf{v}) \cdot \mathbf{n} d\mathbf{x} - \int_{\Omega(t)} \nabla w \cdot (h \mathbf{v}) d\mathbf{x}, \quad (7.27)$$

$$= - \int_{\Omega(t)} \nabla w \cdot (h \mathbf{v}) d\mathbf{x}, \quad (7.28)$$

after applying the boundary conditions, Eqs. (7.2) and (7.3), which force the boundary integral to be zero since either  $h = 0$  or  $\mathbf{v} \cdot \mathbf{n} = 0$  on the boundary.

Similarly the last term on the RHS of Eq. (7.26) may also be evaluated using integration by parts:

$$\int_{\Omega(t)} w \nabla \cdot (h \mathbf{u}) d\mathbf{x} = \oint_{\Gamma(t)} (wh \mathbf{u}) \cdot \mathbf{n} d\mathbf{x} - \int_{\Omega(t)} \nabla w \cdot (h \mathbf{u}) d\mathbf{x}, \quad (7.29)$$

$$= - \int_{\Omega(t)} \nabla w \cdot (h \mathbf{u}) d\mathbf{x}. \quad (7.30)$$

Again, enforcing the boundary conditions reduces the boundary integral in Eq. (7.29) to zero. Putting Eqs. (7.28) and (7.30) back into the expression for the net velocity (Eq. (7.26)) gives

$$\int_{\Omega(t)} \nabla w \cdot (h \mathbf{v}) d\mathbf{x} = \int_{\Omega(t)} w m d\mathbf{x} - \mu \dot{\theta} + \int_{\Omega(t)} \nabla w \cdot (h \mathbf{u}) d\mathbf{x}. \quad (7.31)$$

Eq. (7.31) is a weak formulation satisfied by the net velocity  $\mathbf{v}$  as a combination of the movement induced by both the source and diffusion parts of Eq. (7.1) for an arbitrary point in a region. Any solution to Eq. (7.31) determines the mechanism by which the domain evolves over time, which we may approximate using finite elements. This can also be simplified to the one-dimensional case where results are comparable to the finite difference approach in Section 5.4.1, but that is not done here.

We note that there is no unique solution to this weak formulation, since it is possible to add to  $h \mathbf{v}$  an arbitrary velocity  $\nabla \times \mathbf{q}$  for some vector field  $\mathbf{q}$  in Eq. (7.26). Here we

assume that  $\mathbf{v}$  is irrotational (not unreasonable for glaciers) and write the velocity in terms of a velocity potential  $\psi$ :

$$\mathbf{v} \approx \nabla\psi, \quad (7.32)$$

which is unique to a constant. Eq. (7.31) can then be written as

$$\int_{\Omega(t)} \nabla w \cdot (h \nabla \psi) d\mathbf{x} = \int_{\Omega(t)} w m d\mathbf{x} - \mu \dot{\theta} + \int_{\Omega(t)} \nabla w \cdot (h \mathbf{u}) d\mathbf{x}. \quad (7.33)$$

### 7.3 A Finite Element Scheme

Now that we have a weak form for the net velocity (in the form of a velocity potential, Eq. (7.33)), based upon the relative mass conservation principle we seek a finite element numerical approximation to model the shallow ice equation.

Any domain  $\Omega(t)$  can be discretised into a set of elements defined by a set of nodes  $\mathbf{X}_1, \mathbf{X}_2 \dots \mathbf{X}_N$  where  $\mathbf{X}_i = (X, Y)_i$ . These nodes can be connected to form a mesh made of triangular elements across the domain. Let us define the test function  $w$  as a piecewise linear basis function,

$$w = \phi_i(\mathbf{x}, t), \quad (7.34)$$

which takes the value 1 at node  $\mathbf{X}_i$  and zero at all other nodes, thus forming the ‘pyramid’ function shown in Figure 7.2. The set of functions,  $\phi_i$  has the property that they form a partition of unity

$$\sum_{i=1}^N \phi_i = 1. \quad (7.35)$$

To ensure this partition when a Dirichlet boundary condition is imposed, the mass is shifted to the interior nodes. This means the pyramid function is altered for elements connected to a Dirichlet boundary (for more details see [47]).

Choosing the basis functions in this way enables us to define a piecewise linear approximation of  $h(\mathbf{x})$  such that

$$h \approx H = \sum_{j=1}^N H_j \phi_j, \quad (7.36)$$

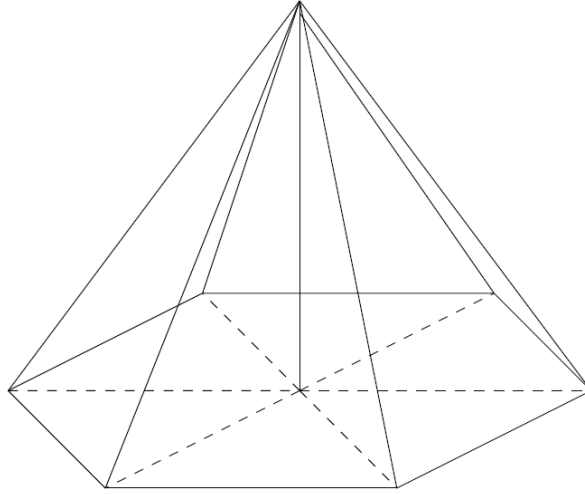


**Figure 7.2:** Two-dimensional linear finite element ‘pyramid’ basis function [109]

where  $H_j$  is the approximation to  $h$  at  $\mathbf{X}_j$ . Similarly  $M_j$  is the discrete approximation to  $m(\mathbf{X}_j)$  with

$$m \approx M = \sum_{j=1}^N M_j \phi_j. \quad (7.37)$$

The total mass  $\theta$  (Eq. (7.4)) can be approximated by substituting  $H$  for  $h$ , then summing over all the triangles which make up the domain. An approximation  $\Theta$  to  $\theta$  is then given using the two-dimensional equivalent of the trapezium rule,

$$\Theta = \frac{1}{3} \sum_{p=1}^P \mathcal{A}_p \left( \sum_{q=1}^3 H_{pq} \right) \quad (7.38)$$

where  $P$  is the number of triangles in the domain  $\Omega(t)$  and  $\mathcal{A}_p$  is the area of triangle  $p$ .  $H_{pq}$  is the approximation to the ice thickness at vertex  $q$  of triangle  $p$ .

Similarly we may approximate the differential of the total mass,  $\dot{\theta}$  (Eq. (7.9)), by

$$\dot{\Theta} = \frac{1}{3} \sum_{p=1}^P \mathcal{A}_p \left( \sum_{q=1}^3 M_{pq} \right) \quad (7.39)$$

where  $M_{pq}$  is the approximation to the ice equivalent accumulation rate at vertex  $q$  of triangle  $p$ .

With these approximations we can formulate a numerical expression to the relative mass fraction constants  $\mu_i$  (Eq. (7.17)). Using the basis function Eq. (7.34) and the

approximation of  $h$  from Eq. (7.36), the expression for  $\mu$  can be written

$$\mu = \frac{1}{\theta} \int_{\Omega(t)} w h d\mathbf{x} \quad (7.40)$$

$$= \frac{1}{\theta} \sum_{j=1}^N \left[ \int_{\Delta p} \phi_i \phi_j d\mathbf{x} \right] H_j \quad (7.41)$$

$$= \frac{1}{\theta} \mathcal{M} \mathbf{H} \quad (7.42)$$

where we introduce the matrix  $\mathcal{M}$ , the standard mass matrix for linear basis functions used in finite element methods with elements

$$\mathcal{M}_{ij} = \int_{\Delta p} \phi_i \phi_j d\mathbf{x}. \quad (7.43)$$

Using a similar approximation to that used for the ice thickness and the source term in Eqs. (7.36) and (7.37), respectively, we may approximate the velocity potential  $\psi$  by

$$\psi = \sum_{j=1}^N \psi_j \phi_j, \quad (7.44)$$

where  $\psi_j = \psi(\mathbf{X}_j)$ . The gradient of the velocity potential is therefore approximated by

$$\nabla \psi = \sum_{j=1}^N \psi_j \nabla \phi_j. \quad (7.45)$$

The initial ice thickness, accumulation term, total mass, mass fraction constants and velocity potential have now been approximated, which allow us to calculate the numerical estimations in Eq. (7.33) and thus find the net velocity. The algorithm for a single time step can be split into three stages.

### Stage 1

In the first stage we aim to approximate the net velocity, for which we require the velocity potential from Eq. (7.33).

Substituting the approximations Eqs. (7.32) and (7.45) into the equation for velocity potential, the left hand side of Eq. (7.33) can be written as

$$\int_{\Omega(t)} \nabla w \cdot (h \nabla \psi) d\mathbf{x} \approx \sum_j \left[ \int_{\Omega(t)} H_j \nabla \phi_i \cdot \nabla \phi_j d\mathbf{x} \right] \psi_j \quad (7.46)$$

$$= \mathcal{K}_h \psi \quad (7.47)$$

where  $\boldsymbol{\psi}$  is a vector with entries  $\psi_j$ .  $\mathcal{K}_h$  is the stiffness matrix used in finite element methods weighted by the ice thickness  $h$ . The elements of the weighted stiffness matrix are given by

$$(\mathcal{K}_h)_{ij} = \int_{\Delta p} H \nabla \phi_i \nabla \phi_j d\mathbf{x}. \quad (7.48)$$

The velocity potential  $\psi$  is then found by a solution of the approximation to Eq. (7.33)

$$\mathcal{K}_h \boldsymbol{\psi} = \mathcal{M} \mathbf{M} - \frac{\dot{\Theta}}{\Theta} \mathcal{M} \mathbf{H} + \mathbf{f} \quad (7.49)$$

using the approximations to  $h$ ,  $m$  and  $\mu$  from Eqs. (7.36), (7.37) and (7.42), with  $f_i = \int \phi_i \cdot (h\mathbf{u}) d\mathbf{x}$ .

Finally, to recover the net velocity  $\mathbf{v}$  we use an approximation to the weak form of Eqs. (7.32) and (7.45) to obtain

$$\sum_{j=1}^N \left[ \int_{\Delta p} \phi_i \phi_j d\mathbf{x} \right] V_j = \sum_{j=1}^N \left[ \int_{\Delta p} \phi_i \nabla \phi_j d\mathbf{x} \right] \psi_j, \quad (7.50)$$

$$\mathcal{M} \mathbf{V} = \sum_{j=1}^N \left[ \int_{\Delta p} \phi_i \nabla \phi_j d\mathbf{x} \right] \psi_j. \quad (7.51)$$

### Stage 2

In the second stage we use the calculated velocity  $\mathbf{V}$  to move the nodes of the mesh by the explicit Euler scheme:

$$\mathbf{X}^{k+1} = \mathbf{X}^k + \Delta t \mathbf{V}^k, \quad (7.52)$$

where  $k$  denotes the time discretisation level. Similarly, the total mass  $\Theta$  is also updated by an explicit Euler scheme using the approximated value of  $\dot{\theta}$  from Eq. (7.39),

$$\Theta^{k+1} = \Theta^k + \Delta t \dot{\Theta}. \quad (7.53)$$

The time step is again based upon the general rule for diffusion equations, as in Eq. (5.63).

### Stage 3

The final step is to recover the ice thickness at the new nodes. Rearranging Eq. (7.42) gives

$$\mathbf{H}^{k+1} = [\mathcal{M}^{-1} \Theta]^{k+1} \boldsymbol{\mu} \quad (7.54)$$

determines the ice thickness at the next time step while enforcing relative mass conservation.

## 7.4 Experiments

We now demonstrate the two-dimensional moving mesh method detailed in Section 7.3. As with the one-dimensional version of the method we begin with a test scenario to demonstrate the method, before again using the radially symmetric EISMINT scenario to compare the method with existing methods. Finally we will demonstrate domains that are not radially symmetric.

### 7.4.1 Testing the Model

For an initial test we shall use a circular domain centered at the origin  $(0, 0)$  with radius  $b(t)$  and an initial profile of the form:

$$h = (b(0)^2 - |\mathbf{x}|^2)^\alpha. \quad (7.55)$$

The parameter  $\alpha$  influences the profile and the diffusive velocity in a similar way to the analysis in Section 5.2.1. Initially the radius of the domain is given as  $b(0) = 1$ , where the boundary is entirely Dirichlet with the zero ice thickness condition given in Eq. (7.3). This means that the entire boundary is free to move. We choose a source term that is radially symmetric, i.e.

$$m = \gamma \left( 1 - \frac{|\mathbf{x}|^2}{\beta} \right) \quad (7.56)$$

where  $\beta$  determines the equilibrium line and  $\gamma$  is a parameter to control the scale. Using a radially symmetric domain and source term forces the model to behave evenly in all directions, which is ideal for testing the model. The source function is independent of time which means there exists a steady state solution. This may be found by using the radially adjusted version of the steady state solution, found in Eq. (5.82). It can be shown therefore that the steady state radius is given by

$$b_{ss} = \sqrt{2\beta}. \quad (7.57)$$

Using the parameters defined in Table 7.1 the two-dimensional numerical moving mesh model is tested on a *Strang* type mesh (see Section A.2) with 177 mesh nodes, as shown in Figure 7.3. We will now demonstrate the ability of the two-dimensional numerical model to simulate advance, retreat and an initially stationary front.

Physical Parameters	
$n = 3$	Flow-law exponent
$A = 10^{-16}(Pa)^{-3}a^{-1}$	Flow-law parameter
$g = 9.81ms^{-2}$	Acceleration due to gravity
$\rho = 910kgm^{-3}$	Ice density
$c = -2Ag^n\rho^n/(n + 2)$	Constant Parameter
$\gamma = 0.0005$	Scale of accumulation rate
Computational Data	
$N = 177$	Number of gridpoints
$\Delta t = 2a$	Time Step
$T$	Final Time

**Table 7.1:** Values used within the test scenario including physical parameters of the PDE and the data used in the computational domain.

**Glacier in Advance:**  $\alpha = 3/7$ ,  $\beta = 0.72$ ,  $T = 30000a$

We first set the equilibrium line parameter to  $\beta = 0.72$ , so that the steady state solution has a larger extent than the initial domain. We see in Figure 7.4 that the ice thickness builds up over time across the domain, primarily close to the centre where the accumulation term in Eq. (7.56) is greatest. The boundary of the domain increases symmetrically over time until the domain reaches steady state at  $b_{ss} = \sqrt{1.44}$  in Eq. (7.57). Note that in steady state there still exists a small amount of movement in the interior, but the effect on the ice thickness over the domain is negligible and crucially there is zero velocity on the boundary which means the domain is stationary.

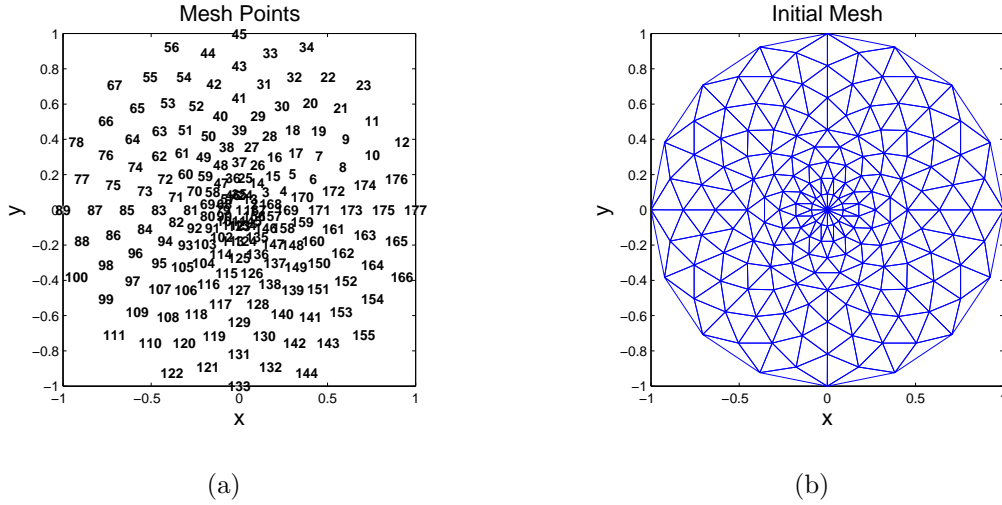


**Figure 7.3:** Initial nodal location and mesh, using the Strang method (see Section A.2) for the two-dimensional test scenario

**Glacier in Retreat:**  $\alpha = 3/7$ ,  $\beta = 0.32$ ,  $T = 10000a$

Now let us define the equilibrium line by  $\beta = 0.32$ , such that the extent of the steady state solution in Eq. (7.57) is inside the original domain. We observe in Figure 7.5 that the ice thickness still builds up in the center of the domain where the accumulation term is positive, only now the boundary retreats back to  $b_{ss} = \sqrt{0.64}$ . Due to the sharp gradient of the accumulation term (Eq. (7.56)) the simulation reaches the steady state solution quickly as this is the dominant term in the net velocity Eq. (7.31). Encouragingly, the numerical mesh nodes respond evenly in the domain, maintaining their connectivity and avoiding mesh tangling.

**Stationary Front:**  $\alpha = 1$ ,  $\beta = 1$ ,  $T = 2000a$

A final test of the model sets the equilibrium line by choosing  $\beta = 1$  so that the accumulation term is zero on the initial boundary. In addition, the initial profile Eq. (7.56) is set with  $\alpha = 1$  so the analysis in Section 5.2.1 is applicable and the flow velocity is initially zero on the boundary.

We see in Figure 7.6 that the net velocity remains zero around the boundary as a result of the choice of initial conditions, until the ice thickness profile builds up to meet the condition in Section 5.2.1, and the flow velocity can push the boundary forwards.

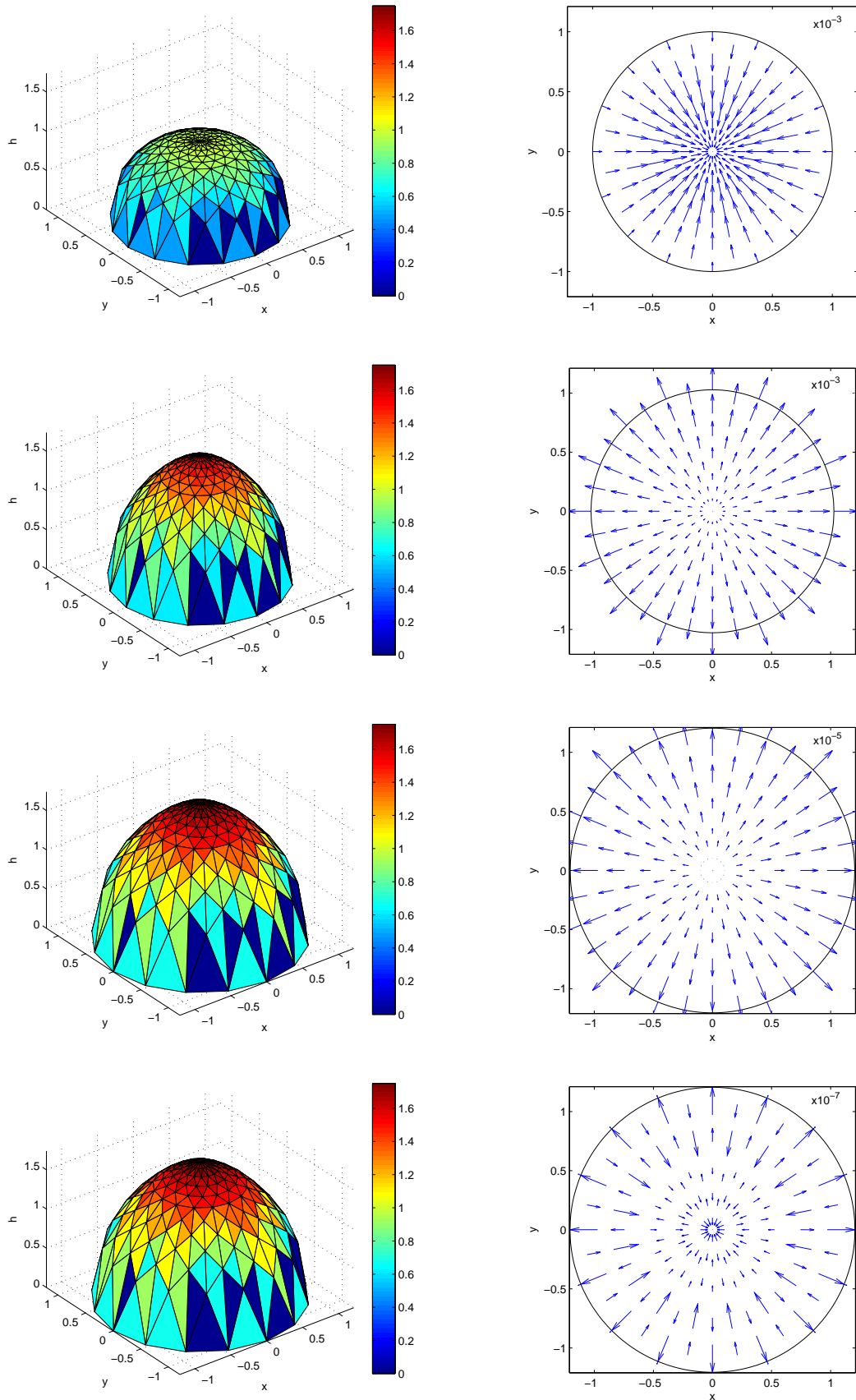


**Figure 7.4:** *Advancing Glacier: Ice Thickness Profile (left) and Net Velocity (right) at  $t = 0, 2000, 15000, 30000$  (in descending order) with  $\alpha = 3/7$  and  $\beta = 0.72$ .*

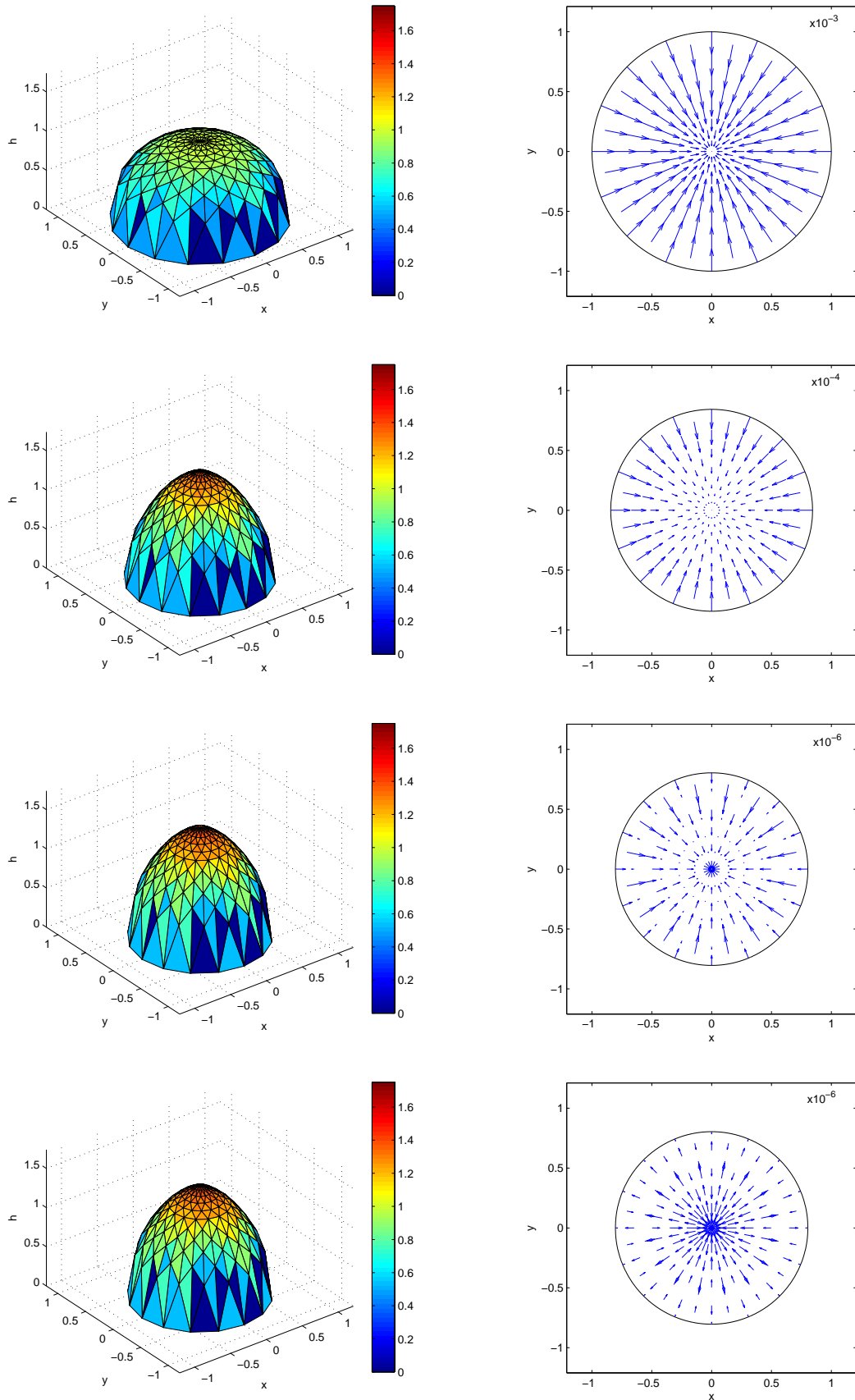


**Figure 7.5:** *Retreating Glacier: Ice Thickness Profile (left) and Net Velocity (right) at  $t = 0, 1000, 5000, 10000$  (in descending order) with  $\alpha = 3/7$  and  $\beta = 0.32$ .*

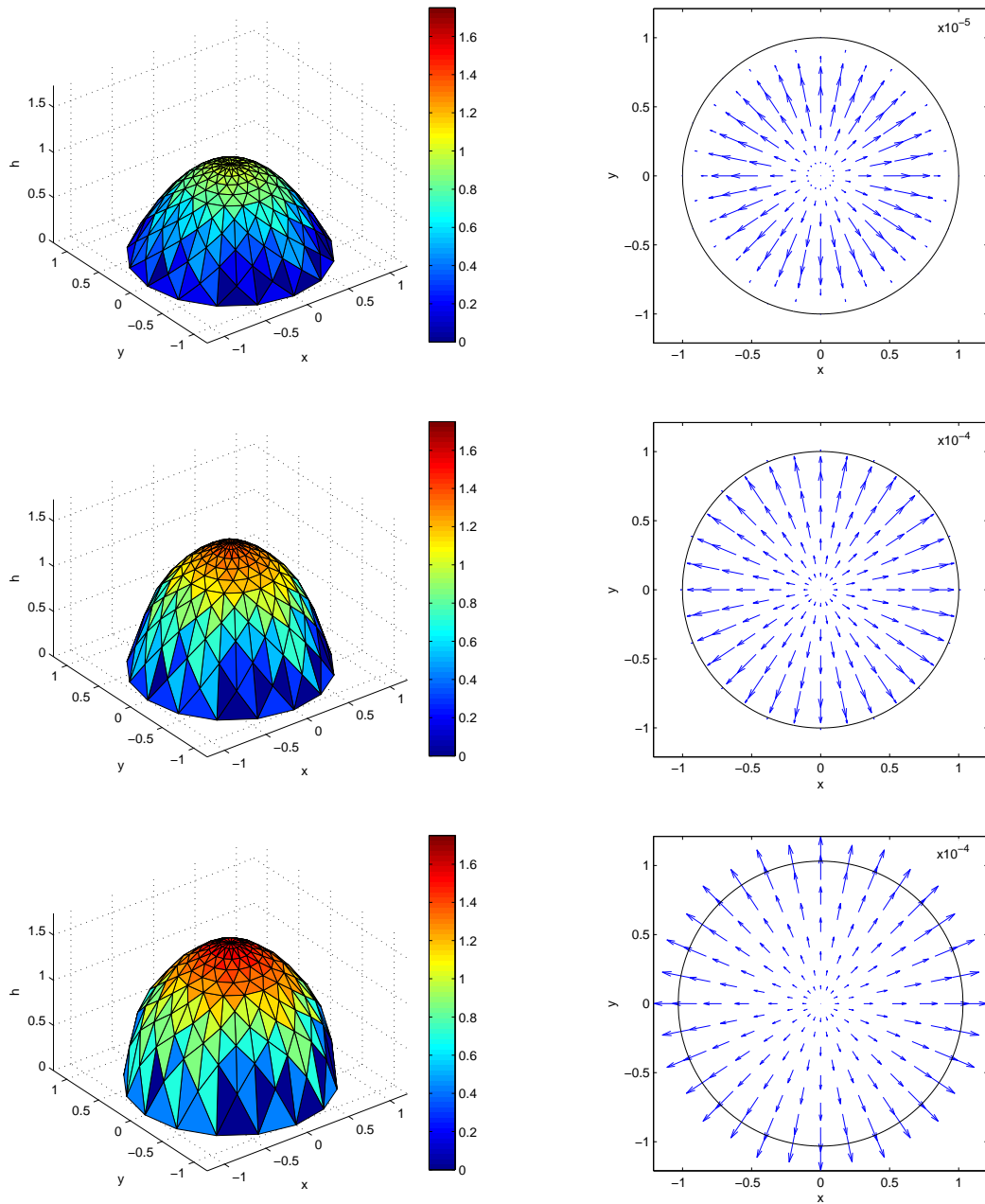


**Figure 7.6:** *Initially Stationary Glacier: Ice Thickness Profile (left) and Net Velocity (right) at  $t = 0, 1000, 2000$  (in descending order) with  $\alpha = 1$  and  $\beta = 1$ .*

### 7.4.2 European Ice Sheet Modelling INiTiative

We now compare the two-dimensional moving mesh model with the EISMINT equations encountered in Section 5.5.2. As before we replicate the radially symmetric moving margin experiment and compare the results with the fixed grid methods presented in [49].

The source term is given as a function of the distance from the origin,

$$m = \min\{0.5, \gamma(\beta - |\mathbf{x}|)\}, \quad (7.58)$$

with  $\beta = 4.5 \times 10^5 km$  determining the equilibrium and  $\gamma = 10^{-2} ma^{-1} km^{-1}$  the scaling factor. The experiment starts with zero ice thickness, and is evolved forward by one fixed grid Euler time step to get an initial profile for the ice thickness, whose distributed mass we will preserve under the two-dimensional weak form CMF method in Section 7.2.1. Therefore the initial ice thickness profile is

$$h^0 = \Delta t \times \min\{0.5, \gamma(\beta - |\mathbf{x}|)\}, \quad (7.59)$$

over a circular domain with radius  $\beta$ . The initial radius corresponds to the equilibrium line as ice has accumulated in this region. The steady state boundary is the same as in one dimension (Eq. (5.83)) which applies to the whole circumference of the domain:

$$b_{ss} = 579.81 km. \quad (7.60)$$

The physical parameters used in the experiment are given in Table 7.2 along with the numerical data. The initial mesh discretisation uses the *Strang* approach (see Section A.2) with 721 mesh nodes. The time step is taken to be  $2a$ , with the simulation running to a final time  $T = 30000a$ .

To assess the results of the moving mesh approach we directly compare the output with that of a fixed grid scenario discretised evenly on a  $31 \times 31$  square, a total of 961 grid points. We see in Figure 7.7 that the moving mesh approach resembles the circular

Value	Quantity
$n = 3$	Flow-law exponent
$A = 10^{-16} Pa^{-3} a^{-1}$	Flow-law parameter
$g = 9.81 m s^{-2}$	Acceleration due to gravity
$\rho = 910 kg m^{-3}$	Ice density
$m = \min\{0.5, \gamma(\beta -  \mathbf{x} )\}$	Ice equivalent accumulation/ablation
$\gamma = 10^{-2} m a^{-1} km^{-1}$	Slope of source function
$\beta = 4.5 \times 10^5 km$	Distance at which source function becomes negative

**Table 7.2:** *Two-dimensional EISMINT model parameters and functions.*

nature of the domain significantly better than the fixed grid method despite having 25% fewer grid points. The boundary is not perfectly circular due to the mesh representation, though the jagged edges are less prominent than in the fixed grid case. More specifically, the mesh points that do lie on the boundary provide a direct approximation to the location, without the need for interpolation.

Comparing both methods to the exact solution, we see in Table 7.3 that the moving mesh approach approximates the solution to the divide thickness to within 1%, while the error in the fixed grid method is twice as much. In particular the moving mesh adept at estimating the boundary position which it approximates to 0.14% of the exact location, whereas the fixed grid method has an error of 2.6%. When considering the scale is in kilometers this value is significantly higher.

However, the moving mesh method took approximately 4 times as long to run on a standard desktop than the fixed grid method, despite having fewer grid points. This could probably be reduced using more efficient coding techniques, though some speed is invariably lost due to the overheads in finite element methods.

### Choice of Initial Mesh

The initial mesh can potentially be important in achieving high levels of accuracy. To that end we introduce four different methods for generating a circular mesh, detailed

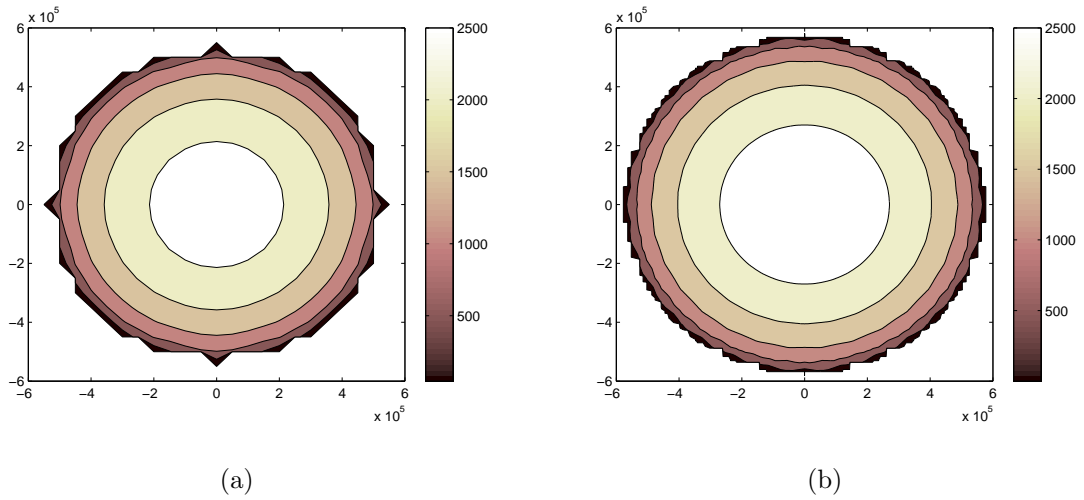


**Figure 7.7:** Steady state solution to the EISMINT scenario: a) A 2D fixed grid method, b) 2D Moving mesh model.

	Fixed Grid	Moving Mesh
Divide Thickness Error	1.96%	0.86%
Boundary Position Error	2.60%	0.14%
Computational Time	445s	2057s

**Table 7.3:** Error comparison of steady state results from Fixed Grid and Moving Mesh solutions to the 2D EISMINT problem.

in Appendix A, to use for comparison. By comparing different meshes we may identify common themes of the underlying method. We will apply the EISMINT scenario to each of these initial meshes, with approximately the same number of mesh nodes.

As expected the four meshes give comparable results (Figure 7.8) with only minor differences. The results from the *hex* mesh (Figure 7.8(c)) looks the most different from the others as this mesh has a large spatial gap between the boundary nodes and their connections to the interior, which results in long, thin triangular elements that skew the shading of the plot. As a consequence of having fewer mesh points near the boundary this mesh is the least accurate in resolving the boundary distance, as seen in Table 7.4.

A common theme for all the meshes is to overestimate the thickness at the divide.

This suggests that the flow velocity near the centre is slightly underestimated, as this acts to move ice towards the boundary.

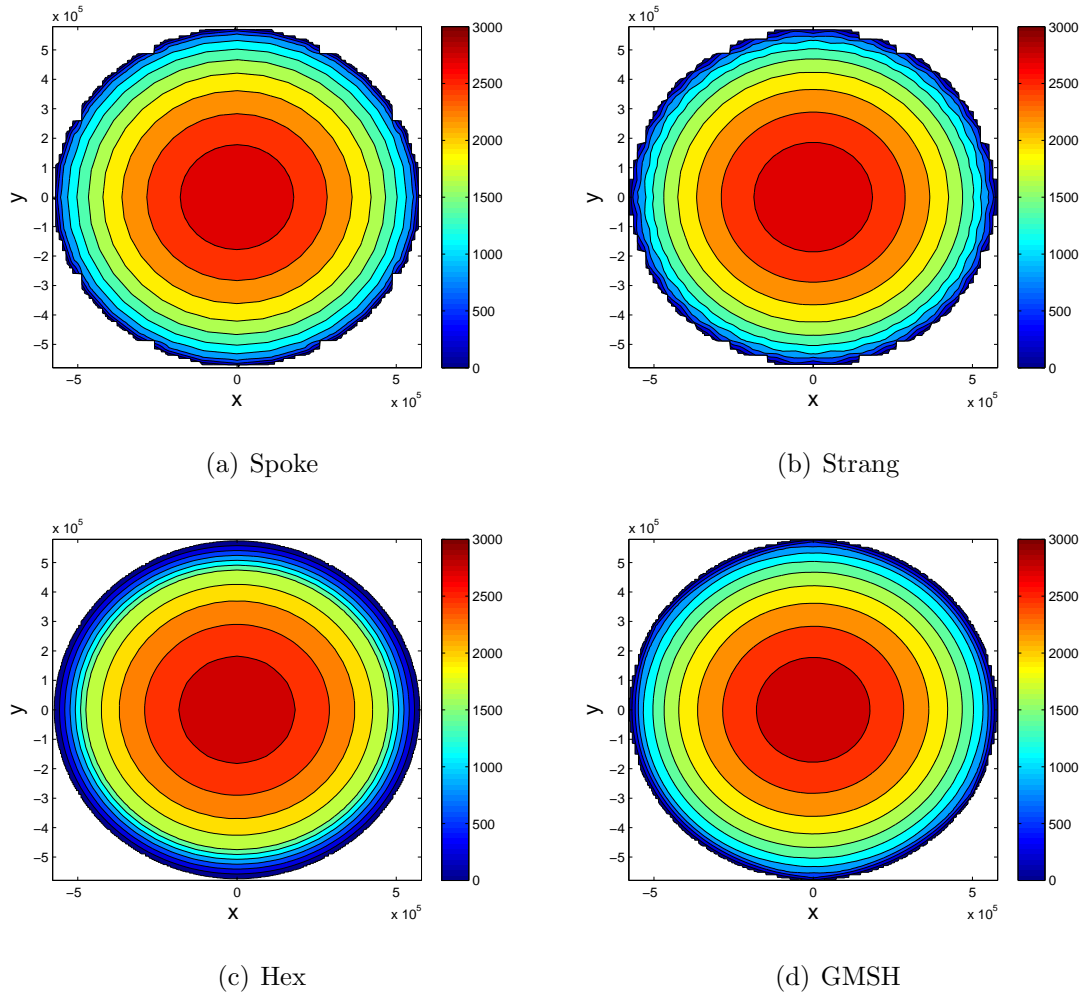


**Figure 7.8:** *Steady state ice thickness for the EISMINT problem using four different initial meshes.*

### Convergence

To test the performance of the numerical models we increase the resolution and assess convergence towards the exact solution. We check convergence for the *spoke* mesh (Appendix A.1) using the EISMINT data found in Table 7.2, while alternate initial meshes and inputs exhibited similar behaviour. As you can see in Figure 7.9, as the

Mesh	$N$	Boundary (km)	Divide Thickness (m)
Spoke	871	579.56	2986.2
Strang	721	580.62	2977.5
Hexagonal	763	573.76	3035.0
Gmsh	943	579.47	3004.3
Exact	-	579.814	2952

**Table 7.4:** Table of steady state values for the boundary and divide thickness in the EISMINT problem under four different initial meshes.

number of mesh points increase, the absolute difference between the approximation to the boundary and the exact location decreases exponentially. However the amount of computational time taken to achieve these results exhibits a linear increase which suggests there is an optimal trade off between the number of mesh points and the accuracy required. We can therefore say the the two-dimensional numerical CMF method is in this sense convergent.

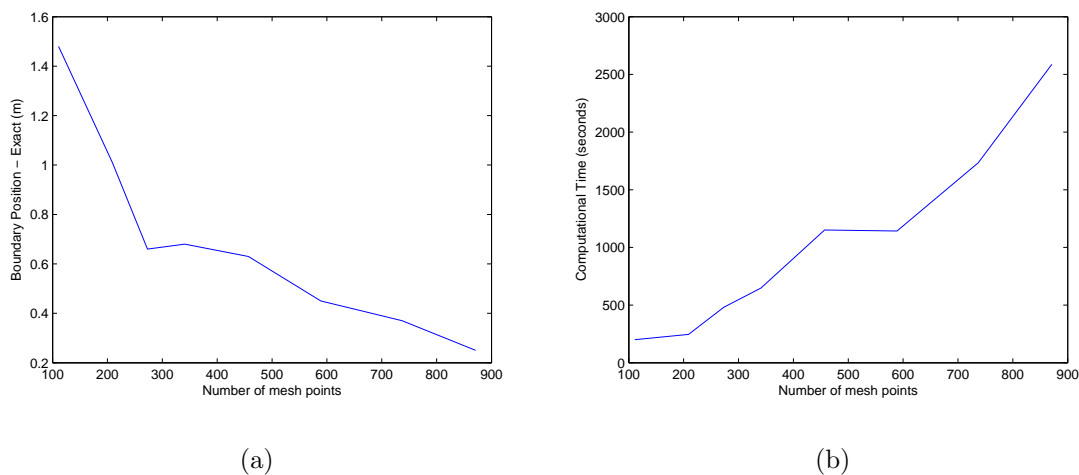


**Figure 7.9:** Convergence analysis for varying mesh nodes using the spoked initial mesh: a) absolute error in the boundary position, b) computational time.

## 7.5 Summary

In this chapter we began by looking at the shallow ice PDE in two horizontal spatial dimensions. We examined the evolution of the total mass of the domain and described the PDE in non-dimensional form with the requirements to maintain balance between the terms.

We then derived the weak formulation for the CMF approach in two dimensions which resulted in a net velocity described by the flow velocity and the ice accumulation. The weak formulation was then approximated numerically using a finite element method to gain the net velocity and a solution.

The numerical model was then tested against an example scenario that was circular in nature, with a zero Dirichlet condition for the ice thickness on the entire boundary. This demonstrated that the mesh is able to both advance and retreat whilst maintaining connectivity and avoiding mesh tangling. We provided a direct comparison between the moving mesh method and the fixed grid approach described in the EISMINT scenario, where the results showed a significant increase in accuracy but also in computational time.

Finally we showed the numerical method was convergent.

# Chapter 8

## Data Assimilation on Moving Meshes in 2D

In this chapter we apply the optimised 3D-VAR data assimilation scheme to the two-dimensional moving mesh model of the previous chapter to produce a statistically best estimate of the state of the ice. We describe the components of the scheme for this higher dimensional moving mesh application and highlight the differences with the one-dimensional case. We again use a *twin experiment* to test this approach and demonstrate the ability of the method to improve the prediction.

We then extend the scheme to incorporate the mesh into the state vector as we did in the one-dimensional case, highlighting potential restricting factors.

### 8.1 3D-VAR on a 2D Moving Domain

Increasing the numerical model to two horizontal dimensions produces a more accurate approximation to the ice thickness over the domain as we allow the ice to spread out in more directions. We now apply the 3D-VAR scheme to this moving mesh model to further improve the representation of the ice thickness. As in one-dimension the 2D numerical mesh is also evolving as part of the dynamical model, but this does not change the general form of the optimal 3D-VAR equation used before (Eq. (6.1)), given

by:

$$\mathbf{z}_k^a = \mathbf{z}_k^f + \mathbf{K}_k(\mathbf{y}_k - \mathbf{C}_k \mathbf{z}_k^f), \quad (8.1)$$

subject to the dynamical model

$$\mathbf{z}_k^f = \mathcal{M} \mathbf{z}_{k-1}^a, \quad (8.2)$$

where  $\mathbf{z}_k \in \mathbb{R}^q$  is a vector containing the unknown state variables at time  $t_k$ , where  $a$  is the optimal *analysis* solution, and  $f$  is the *forecast* from the dynamical model. The gain matrix  $\mathbf{K}_k$  is given by

$$\mathbf{K}_k = \mathbf{B}_k \mathbf{C}_k^T (\mathbf{C}_k \mathbf{B}_k \mathbf{C}_k^T + \mathbf{R}_k)^{-1}. \quad (8.3)$$

There are however, some changes to the observation operator  $\mathbf{C}_k$ , the observation error covariance matrix  $\mathbf{R}_k$  and the background error covariance matrix  $\mathbf{B}_k$  in the 2D application which we shall detail now.

### 8.1.1 Observation Operator

The observation operator maps the state vector to observational space so that it is directly comparable to the observations.

In one-dimension we defined the rows of the observation operator  $\mathbf{C}_k$  by using a simple linear interpolation technique to define an observation of ice thickness in terms of the two surrounding mesh points. In two-dimensions this is no longer possible. Instead we use the knowledge of the numerical solution which lies on a triangular mesh, for which we seek to interpolate an observation to the vertices of a surrounding triangle.

Consider a point  $P$  located at  $(x^*, y^*)$  sitting within a triangle with vertices  $ABC$  (see Figure 8.1). This point may be described in terms of the areal co-ordinates [26]  $L_A, L_B, L_C$ , for which

$$L_A = \frac{\mathcal{A}_{PBC}}{\mathcal{A}_{ABC}}, \quad (8.4)$$

$$L_B = \frac{\mathcal{A}_{PCA}}{\mathcal{A}_{ABC}}, \quad (8.5)$$

$$L_C = \frac{\mathcal{A}_{PAB}}{\mathcal{A}_{ABC}}, \quad (8.6)$$

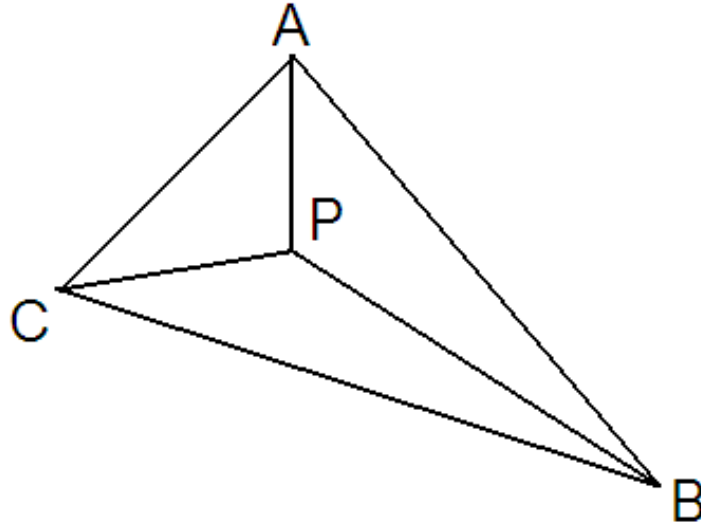


**Figure 8.1:** Point  $P$  lying within triangle  $ABC$  can be expressed in terms of its areal coordinates.

where  $\mathcal{A}_{ijk}$  represents the area of the triangle with vertices  $ijk$ . Since

$$L_A + L_B + L_C = 1 \quad (8.7)$$

these three co-ordinates provide a simple method of interpolation comparable with the linear interpolation used in one-dimension.

We now write the expressions for  $L_A, L_B$  and  $L_C$  in terms of the observation point  $P = (x^*, y^*)$ . First note that the area of triangle  $ABC$  with vertices  $(x_1, y_1), (x_2, y_2), (x_3, y_3)$  is given by

$$\mathcal{A}_{ABC} = \frac{1}{2} \begin{vmatrix} 1 & x_1 & y_1 \\ 1 & x_2 & y_2 \\ 1 & x_3 & y_3 \end{vmatrix}. \quad (8.8)$$

Equivalent expressions can be formulated for the three smaller triangles in Figure 8.1.

Therefore  $L_A$  can be written in the form

$$L_A = \frac{1}{2\mathcal{A}}(b_A + c_A x^* + d_A y^*), \quad (8.9)$$

with

$$b_A = \begin{vmatrix} x_2 & y_2 \\ x_3 & y_3 \end{vmatrix}, \quad c_A = \begin{vmatrix} y_2 & 1 \\ y_3 & 1 \end{vmatrix}, \quad d_A = \begin{vmatrix} 1 & x_2 \\ 1 & x_3 \end{vmatrix}. \quad (8.10)$$

Similar expressions for  $L_B$  and  $L_C$  can be formed with cyclic expressions of  $b_B, c_B, d_B, b_C, c_C$  and  $d_C$  to provide the interpolations values. The observation may then be written

$$h(x^*, y^*) = L_A h(x_1, y_1) + L_B h(x_2, y_2) + L_C h(x_3, y_3) \quad (8.11)$$

Therefore for every observation of ice thickness, the corresponding row  $j$  in  $\mathbf{C}$  contains the coefficients  $L_A, L_B$  and  $L_C$  located at  $C_{j,i}$ , where  $i$  represents the numbered location of the vertices  $A, B$  and  $C$  within the mesh structure. We assume that every observation lies within the numerical domain of the model.

### 8.1.2 Observation Error Covariance Matrix

The observation error covariance matrix  $\mathbf{R}_k$  represents the uncertainty in the errors in observations and is unaffected by the dimension of the system. As such this matrix can be written in the form

$$\mathbf{R}_k = \sigma_o^2 \mathbf{I}, \quad \mathbf{R}_k \in \mathbb{R}^{p \times p}, \quad (8.12)$$

under the assumption that each observation is independent of the others. The error variance for each observation is given by  $\sigma_o^2$ .

### 8.1.3 Background Error Covariance Matrix

The background error covariance matrix  $\mathbf{B}_k$  is a  $q \times q$  matrix representing the uncertainty in the errors in the prior state of the system.

The elements of the background error covariance matrix  $\mathbf{B}_k$  can be approximated using an analytic correlation function, which we choose to be a modified Gaussian function. This uses the distance between mesh points to form the elements of  $\mathbf{B}_k$ . For two-dimensions (and higher) this may be written as

$$b_{ij} = \sigma_b^2 \exp^{-L \|\mathbf{x}_i - \mathbf{x}_j\|^2}, \quad i, j = 1, \dots, N \quad (8.13)$$

where  $L$  is the inverse of a background correlation length scale and  $\sigma_b^2$  is the error variance associated with each ice thickness variable. The structure of this matrix de-

depends on the numbering system used when defining the numerical mesh and like the one-dimensional version, the function evolves to reflect this. The background error covariance matrix influences on the way information from observations is spread between the variables and by writing it in this form it implicitly depends upon the flow of the dynamical model.

### 8.1.4 Analysis Solution and Mass Conservation

Performing a step of an assimilation scheme alters the mass of the glacier using external information from observations of ice thickness. The CMF moving mesh method that we are applying this assimilation scheme to (see Section 7.2.1) is based on conserving relative mass, where the conservation principle (Eq. (7.17)) no longer holds after assimilating. The conservation principle

$$\frac{1}{\theta(t)} \int_{\Omega(t)} h d\mathbf{x} = \mu, \quad (8.14)$$

used to define the mesh deformation velocity and the ice thickness profile requires an analysis solution before the numerical model can continue.

Therefore at every assimilation cycle, after calculating the analysis solution to the ice thickness using Eq. (6.1), we recalculate the total mass  $\theta$  such that the analysis solution of the mass is

$$\theta^a(t) = \int_{\Omega(t)} h^a d\mathbf{x}, \quad (8.15)$$

and the mass fraction constants  $\mu$  are redefined as

$$\frac{1}{\theta^a(t)} \int_{\Omega(t)} wh^a d\mathbf{x} = \mu^a, \quad (8.16)$$

before the forecast step in the dynamical model. The analysis mass and equivalent mass fraction constants then correspond to the analysis estimation of the state variables.

In this work we calculate the analysis solution to the total mass and mass fraction constants at the end of each assimilation step.

### 8.1.5 3D-Var Algorithm for the CMF Moving Mesh Method

We now present the 3D-VAR algorithm for assimilating on a 2D moving domain using the weak form conservation of mass fractions method from Section 7.2.1.

1. Calculate a forecast of the state vector  $\mathbf{z}^f$  by evolving the numerical model of the CMF method (Section 7.3) using the previous analysis solution as model inputs. This gives forecast values of the numerical mesh  $(\mathbf{X}, \mathbf{Y})^f$ , the ice thickness  $\mathbf{H}^f$  and the total mass  $\theta^f$ . We also know the constant in time mass fractions  $\mu$ .
2. Use the optimal 3D-VAR formulation (Eq. (8.1)) to produce a new analysis solution of the ice thickness  $\mathbf{H}^a$  using observations available at the current time. The analysis solution to the numerical mesh is identical to the forecast, with  $\mathbf{X}^a = \mathbf{X}^f$ .
3. Calculate the analysis solution of the total mass  $\theta^a$  and update the mass fractions  $\mu^a$  using Eqs. (8.15) and (8.16).
4. Evolve the analysis solution using the dynamical model to produce a forecast at the next time step.
5. Repeat steps 2-4.

## 8.2 A Test Experiment

We now test the 2D data assimilation scheme with the components defined above using a test scenario. As there are no observations available we will use a *twin experiment*, as in the 1D method (Section 6.2). A reference solution is simulated by evolving the numerical model in Section 7.4.1 with exact initial conditions, from which we sample observations. We then define incorrect initial conditions for the forecast model which we will evolve and apply the data assimilation scheme to.

### 8.2.1 Initial Conditions

#### Reference Solution

To generate the observations for a *twin experiment* we first define the known set of exact initial conditions. Let the true initial ice thickness be the function

$$h = 1 - (x^2 + y^2), \quad x^2 + y^2 \leq 1. \quad (8.17)$$

The model is evolved using the finite element approximation described in Section 7.3, with  $\Delta t = 0.2a$  on a *Hexagonal*-type mesh (see Appendix A.3) with 187 mesh nodes. Both the reference and forecast models run until an end time  $T = 2000a$ , as we want to see the effects of including observations before the models reach a steady state solution. These initial conditions formulate the reference solution, which provide observations and the target solution.

#### Forecast Model

For our experiments we estimate the initial ice thickness by function

$$h = 1.2^2 - (x^2 + y^2), \quad x^2 + y^2 \leq 1.2. \quad (8.18)$$

where the estimate of the initial domain, in addition to the ice thickness profile, is different to the reference solution. The total mass will also be different, along with the mass fraction constants used in the moving mesh procedure. The time step is taken to be the same as the reference solution, and we again use a *Hexagonal*-type mesh with 187 mesh nodes.

### 8.2.2 Results

We include a set of 18 observations of ice thickness taken at  $t = 500$  and  $t = 1500$ , distributed randomly across the domain with random noise taken from a normal distribution  $\epsilon_o \sim N(0, \sigma_o^2)$  with  $\sigma_o^2 = 0.05$  to represent an error of 5%. The observation

noise is kept constant between each of the experiments. The background error variance in Eq. (8.13),  $\sigma_b^2$  is also set to 0.05.

We see in Figures 8.2 and 8.3 that the application of the 3D-VAR scheme to the two-dimensional moving mesh method provides improved results for an ice thickness profile, with an small improvement to the extent of the domain.

At the first assimilation time,  $t = 500$ , that there is a large difference between the forecast (Figure 8.2(a)) and reference (Figure 8.2(c)) thickness profiles. After the assimilation the analysis thickness profile (Figure 8.2(b)) more closely resembles the truth, particularly in the centre of the domain. When we examine the difference between the analysis and reference solutions, Figure 8.2(d), there is a notable ring relating to the largest difference that corresponds to the location of the boundary of the reference solution. This is because the shape and size of the analysis domain remains the same size as the forecast since we only update the ice thickness variables not the domain.

By the second assimilation time,  $t = 1500$ , we see the see the forecast domain (Figure 8.3(a)) is closer to the reference (Figure 8.3(c)), as the moving mesh method implicitly improves the estimate of the mesh as it evolves. A second assimilation step again improves the prediction of the ice thickness profile (Figure 8.3(b)), with a smaller difference between the reference and the analysis as seen in Figure 8.3(d) which again exhibits the largest difference where the reference boundary is located.

The evolution of one of the boundary nodes is shown in Figure 8.4 where we can directly observe this moving point being pulled towards the reference location after the first assimilation time despite no analysis correction to the boundary at that time. Interestingly, after the second assimilation time the boundary appears to be moving with the same speed as the reference boundary. This suggests that the ice thickness profile is similar enough to the reference solution to generate the correct mesh velocity, despite the domain being overestimated.

Similar results are achieved using the alternative initial meshes described in Appendix A, which have little effect on the overall impact of the observations shown already. Additionally, experiments exploring the impact of observation quantity and distribution consistently improve the overall accuracy of the scheme. For instance, in-

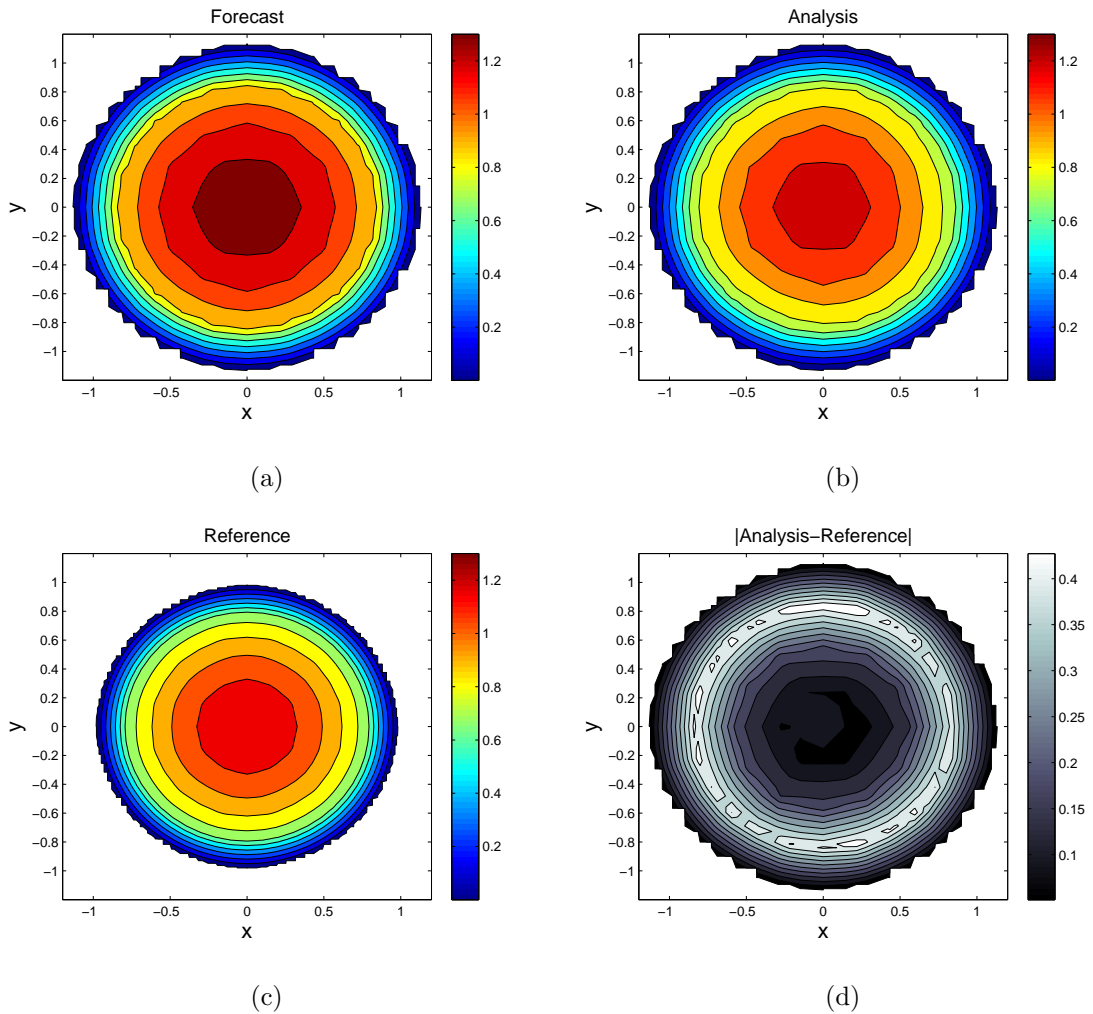


**Figure 8.2:** 2D moving mesh with data assimilation at  $t = 500$ :- a) Forecast before assimilation, b) Analysis solution, c) Reference solution and d) Difference between analysis and reference.

cluding observations all on one side of the domain instead of distributed randomly does not significantly impact the symmetry in the dynamical model.

Observations that lie within elements connected to the boundary nodes occasionally caused spurious results, which are believed to be due to the steep gradients along with the enforcement of Dirichlet boundary conditions.

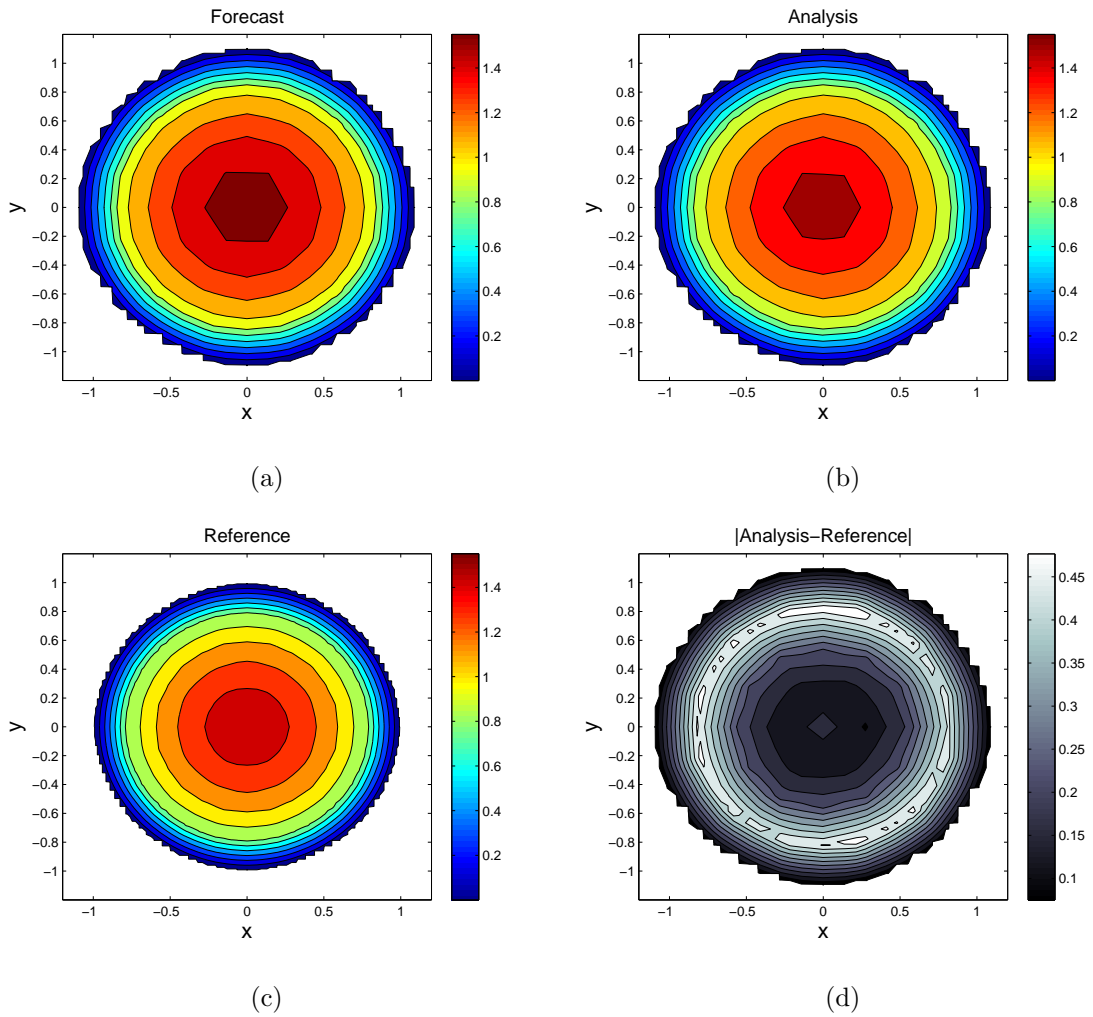


**Figure 8.3:** 2D moving mesh with data assimilation at  $t = 1500$ :- a) Forecast before assimilation, b) Analysis solution, c) Reference solution and d) Difference between analysis and reference.

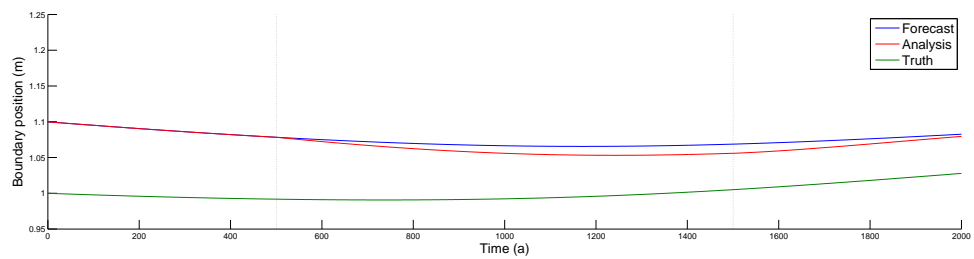


**Figure 8.4:** 2D moving mesh with data assimilation:- Evolution of a boundary point over time- Forecast (blue), Reference (Green), Analysis (Red).

### 8.3 2D Extended Scheme: Assimilating the Mesh - Theory

In Section 6.3 we built an extension to the one-dimensional 3D-Var scheme to incorporate the mesh explicitly into the state vector to calculate an analysis solution to the numerical domain. This was successfully implemented and it was demonstrated that the prediction of the domain at the time of assimilation was improved. We now seek a similar extension in higher spatial dimensions.

Generally, positional features in higher dimensions are observed in the form of a line, such as the boundary of the domain or geological evidence such as moraines for glaciers. The interpolation of this to a numerical mesh requires a discretisation of the line into points that may be related to the mesh via the operator  $\mathbf{C}_k$ .

The definition of this operator, and the error covariance matrices  $\mathbf{R}_k$  and  $\mathbf{B}_k$  is not as straightforward in higher dimensions, since each co-ordinate is now a vector. We present two options for solving the problem in 2D:

#### 8.3.1 Option 1: Conjoined Co-ordinates

The first option joins the two co-ordinates together to form a single entity,  $\mathbf{d}_i = \|\mathbf{x}_i\|$ , such that the state vector is

$$\mathbf{z}_e = \begin{pmatrix} \mathbf{d} \\ \mathbf{h} \end{pmatrix}. \quad (8.19)$$

By combining the co-ordinates in this way, we essentially reduce the problem to 1D and can define the other components in the data assimilation scheme in a similar way to Section 6.3. The extended observation operator to map the state vector  $\mathbf{z}_e$  to the observations can be written as

$$\mathbf{C}_e = \begin{pmatrix} \mathbf{C}_d & \mathbf{0} \\ \mathbf{0} & \mathbf{C} \end{pmatrix}, \quad (8.20)$$

where  $\mathbf{C}_d$  is a simple interpolation matrix mapping observations of positional locations (e.g. the moving boundary) to the equivalent numerical mesh points.

The extended observation error covariance matrix, assuming observations are independent is

$$\mathbf{R}_e = \begin{pmatrix} \sigma_{od}^2 \mathbf{I} & \mathbf{0} \\ \mathbf{0} & \mathbf{R} \end{pmatrix} \quad (8.21)$$

where  $\sigma_{od}^2$  represents the error variances relating to observations of positional features.

Lastly, the background error covariance matrix can be written in the form

$$\mathbf{B}_e = \begin{pmatrix} \mathbf{B}_{dd} & \mathbf{B}_{dh} \\ (\mathbf{B}_{dh})^T & \mathbf{B} \end{pmatrix}, \quad (8.22)$$

where  $\mathbf{B}_{dd}$  is the error covariance matrix corresponding to the numerical mesh. As in one-dimension this can be defined using the modified Gaussian function from Eq. (8.13) as a correlation function. The cross-covariances  $\mathbf{B}_{dh}$  may then also be determined using the boundary points as was done successfully in one-dimension. This approach means the matrix  $\mathbf{B}_e \in \mathbb{R}^{2N \times 2N}$  is straightforward to calculate and suffers from no increase in size over the one-dimensional method.

With this option the analysis step, Eq. (8.1), is no more difficult than the one-dimensional method. However, by treating the coordinate pair as a single item, some post-assimilation technique is required to distinguish between the  $x$  and  $y$  elements.

### 8.3.2 Option 2: Separate Co-ordinates

An alternative option separates the co-ordinate pairs and treats them as separate variables, such that the state vector is defined by

$$\mathbf{z}_e = \begin{pmatrix} \mathbf{x} \\ \mathbf{y} \\ \mathbf{h} \end{pmatrix}, \quad (8.23)$$

with  $\mathbf{x}$  and  $\mathbf{y}$  representing the sets of  $x$  and  $y$  co-ordinates respectively. The components of the data assimilation algorithm can then be determined as follows.

By separating the variables any observations of positional features, which contain information in the form of a co-ordinate pair  $(x^*, y^*)$ , will also be separated. The

extended observation operator to map the state vector to these observations will be of the form:

$$\mathbf{C}_e = \begin{pmatrix} \mathbf{C}_x & \mathbf{0} & \mathbf{0} \\ \mathbf{0} & \mathbf{C}_y & \mathbf{0} \\ \mathbf{0} & \mathbf{0} & \mathbf{C} \end{pmatrix}, \quad (8.24)$$

where  $\mathbf{C}_x$  interpolates the  $x$  co-ordinates in the state vector to the observation location  $x^*$  and  $\mathbf{C}_y$  interpolates the  $y$  co-ordinates to  $y^*$ . These matrices need to account for the net distance between the observation and the mesh points rather than treating the co-ordinates completely separate since, for example, locations that are close together in the  $x$ -direction could be far apart in the  $y$ -direction.

Assuming that errors in observations are independent of each other, the extended observation error covariance matrix may be written in the form

$$\mathbf{R}_e = \begin{pmatrix} \mathbf{0} & \mathbf{0} & \mathbf{R} \\ \sigma_{ox}^2 \mathbf{I} & \mathbf{0} & \mathbf{0} \\ \mathbf{0} & \sigma_{oy}^2 \mathbf{I} & \mathbf{0} \end{pmatrix} \quad (8.25)$$

where  $\sigma_{ox}^2$  and  $\sigma_{oy}^2$  represent the error variances relating to observations of positional features in the  $x$  and  $y$  cartesian directions. We assume that the error variances are the same,  $\sigma_{ox}^2 = \sigma_{oy}^2$ . The assumption that errors in the observations of positional features are independent is debatable since we are observing a co-ordinate pair.

Finally, the extended background error covariance matrix for the error covariances in the forecast can be written as

$$\mathbf{B}_e = \begin{pmatrix} \mathbf{B}_{xx} & \mathbf{B}_{xy} & \mathbf{B}_{xh} \\ (\mathbf{B}_{xy})^T & \mathbf{B}_{yy} & \mathbf{B}_{yh} \\ (\mathbf{B}_{xh})^T & (\mathbf{B}_{yh})^T & \mathbf{B} \end{pmatrix} \quad (8.26)$$

where  $\mathbf{B}_{xx}$  and  $\mathbf{B}_{yy}$  are the error covariance matrices for the forecast of the  $x$  and  $y$  co-ordinates, while  $\mathbf{B}_{xy}$ ,  $\mathbf{B}_{xh}$  and  $\mathbf{B}_{yh}$  are the cross-covariance matrices between the co-ordinates and the ice thickness.

Defining  $\mathbf{B}_{xx}$ ,  $\mathbf{B}_{xy}$ ,  $\mathbf{B}_{xh}$ ,  $\mathbf{B}_{yy}$ ,  $\mathbf{B}_{yh}$  and  $\mathbf{B}$  is certainly a grey area. As previously mentioned the co-ordinates cannot be treated completely separately as the net distance between mesh points needs to be considered.

### 8.3.3 Discussion

Option 1 joined the co-ordinates together into a single unit, which reduces the problem to one-dimension and makes it easier to define and calculate. In doing so we require a method to distribute the analysis solution back to the individual  $x$  and  $y$  components.

Option 2 splits the co-ordinate pairs into separate entities, which maintains the full description of all the variables but is more difficult to define. The construction of the components in the data assimilation scheme still needs consider the distance between mesh points when calculating the observation operator mapping and the error covariances.

In essence, both methods appear to have significant drawbacks but until they have been tested we cannot determine which approach, if either, provides an viable analysis solution to the numerical mesh.

## 8.4 Summary

In this chapter we presented an application of the 3D-VAR data assimilation scheme to a two-dimensional moving mesh environment. An analysis solution of the total and relative mass values was required to ensure compatibility with the chosen method of mesh movement. Results demonstrated a successful application of the scheme with improved predictions of the ice thickness profile.

We then attempted to extend the scheme to include the mesh within the state vector and allow the potential for observations of positional co-ordinates to be included, using a similar approach to the extension in one-dimension. However, since the mesh nodes are described in coordinate pairs this proved significantly more difficult. A couple of potential solutions was proposed, neither of which is ideal. This remains an open ended problem.

# Chapter 9

## Conclusions

Accurate, efficient numerical modelling of the dynamical flow of glaciers is vital to simulating and forecasting the Cryosphere, which in turn has an impact on the atmosphere and oceans of our planet. Using adaptive mesh techniques improve efficiency by reducing the need for numerical domains with high resolutions and in particular moving meshes adapt the mesh by relocating mesh points to areas that require higher resolution. These numerical models can make use of the global observation network to produce a statistically best representation of glaciers using data assimilation.

In this thesis we sought to apply both a moving mesh method and data assimilation to the shallow ice model used to simulate glacier flow. We now summarise the work undertaken in this thesis before drawing conclusions and discussing ideas for future research.

### 9.1 Summary

In the introduction we set out the objectives of this thesis. They were:

- Develop a moving mesh method to equations governing dynamical ice flow.
- Use data assimilation to combine observations with a moving mesh model of dynamical ice flow.

With the specific aims of:

- Applying the CMF moving mesh method of Baines, Hubbard and Jimack [8] to the one-dimensional shallow ice approximation equation used within glaciology.
- Analysing the impact of internal glacier flow on the movement of the ice boundary.
- Using a sequential 3D-Var data assimilation scheme in conjunction with the moving mesh to improve the predicted ice profile.
- Building an extended scheme capable of including observations of positional features within the data assimilation method to improve the representation of the domain.
- Extending the moving mesh method and the 3D-Var scheme to two horizontal dimensions and demonstrate the difficulties encountered when considering this more complex scenario.

In the introduction we discussed elements of Glaciology and the reasons for being interested in ice dynamics. We continued this in Chapter 2 by introducing some of the terminology used in the field and the key driving forces behind ice flow. A brief discussion of the types of models used to simulate this flow was given, with particular focus on the shallow ice equations.

Chapter 3 introduced the idea of numerical models as a solution to time dependent PDEs, focusing on adaptive mesh models. We discussed the different methods of adaptivity, with the benefits of each method for ice flow models presented. A detailed description of a particular moving mesh method [8] was provided, based upon the idea of conserving relative mass. We then provided an brief history of the use of adaptive mesh methods within the field of glaciology.

In chapter 4 we introduced the idea and objectives of data assimilation, with an overview of some of these methods. Both sequential and variational schemes were

introduced, with details of the various components that are required to apply data assimilation techniques. We then examined the past attempts at applying data assimilation to both dynamical ice sheet models and adaptive mesh methods.

We began chapter 5 by examining the one-dimensional shallow ice equation in more detail. In particular we evaluated the effect of internal diffusive flow on the movement at the boundary. This provided a criterion upon the local ice profile that allows the boundary to move in the absence of any external forcing. We introduced a method for calculating a steady state solution when the forcing term is independent of time. We proceeded to apply the relative mass conservation method to the shallow ice equation, relating the resulting expression for mesh movement back to the analysis of boundary movement. A finite difference approximation to this moving mesh method was developed and tested using a series of simple test equations. We also extended the method to allow for radially symmetric problems and compared the method to the circular EIS-MINT moving margin experiment.

Chapter 6 detailed the application of the 3D-Var data assimilation scheme to the 1D moving mesh method of the previous chapter. We examined the changes to the components that make up the data assimilation scheme for a moving mesh method and described the analysis update of the total mass and the relative mass constants that were required in order to apply the assimilation scheme to our method. We then tested this method using a twin experiment applied to the test equations introduced in the previous chapter. We made an extension to the data assimilation scheme to include the mesh within the state vector and allow observations of positional features to be included. The impact on the components was assessed, in particular the background error covariance matrix with a proposed definition of the cross covariances between the mesh and the ice thickness variables. We carried out experiments to demonstrate the impact of including observations of the boundary and cross covariance terms, both separately and simultaneously.

In chapter 7 we extended the shallow ice equation to two horizontal dimensions, and detailed a non-dimensional version of the equations. The moving mesh method was then described in a weak formulation, from which we extracted the expression for the mesh velocity. A finite element approximation to the moving mesh method was applied and tested using a set of test scenarios similar to those used in one-dimension. We then compared the method to the EISMINT moving margin experiment and assessed the impact of using different initial meshes.

Lastly, in chapter 8 we applied the 3D-Var scheme to the 2D moving mesh model and detailed changes to the components of the scheme when an additional horizontal dimension is included. We used a twin experiment to test the scheme against the test equations and the EISMINT scenario. Finally we attempted to apply an extension to the scheme to include the mesh in the state vector and detailed the difficulties encountered.

## 9.2 Conclusions

In conclusion, we have shown that moving mesh methods accurately simulate the dynamical flow of glaciers and can achieve greater accuracy than conventional fixed grid approaches for, in 1D at least, minimal computational cost. A 3D-VAR Data assimilation method can be applied to moving mesh methods after adjusting the components of the scheme and can, in 1D at least, be extended to incorporate the numerical mesh within the analysis update.

Specifically, we conclude that

- The CMF moving mesh method of Baines, Hubbard and Jimack [8] is an effective tool for simulating the dynamical flow of a one-dimensional shallow ice flowline model.

We demonstrated in chapter 5 that the moving mesh approach can effectively simulate various aspects of dynamical ice flow in one-dimension. This method uses a combination of the diffusive velocity and the ice equivalent accumulation rate to adapt the mesh and accurately simulate changes in the domain. Results show that when using the same number of grid points, the solution to the EISMINT moving margin experiment, especially the location of the boundary, is significantly closer to the true solution for a negligible computational cost.

- Internal glacier flow impacts the movement of the ice boundary when the local profile has an asymptotically infinite gradient.

In Section 5.2.1 we assessed the diffusive flow velocity by rewriting the equation in a different form. This led to a condition on the local ice thickness profile that needed to be met to induce a finite flow at the boundary, corresponding to an infinite gradient. The underlying topography, ice density and temperature had no impact on this condition. This was supported by experiments with a zero source term at the initial boundary.

- A sequential 3D-Var data assimilation scheme can be used in conjunction with the moving mesh to improve the accuracy of the predicted ice profile.

In chapter 6 we demonstrated that with little configuration a 3D-Var scheme is readily applicable to the moving mesh scenario. An analysis update of the total mass and the relative mass constants was required for this particular moving mesh scheme to be compatible with the data assimilation. A modified Gaussian function was used to form the background error covariance matrix, which gave an improved representation of the evolving mesh that was previously unchanged when assimilating. Results showed that by observing the ice thickness the profile is improved, which with future iterations of the numerical model also reduces the errors in the domain.

- An extended scheme allows an analysis solution to the mesh at the time of assimilation.

By explicitly including the mesh into the state vector in Section 6.3, we were able to calculate an analysis solution of the numerical mesh. This was achieved in two ways; firstly by allowing observations of physical points such as the boundary and secondly by defining the cross-covariance terms in the background error covariance matrix to pass information between the mesh and the ice thickness variables. The experiments show that including one or both of these results in an improvement to the prediction of the numerical domain in addition to the ice thickness profile at the moment of assimilation.

- The moving mesh method readily extends to two horizontal dimensions.

We showed in chapter 7 that rewriting the moving mesh method in a weak formulation allows us to use finite elements to approximate the solution to the shallow ice equation in two-dimensions. Experiments demonstrate the ability of the method to replicate the different types of movement. Comparisons with the EIS-MINT moving margin scenario show that using  $\frac{2}{3}$ rd's the number of mesh nodes as a fixed grid method achieves a significant reduction in error, particularly the approximation to the location of the boundary. The choice of initial mesh demonstrated small variability in the steady state solution achieved.

- The sequential 3D-Var scheme applied to the moving mesh method extends to two horizontal dimensions.

In chapter 8 we demonstrated that the 3D-Var scheme can be applied to the moving mesh method in two-dimensions with a few modifications to the schemes components. An analysis update of the total mass and the relative mass constants was required for compatibility. Results indicated an improvement in the

prediction of the ice profile, with the error in the domain representation reducing implicitly with iterations of the numerical model.

- Extending the 3D-Var scheme to achieve an analysis solution of the mesh presents many difficulties in two-dimensions.

Two options for explicitly including the numerical mesh in the data assimilation scheme in 2D were proposed, with their advantages and disadvantages discussed. The effectiveness of both options is yet to be tested.

### 9.3 Future Work

In this work we have used the shallow ice approximation which defines an explicit equation to represent the diffusive flow velocity, where the resistance is solely at the bed of the glacier. In other scenarios different resistive stresses become important. For instance, in ice streams the resistance at the edge of the moving ice is more important than the base, while in problems that involve an ice shelf the back stress is most critical. In theory any time-independent function to describe the flow velocity can readily be included within the moving mesh solution to the mass continuity PDE (Section 5.3.1), which means the moving mesh procedure is not restricted to the shallow ice approximation. However, solving the function for diffusive flow is a separate issue independent of the moving mesh.

In our experiments we neglected the influence of temperature and density by including them as constant parameters in the model. Temperature can be incorporated by solving a thermodynamic equation, which in turn influences the flow law parameter  $A$  in Eq. (2.3). Including variable density is a different issue, as the main changes occur with depth. Potentially, a multilayered model could be a solution which would also allow an element of flow in vertical directions; however, the form of the mass continuity equation would change. A multilayered moving mesh solution would need careful defi-

dition around the boundary layer, but would open up a whole new area of development.

There are other scenarios in glaciology that are of particular interest, most notably the issue of finding the grounding line which separates grounded ice from floating ice shelves. With a moving mesh model we could fix a mesh node to the grounding line itself which would enable us to track its movements rather than interpolating to find its location. Additionally, if we were able to observe the grounding line the extended data assimilation scheme (Section 6.3) would be ideal for including this observation.

The glacier bed has been assumed to be flat throughout this thesis, except in the analysis of the diffusive velocity at the boundary (Section 5.2.1). The choice of bed will have an effect on the diffusive flow, particularly in areas where the gradient of the bed is positive. In addition more complex models aim to include the basal sliding that glaciers exhibit when there is water present at the base. Furthermore, over long time scales the effect of isostasy will influence the shape of the bed. The inclusion of the glacier bed opens up the possibility to apply the moving mesh method to a real-life scenario, which provides the opportunity to fully assess the feasibility of the method to accurately simulate dynamical flow.

In our data assimilation model the biggest limitation involved assuming all observations occur within the computational domain. The next logical step would be to devise a method for incorporating observations from outside the domain, ideally into the extended scheme so that the numerical mesh is corrected given this new information. The next step for the extended scheme is to find an effective way of applying the method to higher dimensions, either by developing the ideas mentioned in Section 8.3 or devising an alternative method.

When the model has been applied to a real-life scenario, actual observations can be included into the data assimilation scheme to further test the abilities of both the

original and extended schemes to improve the estimate of the ice thickness profile and numerical domain. Including observations of the diffusive flow (at the surface) opens up the possibility of rewriting the problem by expressing the state vector in terms of this flow instead of the ice thickness. There could then be two applications of a data assimilation scheme at each time step; once to gain an analysis estimation of the diffusive flow before the mesh is moved and once after to update the ice thickness (and domain if positional observations are available).

Long term, applying an ensemble data assimilation scheme (see e.g. [32]) to the moving mesh environment is a key objective. These methods use an ensemble of perturbed initial conditions, forecast with the dynamical model to estimate the errors in the model and generate the optimal forecast. In a moving mesh method the ensemble approach would provide the best possible estimate of the numerical domain.

# Appendices

# Appendix A

## Circular Mesh Generation

There are many ways to discretise a domain. Here we show four methods for discretising a circular shaped domain around the origin.

### A.1 Spoke

One of the most straightforward circular meshes is a spoked mesh, with the nodes lying along straight lines extending from the centre. like a bike wheel. Two parameters are used to determine the number of grid points; the number of points on each spoke and the number of spokes themselves. If we define the number of spokes in terms of the angle between them, this gives a set of polar co-ordinates with which to generate the mesh.

Whilst simple to calculate, as you can see in Figure A.1 the nodes are concentrated close to the centre and spread out around the boundary. This would be better suited to a problem where the centre requires more information, as opposed to the ice sheet problem where the boundary requires a finer mesh.

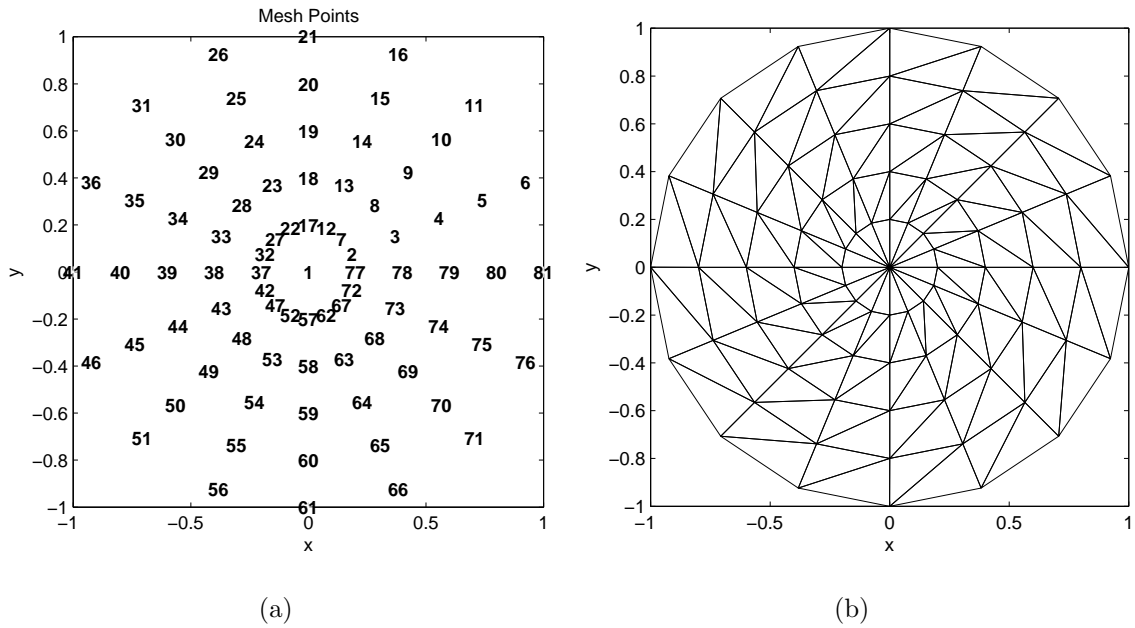


**Figure A.1:** An example of a mesh generated using spokes protruding from the centre, with 5 nodes per spoke and the angle between them  $\pi/8$ .

## A.2 Strang

An alternative mesh is the one proposed by Strang [98]. Here the nodes are placed using a combination of spokes and circles. The nodes still lie on the spokes however for each circle there is only a node on every other spoke. The next circle out then places a node on remaining spokes and then the process is repeated. The number of circles and the number of nodes lying on each circle then define the mesh.

This mesh is relatively simple to produce and around the centre there is a smaller cluster of nodes than the spoke mesh. However there are still large connections between nodes near the boundary and long thin triangles are produced from the calculation (see Figure A.2). This effect is reduced by including more nodes.

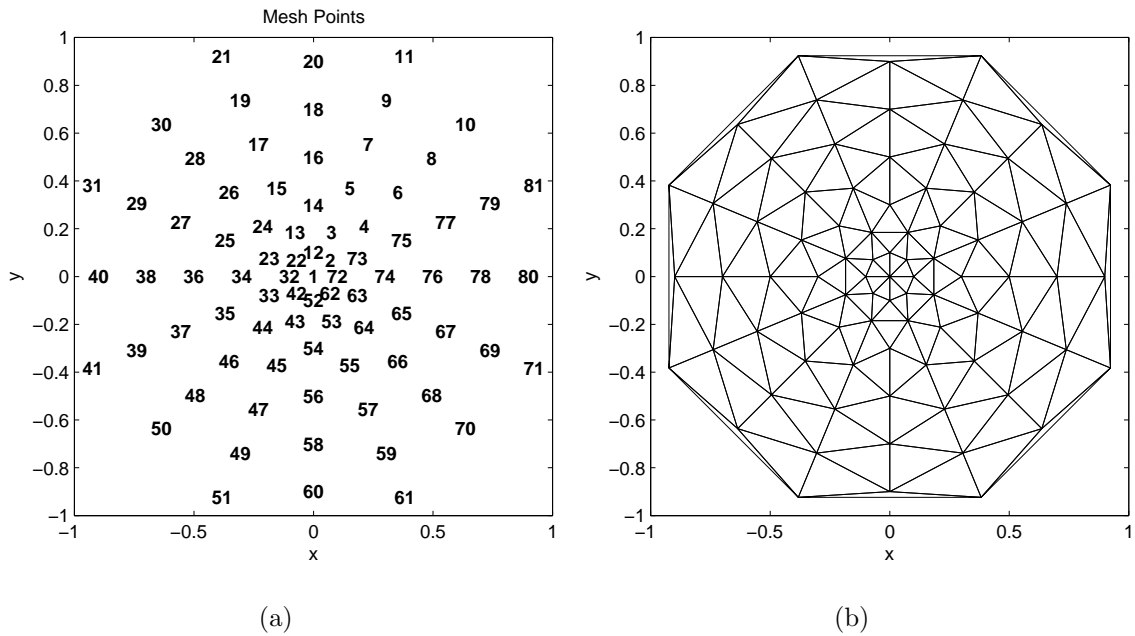


**Figure A.2:** A mesh generated using the Strang approach with 10 circles and 8 nodes per circle. At low resolution this mesh loses information close to the boundary and has a lot of long thin triangles which can cause numerical problems due to the shallow angle.

### A.3 Hexagonal

Looking closely at Figure A.1(a) and Figure A.2(a) shows that these two methods of mesh generation can lead to nodes with varying amounts of connections. With the exception of the boundary, it can be beneficial to have an equal number of connections to improve the structure of the matrices in the finite element method Section 7.3. With this in mind we construct a mesh where the elements are hexagonal in shape with six connections into each node. To achieve this we again define how many circles we require, however this time for each circle we double the number of nodes each time as we move away from the centre, starting from six. The nodes are then distributed evenly around the circle.

As we observe in Figure A.3 the interior nodes now contain six connections and there is a greater number of nodes near the boundary to provide more detail, but this introduces long thin triangles.

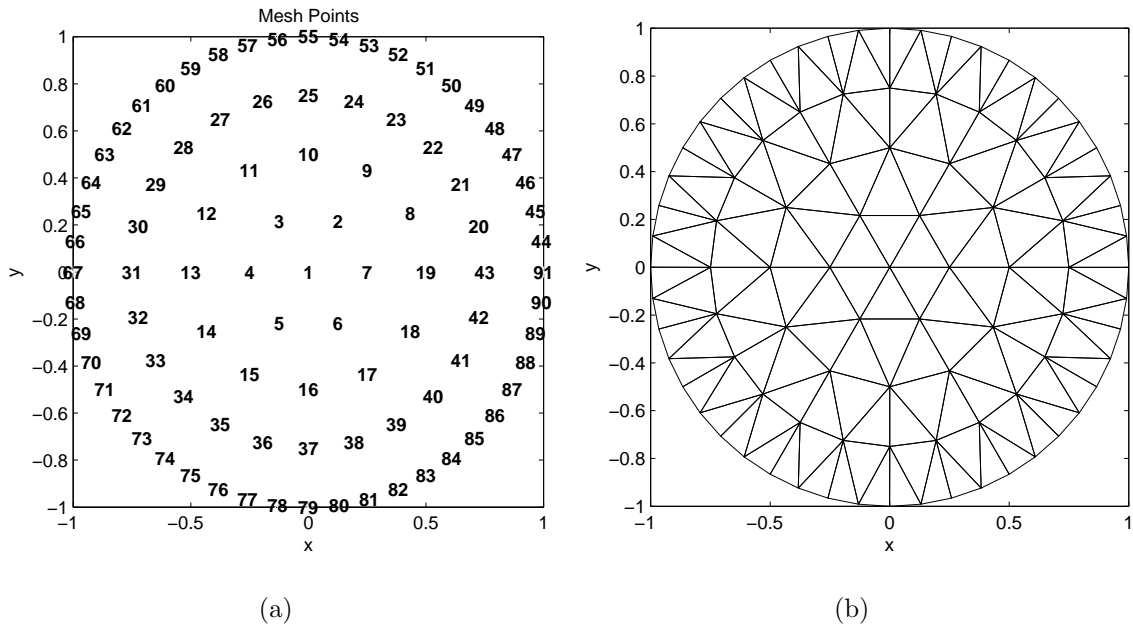


**Figure A.3:** A hexagonal mesh with only 4 circles. Note that each interior node has 6 connections each and the regular hexagon in the centre.

## A.4 Automatic Generation

The final mesh is one that is automatically generated using the open source software GMSH [37]. The software discretises along the lines of the shape, in this case the circumference and diameter of the circle, which are then refined to produce a mesh. Further refinement can be performed to achieve the level of resolution required.

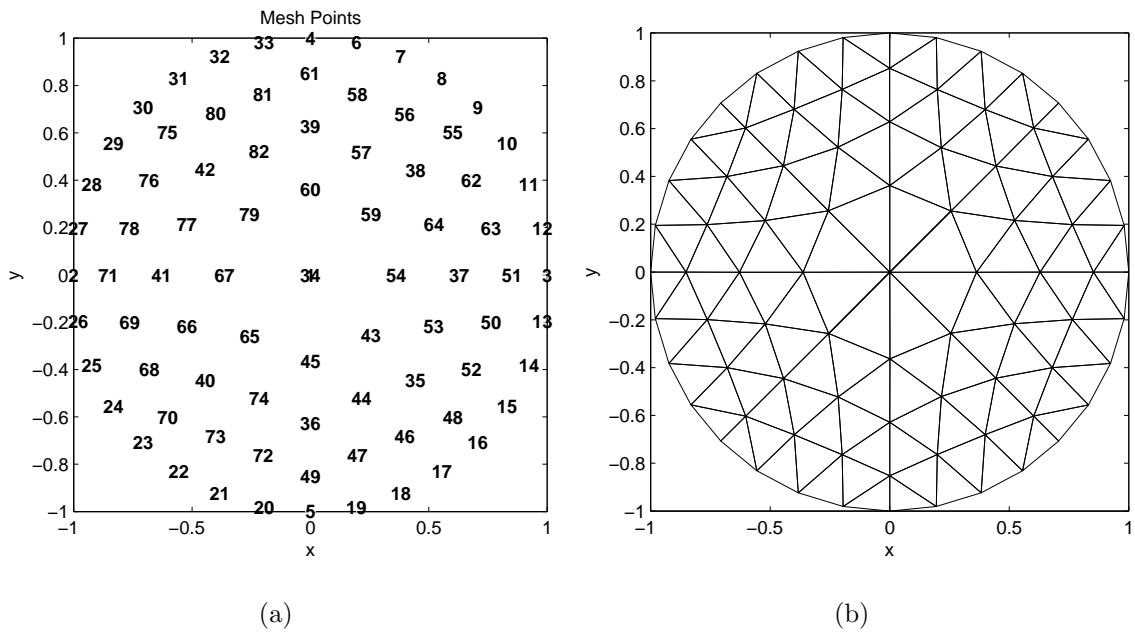


**Figure A.4:** Mesh generated using the software GMSH [37]. The software uses a refinement criteria that leaves the individual triangular elements approximately equilateral in shape.

# Appendix B

## Useful Theorems

We state some of the theorems used in this thesis for convenience, the proofs for which can be readily found.

### B.1 Leibniz's Integral Rule

The differentiation of a definite integral, with limits that are functions of the differential variable is given by

$$\frac{d}{dy} \int_{a(y)}^{b(y)} f(x, y) dx = \int_a^b \frac{d}{dy} f(x, y) dx + f(a(y), y) \frac{da(y)}{dy} - f(b(y), y) \frac{db(y)}{dy}. \quad (\text{B.1})$$

### B.2 L'Hôpital's Rule

L'Hopital's rule states that if

$$\lim_{x \rightarrow a} f(x) = \lim_{x \rightarrow a} g(x) = 0 \text{ (or } \infty), \quad (\text{B.2})$$

then

$$\lim_{x \rightarrow a} \frac{f(x)}{g(x)} = \lim_{x \rightarrow a} \frac{f'(x)}{g'(x)} \quad (\text{B.3})$$

provided the derivatives exist.

### B.3 Trapezium Rule

An integral may be approximated using the Trapezium Rule, where the region is split into  $N$  mesh points and approximated by

$$\int_a^b f(x)dx \approx \frac{1}{2} \sum_{i=1}^{N-1} (x_{i+1} - x_i)(f(x_{i+1}) + f(x_i)). \quad (\text{B.4})$$

### B.4 Reynold's Transport Theorem

A general three dimensional version of Leibniz's Integral Rule is given by Reynolds Transport Theorem [90]:

$$\frac{d}{dt} \int_{\Omega(t)} f(\mathbf{x}, t) d\mathbf{x} = \int_{\Omega(t)} \frac{d}{dt} f(\mathbf{x}, t) d\mathbf{x} + \oint_{\partial\Omega(t)} (\mathbf{v} \cdot \mathbf{n}) f(\mathbf{x}, t) d\Gamma, \quad (\text{B.5})$$

where  $\mathbf{n}$  is the unit normal vector and  $\mathbf{v}$  is the velocity of the area element.

### B.5 Divergence Theorem

The Divergence Theorem relates the volume integral of the divergence to the flux on the surface in the outward normal direction. This is written as:

$$\int_{\Omega} (\nabla \cdot f(\mathbf{x})) d\mathbf{x} = \oint_{\partial\Omega} (f(\mathbf{x}) \cdot \mathbf{n}) d\Gamma \quad (\text{B.6})$$

# Bibliography

- [1] Elmer/ice. <http://elmerice.elmerfem.org/>. Accessed August 15, 2013.
- [2] National parks glossary. <http://www.nature.nps.gov/views/System/Glossary.htm>. Accessed January 29, 2013.
- [3] R. J. Arthern and R. C. A. Hindmarsh. Optimal estimation of changes in the mass of ice sheets. *J. Geophys. Res.*, 108, 2003.
- [4] R. J. Arthern and R. C. A. Hindmarsh. Determining the contribution of antarctica to sea-level rise using data assimilation methods. *Philosophical Transactions: Mathematical, Physical and Engineering Sciences*, 364(1844):pp. 1841–1865, 2006.
- [5] N. Azuma. A flow law for anisotropic ice and its application to ice sheets. *Earth and Planetary Science Letters*, 128, Issue 3-4, 601-614, 1994.
- [6] I. Babuska and B. Q. Guo. The h, p and h-p version of the finite element method: basis theory and applications. *Advances in Engineering Software*, 15, 3-4, 1992.
- [7] M. J. Baines, M. E. Hubbard, and P. K. Jimack. A moving mesh finite element algorithm for the adaptive solution of time-dependent partial differential equations with moving boundaries. *Applied Numerical Mathematics*, 54(34):450 – 469, 2005.
- [8] M. J. Baines, M. E. Hubbard, and P. K. Jimack. Velocity-based moving mesh methods for nonlinear partial differential equations. *Communications in Computational Physics*, 10(3):509–576, 2011.

- [9] J. L. Bamber and R. A. Bindschadler. An improved elevation dataset for climate and ice-sheet modelling: validation with satellite imagery. *Annals of Glaciology*, 25:439–444, 1997.
- [10] J. L. Bamber and A. J. Payne. *Mass balance of the cryosphere*. Cambridge University Press, 2004.
- [11] R. N. Bannister. A review of forecast error covariance statistics in atmospheric variational data assimilation. ii: Modelling the forecast error covariance statistics. *Quarterly Journal of the Royal Meteorological Society*, 134(637):1971–1996, 2008.
- [12] G. Beckett, J. Mackenzie, A. Ramage, and D. Sloan. On the numerical solution of one-dimensional pdes using adaptive methods based on equidistribution. *Journal of Computational Physics*, 167(2):372 – 392, 2001.
- [13] D. I. Benn and D. J. A. Evans. *Glaciers and Glaciation*. Hodder Education, 2010.
- [14] H. Blatter. Velocity and stress-fields in grounded glaciers - a simple algorithm for including deviatoric stress gradients. *Journal of Glaciology*, 41(138), 333-344, 1995.
- [15] B. Bonan, M. Nodet, O. Ozenda, and C. Ritz. Data assimilation in glaciology. In *Advanced Data Assimilation for Geosciences*, 2012.
- [16] F. Bouttier and P. Courtier. Data assimilation concepts and methods. In *Meteorological Training Course Lecture Series*. ECMWF, 2002.
- [17] C. Budd, M. Cullen, and E. Walsh. Mongeampre based moving mesh methods for numerical weather prediction, with applications to the eady problem. *Journal of Computational Physics*, 236(0):247 – 270, 2013.
- [18] C. J. Budd, W. Huang, and R. D. Russell. Adaptivity with moving grids. *Acta Numerica*, 18:111–241, 4 2009.
- [19] W. F. Budd, D. Jenssen, and I. N. Smith. A three-dimensional time-dependent model of the West Antarctic ice sheet. *Annals of Glaciology*, 5:29–36, 1984.

- [20] X.-X. Cai, B. Jiang, and G. Liao. Adaptive grid generation based on the least-squares finite-element method. *Computers & Mathematics with Applications*, 48(78):1077 – 1085, 2004.
- [21] W. Cao, W. Huang, and R. D. Russell. A moving mesh method based on the geometric conservation law. *SIAM J. Sci. Comput.*, 24(1):118–142, Jan. 2002.
- [22] W. Cao, W. Huang, and R. D. Russell. Approaches for generating moving adaptive meshes: location versus velocity. *Applied Numerical Mathematics*, 47:121–138, 2003.
- [23] S. S. Chow, G. F. Carey, and M. L. Anderson. Finite element approximations of a glaciology problem. *ESAIM: Mathematical Modelling and Numerical Analysis*, 38(5):741–756, 3 2010.
- [24] S. Cornford, D. Martin, D. Graves, D. Ranken, A. Le Brocq, R. Gladstone, A. Payne, E. Ng, and W. Lipscomb. Adaptive mesh, finite volume modeling of marine ice sheets. *Journal of Computational Physics*, 232(1):529–549, 2013.
- [25] P. Courtier, E. Andersson, W. Heckley, D. Vasiljevic, M. Hamrud, A. Hollingsworth, F. Rabier, M. Fisher, and J. Pailleux. The ecmwf implementation of three-dimensional variational assimilation (3d-var). i: Formulation. *Quarterly Journal of the Royal Meteorological Society*, 124(550):1783–1807, 1998.
- [26] H. S. M. Coxeter. *Introduction to Geometry*. Wiley, 2nd edition, 1969.
- [27] K. M. Cuffey and W. S. B. Paterson. *The Physics of Glaciers, Fourth Edition*. Academic Press, 2010.
- [28] R. Daley. *Atmospheric Data Analysis*. Cambridge University Press, 1993.
- [29] L. Debreu, E. Simon, and E. Blayo. 4D variational data assimilation for locally nested models: optimality system and preliminary experiments. Technical Report RR-7675, INRIA, July 2011.

- [30] M. R. Drinkwater, R. Francis, G. Ratier, and D. J. Wingham. The european space agency's earth explorer mission cryosat: measuring variability in the cryosphere. *Annals of Glaciology*, 39(1), 2004.
- [31] R. Eeeico and T. Vukicevic. Sensitivity analysis using an adjoint of the psu-near mesoscale model. *Monthly weather review*, 120(8):1644–1660, 1992.
- [32] G. Evensen. Sequential data assimilation with a nonlinear quasi-geostrophic model using monte carlo methods to forecast error statistics. *Journal of Geophysical Research: Oceans*, 99(C5):10143–10162, 1994.
- [33] F. Fang, C. C. Pain, M. D. Piggott, G. J. Gorman, and A. J. H. Goddard. An adaptive mesh adjoint data assimilation method applied to free surface flows. *International Journal for Numerical Methods in Fluids*, 47(8-9):995–1001, 2005.
- [34] F. Fang, M. Piggott, C. Pain, G. Gorman, and A. Goddard. An adaptive mesh adjoint data assimilation method. *Ocean Modelling*, 15(12):39 – 55, 2006.
- [35] J. Fastook. Modeling the ice age: the finite-element method in glaciology. *Computational Science Engineering, IEEE*, 1(1):55–67, 1994.
- [36] J. L. Fastook and M. Prentice. A finite-element model of Antarctica: sensitivity test for meteorological mass-balance relationship. *Journal of Glaciology*, 40:167–175, 1994.
- [37] C. Geuzaine and J.-F. Remacle. Gmsh: a three-dimensional finite element mesh generator with built-in pre- and post-processing facilities. <http://geuz.org/gmsh/>. Accessed February 19, 2013.
- [38] F. Gillet-Chaulet, O. Gagliardini, J. Meyssonier, M. Montagnat, and O. Castelnau. A user-friendly anisotropic flow law for ice-sheet modelling. *Journal of Glaciology*, 51, Issue 172, 3-14, 2005.
- [39] R. M. Gladstone, V. Lee, A. Vieli, and A. J. Payne. Grounding line migration in an adaptive mesh ice sheet model. *Journal of Geophysical Research: Earth Surface*, 115(F4), 2010.

- [40] J. W. Glen. The flow law of ice. *Proc. Roy. Soc.*, 228, 519, 1955.
- [41] D. N. Goldberg and O. V. Sergienko. Data assimilation using a hybrid ice flow model. *The Cryosphere*, 5(2):315–327, 2011.
- [42] D. L. Hartmann. *Global Physical Climatology*. Academic Press, 1994.
- [43] R. C. A. Hindmarsh. A numerical comparison of approximations to the stokes equations used in ice sheet and glacier modeling. *J. Geophys. Res.*, 109, 2004.
- [44] R. L. Hooke. Flow law for polycrystalline ice in glaciers: comparison of theoretical predictions, laboratory data and field measurements. *Geophys. Space Phys.*, 19, 664-672, 1981.
- [45] D. Howell, M. J. Siegert, and J. A. Dowdeswell. Modelling the influence of glacial isostasy on late weichselian ice-sheet growth in the barents sea. *Journal of Quaternary Science*, 15(5):475–486, 2000.
- [46] W. Huang and R. D. Russell. Adaptive mesh movement the mmpde approach and its applications. *Journal of Computational and Applied Mathematics*, 128(12):383 – 398, 2001.
- [47] M. E. Hubbard, M. J. Baines, and P. K. Jimack. Consistent dirichlet boundary conditions for numerical solution of moving boundary problems. *Appl. Numer. Math.*, 59(6):1337–1353, June 2009.
- [48] K. Hutter. *Theoretical Glaciology*. Springer, 1983.
- [49] P. Huybrechts and T. Payne. The eismint benchmarks for testing ice-sheet models. *Annals of Glaciology*, 1996.
- [50] K. P. Ide, P. Courtier, M. Ghil, and A. C. Lorenc. Unified notation for data assimilation: Operational, sequential and variational. *Journal of the Meteorological Society of Japan*, 75 (1B), 181-189, 1997.
- [51] T. Issac. Approaches and challenges in ice sheet modelling. Lecture Notes, University of Texas, 2008.

- [52] K. C. Jezek. Radarsat-1 antarctic mapping project: change-detection and surface velocity campaign. *Annals of Glaciology*, 34(1):263–268, 2002.
- [53] T. Jóhannesson, C. Raymond, and E. Waddington. Time-scale for adjustment of glaciers to changes in mass balance. *Journal of Glaciology*, 35:355–369, 1989.
- [54] I. Joughin and J. L. Bamber. Thickening of the ice stream catchments feeding the filchner-ronne ice shelf, antarctica. *Geophysical Research Letters*, 32(17), 2005.
- [55] G. Jouvet, M. Huss, H. Blatter, M. Picasso, and J. Rappaz. Numerical simulation of rhonegletscher from 1874 to 2100. *J. Comp. Physics*, 228, 6426-6439, 2009.
- [56] G. Jouvet, M. Picasso, J. Rappaz, and H. Blatter. A new algorithm to simulate the dynamics of a glacier: theory and applications. *Journal of Glaciology*, 54, 801-811, 2008.
- [57] R. E. Kalman. A new approach to linear filtering and prediction problems. *Transactions of the ASME - Journal of Basic Engineering*, 82:35-45, 1960.
- [58] R. E. Kalman and R. S. Bucy. New results in linear filtering and prediction theory. *Transactions of the ASME - Journal of Basic Engineering*, 83:95-108, 1961.
- [59] E. Kalnay. *Atmospheric Modeling, Data Assimilation and Predictability*. Cambridge University Press, 2003.
- [60] R. F. Katz and M. G. Worster. Stability of ice-sheet grounding lines. *Proceedings of the Royal Society A: Mathematical, Physical and Engineering Science*, 2010.
- [61] R. A. Klassen. Glacial history and ice flow dynamics applied to drift prospecting and geochemical exploration. *Proceedings of Exploration 97: Fourth Decennial International Conference on Mineral Exploration*, pages 221–232, 1997.
- [62] J. K. W. Lam and J. A. Dowdeswell. An adaptive-grid finite-volume model of glacier-terminus fluctuations. *Annals of Glaciology*, 23:86–93, 1996.

- [63] E. Larour, H. Seroussi, M. Morlighem, and E. Rignot. Continental scale, high order, high spatial resolution, ice sheet modeling using the ice sheet system model (issm). *Journal of Geophysical Research: Earth Surface*, 117(F1), 2012.
- [64] F. X. Le Demit and O. Talagrand. Variational algorithms for analysis and assimilation of meteorological observations: Theoretical aspects. *Tellus*, 38A:97110, 1986.
- [65] J. Lewis, S. Lakshmiarahan, and S. Dhall. *Dynamic Data Assimilation: A Least Squares Approach*. Number v. 13 in Dynamic data assimilation: a least squares approach. Cambridge University Press, 2006.
- [66] G. Liao and D. Anderson. A new approach to grid generation. *Applicable Analysis*, 44(3-4):285–298, 1992.
- [67] H. Liu, K. C. Jezek, and B. Li. Development of an antarctic digital elevation model by integrating cartographic and remotely sensed data: A geographic information system based approach. *Journal of Geophysical Research: Solid Earth*, 104(B10):23199–23213, 1999.
- [68] A. C. Lorenc. Analysis methods for numerical weather prediction. *Quarterly Journal of the Royal Meteorological Society*, 112(474):1177–1194, 1986.
- [69] A. C. Lorenc, S. P. Ballard, R. S. Bell, N. B. Ingleby, P. L. F. Andrews, D. M. Barker, J. R. Bray, A. M. Clayton, T. Dalby, D. Li, T. J. Payne, and F. W. Saunders. The met. office global three-dimensional variational data assimilation scheme. *Quarterly Journal of the Royal Meteorological Society*, 126(570):2991–3012, 2000.
- [70] M. B. Lythe and D. G. Vaughan. Bedmap: A new ice thickness and subglacial topographic model of antarctica. *Journal of Geophysical Research: Solid Earth*, 106(B6):11335–11351, 2001.
- [71] D. R. MacAyeal. Large-scale ice flow over a viscous basal sediment: Theory and application to ice stream b, antarctica. *J. Geophys. Res.*, 94, 4071-4087, 1989.

- [72] M. W. Mahaffy. A three-dimensional numerical model of ice sheets: Tests on the barnes ice cap, northwest territories. *J. Geophys. Res.*, 81(6), 1059-1066, 1976.
- [73] A. Mangeney and F. Califano. The shallow ice approximation for anisotropic ice: Formulation and limits. *J. Geophys. Res.*, 103, 491-705, 1998.
- [74] D. McRae. r-refinement grid adaptation algorithms and issues. *Computer Methods in Applied Mechanics and Engineering*, 189(4):1161 – 1182, 2000.
- [75] G. A. Meehl, T. F. Stocker, W. D. Collins, P. Friedlingstein, A. T. Gaye, J. M. Gregory, A. Kitoh, R. Knutti, J. M. Murphy, A. Noda, S. C. B. Raper, I. G. Watterson, A. J. Weaver, and Z. C. Zhao. Global climate projections. In *Contribution of Working Group I to the Fourth Assessment Report of the Intergovernmental Panel on Climate Change*. Cambridge University Press, 2007.
- [76] K. Miller and R. Miller. Moving finite elements. i. *SIAM Journal on Numerical Analysis*, 18(6):1019–1032, 1981.
- [77] L. W. Morland. Thermomechanical balances of ice sheet flows. *Geophysical & Astrophysical Fluid Dynamics*, 29(1-4):237–266, 1984.
- [78] B. Munson, D. Young, T. Okiishi, and W. Huebsch. *Fundamentals of fluid mechanics*. Wiley, 2009.
- [79] N. K. Nichols. *Data Assimilation for the Earth System*, chapter Data Assimilation: Aims and basic concepts. Kluwer Academic, 2003.
- [80] N. K. Nichols. *Data Assimilation: Making Sense of Observations*, chapter Mathematical concepts of data assimilation. Springer, 2009.
- [81] S. Nowicki and D. Wingham. Conditions for a steady ice sheetice shelf junction. *Earth and Planetary Science Letters*, 265(12):246 – 255, 2008.
- [82] J. F. Nye. The flow law of ice from measurements in glacier tunnels, laboratory experiments and the jungfraufirn borehole experiments. *Proc. Roy. Soc*, 219, 477-489, 1953.

- [83] J. F. Nye. The distribution of stress and velocity in glaciers and ice sheets. *Proc. Roy. Soc.*, 239, 113-133, 1957.
- [84] J. Oerlemans. A flowline model for nigardsbreen, norway: projection of future glacier length based on dynamic calibration with the historic record. *Annals of Glaciology*, 24, 1997.
- [85] F. Pattyn. A new three-dimensional higher-order thermomechanical ice sheet model: Basic sensitivity, ice stream development, and ice flow across subglacial lakes. *J. Geophys. Res.*, 108, 2382, 1989.
- [86] A. J. Payne, P. R. Holland, A. P. Shepherd, I. C. Rutt, A. Jenkins, and I. Joughin. Numerical modeling of ocean-ice interactions under pine island bay's ice shelf. *Journal of Geophysical Research: Oceans*, 112(C10), 2007.
- [87] J. R. Petit, J. Jouzel, D. Raynaud, N. I. Barkox, J. M. Barnola, I. Basile, M. Bender, J. Chappellaz, M. Davis, G. Delaygue, M. Delmotte, V. M. Kotlykov, M. Legrand, V. Y. Lipenkov, C. Lorius, L. Pepin, C. Ritz, E. Saltzman, and M. Stievenard. Climate and atmospheric history of the past 420,000 years from the vostok ice core, antarctica. *Nature*, 399, 429-436, 1999.
- [88] C. Piccolo and M. Cullen. Adaptive mesh method in the met office variational data assimilation system. *Quarterly Journal of the Royal Meteorological Society*, 137(656):631-640, 2011.
- [89] C. Piccolo and M. Cullen. A new implementation of the adaptive mesh transform in the met office 3d-var system. *Quarterly Journal of the Royal Meteorological Society*, 138(667):1560-1570, 2012.
- [90] O. Reynolds, A. Brightmore, and W. Moorby. *Papers on Mechanical and Physical Subjects: The sub-mechanics of the universe*. Papers on Mechanical and Physical Subjects. The University Press, 1903.
- [91] C. D. Rodgers. *Inverse methods for atmospheric sounding*. World Scientific Publishing Co. Pte. Ltd, 2000.

- [92] F. Saito, A. Abe-Ouchi, and H. Blatter. Effects of first-order stress gradients in an ice sheet evaluated by a three-dimensional thermomechanical coupled model. *Annals of Glaciology*, 37, 2003.
- [93] C. Schoof. Ice sheet grounding line dynamics: Steady states, stability, and hysteresis. *Journal of Geophysical Research: Earth Surface*, 112(F3), 2007.
- [94] G. D. Smith and L. W. Morland. Viscous relations for the steady creep of polycrystalline ice. *Cold Regions Science and Technology*, 5, Issue 2, 141-150, 1981.
- [95] S. Sokolovskiy, Y.-H. Kuo, and W. Wang. Assessing the accuracy of a linearized observation operator for assimilation of radio occultation data: Case simulations with a high-resolution weather model. *Monthly Weather Review*, 133(8):2200–2212, 2005.
- [96] S. Solomon, D. Qin, M. Manning, Z. Chen, M. Marquis, K. B. Averyt, M. Tignor, and H. L. Miller. *Contribution of Working Group I to the Fourth Assessment Report of the Intergovernmental Panel on Climate Change*. Cambridge University Press, 2007.
- [97] A. J. Starr. *Numerical Modelling of Ice-Sheets using Adaptive Grids*. Phdthesis, The University of Wales, 2001.
- [98] G. Strang. *Introduction to Linear Algebra*. Wellesley-Cambridge Press, 2003.
- [99] H. Tang and T. Tang. Adaptive mesh methods for one- and two-dimensional hyperbolic conservation laws. *SIAM Journal on Numerical Analysis*, 41(2):487–515, 2003.
- [100] T. Tang. *Moving Mesh Methods for Computational Fluid Dynamics*. Technical report. Department of Mathematics, Hong Kong Baptist University, 2005.
- [101] J. Van Den Berg, R. S. W. Van De Wal, and J. Oerlemans. Effects of spatial discretization in ice-sheet modelling using the shallow-ice approximation. *Journal of Glaciology*, 52(176):89 – 98, 2006.

- [102] C. J. Van Der Veen. *Fundamentals of Glacier Dynamics*. Taylor and Francis, 1999.
- [103] D. Vaughan, J. Bamber, M. Giovinetto, J. Russell, and A. Cooper. Reassessment of the net surface mass balance in antarctica. *Journal of Climate*, 12(4):933 – 946, 1999.
- [104] S. S. Vialov. Regularities of glacial shields movement and the theory of plastic viscous flow. *International Association of Scientific Hydrology Publication*, 47, 1958.
- [105] A. Vieli and A. J. Payne. Assessing the ability of numerical ice sheet models to simulate grounding line migration. *J. Geophys. Res*, 110(F01003), 2005.
- [106] A. Vieli, A. J. Payne, Z. Du, and A. Shepherd. Numerical modelling and data assimilation of the larsen b ice shelf, antarctic peninsula. *Philosophical Transactions of the Royal Society A: Mathematical, Physical and Engineering Sciences*, 364(1844):1815–1839, 2006.
- [107] L. Wang and M. Ikeda. A lagrangian description of sea ice dynamics using the finite element method. *Ocean Modelling*, 7(12):21 – 38, 2004.
- [108] J. Weertman. Creep of ice. *Physics and chemistry of ice*, 320-337, 1973.
- [109] B. V. Wells. *A Moving Mesh Finite Element Method for the Numerical Solution of Partial Differential Equations and Systems*. PhD thesis, The University of Reading, October 2004.
- [110] P. Wesseling. *Principles of Computational Fluid Dynamics*. Springer Series in Computational Mathematics. Springer, 2001.
- [111] A. V. Wilchinsky and Chugunov. Modelling ice flow in various glacier zones. *J. Appl. Maths Mechs.*, 65, No. 3, 2001.

- [112] T. R. Wylie. The integration of an hp-adaptive finite element analysis library into the community ice-sheet model. Masterthesis, The University of Montana, 2010.